Investigating the BOLD Haemodynamic Response

by N. P. Blockley BSc. (Hons) MPhil.

Thesis submitted to The University of Nottingham
for the degree of Doctor of Philosophy

June 2007

Contents

List of Figures

List of Tables

Glossary

ASL	Arterial Spin Labelling
BBB	Blood Brain Barrier
BOLD	Blood Oxygenation Level Dependent
CBF	Cerebral Blood Flow
CBV	Cerebral Blood Volume
$CMRO_2$	Cerebral Metabolic Rate of Oxygen consumption
CPMG	Carr-Purcell-Meiboom-Gill
CSA	Chemical Shift Anisotropy
CT	Computed Tomography
DSV	Diameter of homogenous Spherical Volume
EPI	Echo Planar Imaging
EVI	Echo Volumar Imaging
FFT	Fast Fourier Transform
FID	Free Induction Decay
fMRI	Functional Magnetic Resonance Imaging
fNIRS	functional Near Infra Red Spectroscopy
FWHM	Full Width Half Maximum

GLM	General Linear Model
GRF	Gaussian Random Fields
HCT	Haematocrit
HRF	Haemodynamic Response Function
IR	Inversion Recovery
MBEST	Modulus Blipped Echo planar Shot Technique
MEG	Magnetoencephalography
MNI	Montreal Neurological Institute
MR	Magnetic Resonance
MRI	Magnetic Resonance Imaging
MRS	Magnetic Resonance Spectroscopy
Nb-Sn	Niobium-Tin
Nb-Ti	Niobium-Titanium
NMR	Nuclear Magnetic Resonance
NMRD	Nuclear Magnetic Resonance Dispersion
PR	Projection Reconstruction
RF	Radio Frequency
SA	Simulated Annealing
SENSE	SENSitivity Encoding
SNR	Signal to Noise Ratio
SPIO	Super Paramagnetic Iron Oxide
SPMMRC	Sir Peter Mansfield Magnetic Resonance Centre

TEM	Transverse ElectroMagnetic
TI	Inversion Time
TSP	Travelling Salesman Problem
VASO	Vascular Space Occupancy

Abstract

In this thesis the underlying mechanisms behind the phenomenon known as the BOLD response were investigated.

Functional imaging of the brain relies on the oxygenation level of blood, therefore the relaxation properties of blood were measured at different oxygenations. The relaxation properties of blood are also modified by introduction of a paramagnetic contrast agent and are dependent on the static magnetic field of the MRI system. These dependencies were also characterised. This led to the discovery that the transverse relaxation rate is non-linearly related to contrast agent concentration. This result was confirmed by performing a Monte-Carlo simulation.

A measurement of total cerebral blood volume (CBV) change, during neural activity, was performed at high temporal resolution (TR = 300 ms). This was achieved by infusing a contrast agent, whilst a visual stimulus was presented to the volunteer. This technique also provided an interesting and novel method to test models of the BOLD response. The temporal characteristics of the BOLD response were differentially effected by the contrast agent, reflecting the dependency of each feature on blood volume change. This allowed a qualitative understanding of the volume contribution to each of these characteristics to be gathered.

Two models of the BOLD haemodynamic response were constructed to describe the contrast agent infusion experiment. Each model was developed from several existing models of the BOLD response, with the aim of comparing empirical and biomechanical model elements. As part of this work an existing model of BOLD signal change was extended to include the arterial and venous vasculature. Both models were separately fitted to the experimental total CBV and BOLD signal data. The results of fitting the data show that existing haemodynamic models cannot fully describe the measured results.

Acknowledgements

There are many people I would like to thank for their help and encouragement throughout my PhD.

Firstly, my supervisors, Prof. Penny Gowland and Dr. Sue Francis, for letting me join the SPMMRC in the first instance and also for their expert guidance and experience. Their helpful suggestions added immeasurably to my work, and this thesis.

I am also indebted to Dr. Andy Peters, Kay Head, Lesley Martin, Paul Clark, Dr. Deep Karia, Ian Thexton, Jeff Smith and David 'Jeph' Jephcote, without whom some aspects of this thesis would not have been possible. Similarly I must also acknowledge the funding provided by the Medical Research Council and the University of Nottingham to enable this research.

As for my office mates, past and present, I must thank them for keeping me entertained and help on many occasions with the vagaries of physics. Early office mates to thank include Matt, Alex, Gianlo, Elliot, Sean and Ian, and more recently Claire, Eleanor, Karen, and Mary. Other *extra-office* companions I would like to thank are Arthur, Mike, Bhavana and Wietske.

I thank my family for their whole-hearted support. In particular I must thank Fliss for putting up with me during the dark days of thesis writing.

Chapter 1

Introduction

1.1 Introduction

The work contained within this thesis began on 22nd September 2003. The aim of this work was to investigate the haemodynamic response associated with neural activation, otherwise known as the BOLD response. A particular emphasis was placed on measuring total cerebral blood volume changes during a short visual stimulus. This experimental work was subsequently modelled theoretically. This also involved measurements of intravascular blood signal *in vitro*, in order to simulate the changes in the magnetic resonance signal. An overview of the chapters describing this work is given in section 1.3.

The end of 2003 proved to be an exciting time to be a member of the Sir Peter Mansfield Magnetic Resonance Centre (SPMMRC), as on 6th October Peter Mansfield was awarded the Nobel prize for Physiology or Medicine. The prize was awarded jointly with Paul Lauterbur in recognition of their independent discovery of magnetic resonance imaging (MRI). Therefore it seems only fitting that this thesis starts at the beginning. A quick spin around the early history of MRI.

1.2 A Spin History

The award of the Nobel prize to Peter Mansfield and Paul Lauterbur was by no means the first to be awarded [1] in relation to magnetic resonance (MR), see table 1.1. In 1944 Isidor Rabi was awarded the Nobel prize for physics for his molecular beam experiments. Next came Edward Purcell and Felix Bloch, in 1952, for the development of nuclear magnetic resonance (NMR). Richard Ernst and Kurt Wüthrich were both awarded the Nobel prize for chemistry in 1991 and 2002, respectively. The former of these laureates noted in his Nobel lecture [2] that there are also several other recipients of the Nobel prize (table 1.2) that have made important contributions to MR. John van Vleck developed the theory of dia- and paramagnetism, Nicolaas Bloembergen worked on relaxation theory, and Alexander Müller contributed to electron paramagnetic resonance. Hans Dehmelt developed pure nuclear quadrupole resonance and Norman Ramsey introduced the concept of chemical shift and J-coupling.

In 1973 Paul Lauterbur published [3] the first two-dimensional NMR image of two tubes of water, with the aim of imaging more complex objects. Several months later, and entirely independently, Peter Mansfield applied similar techniques to produce [4] one-dimensional images of interleaved sheets of plastic and camphor. In uniquely British fashion, the rudiments of the technique were discussed [5] in the tea room of the Department of Physics at the University of Nottingham. Mansfield's initial aim was to perform crystallography using the technique. Whilst presenting this work at the First Specialized Colloque Ampère in Krakow the subsequent discussion led him to the work of Lauterbur. At this point Mansfield realised [6] that imaging in solids was probably ahead of its time and was consigned to *future work*. By imaging biological samples the process was made far easier.

Following a short spell at the University of Illinois, Mansfield moved to the University of Nottingham. He was recruited to the post by Raymond Andrew, who had recently been invited to take up the Lancashire-Spencer chair of physics [7]. Under Andrew's guidance the department of physics

became an international hub for NMR research. Mansfield formed his own group within the department consisting of a postdoc Alan Garroway and PhD student Peter Grannell. Chief amongst the Andrew group were Waldo Hinshaw and Bill Moore. In 1974 Hinshaw and Moore attended the ISMAR conference in Bombay. Lauterbur was also in attendance and gave a talk on his imaging work. This created a great deal of excitement amongst the Nottingham contingent and on their return Hinshaw rapidly devised a new imaging method [8], known as *sensitive point* imaging. By applying time dependent magnetic field gradients along two orthogonal axes it was possible to move this sensitive point around the sample, point by point, and build up an image. Inevitably this was a very slow process, however reconstructing images from this data wasn't very demanding. Digital signal processing was unheard of at the time and computers of the era could do little more than arithmetic [9]. Therefore the simplicity of the sensitive point method had its merits. However, Mansfield and colleagues followed a different approach. They devised a way of selectively exciting a slice of the sample through the use of magnetic field gradients and shaped RF pulses [10]. This led to the line scan imaging [11] technique and the first image of a human finger [12].

Of course Nottingham were not alone [5] in this endeavour. In the UK research was conducted around two centres. In Nottingham by the Andrew and Mansfield groups and in Aberdeen by a group headed by John Mallard. They were subsequently joined by EMI, the first commercial entrant, at the Hammersmith Hospital in London. In the US, groups were led by Paul Lauterbur and Raymond Damadian and in Europe by Richard Ernst in Zürich. The Zürich group were the first to suggest two-dimensional Fourier imaging [13] which was later practically implemented by Bill Edelstein [14] of the Aberdeen group as spin warp imaging. This was an extremely important step as it allowed detailed images to be acquired in a reasonable time-scale, proving that MRI was a viable clinical technique.

In the intervening years rivalry between the different groups was fierce. In fact so fierce that a third group was formed at Nottingham by Bill Moore

by splitting the Andrew group, causing subsequent animosity. This added to the existing acrimony between the Mansfield and Andrew groups, caused by arguments [6] over an earlier grant proposal to the Medical Research Council. As Mansfield noted *"...matters eventually settled down in a quasi steady state."*. However worse was to come, as in the early 1980's research funding cuts left British universities with a massive overstaffing problem. A generous early retirement scheme was introduced leading to Raymond Andrew and Bill Moore leaving Nottingham for the US. In addition Waldo Hinshaw had already left to work for Technicare, after an initial time with GEC. Therefore by the mid-80's there was only one group left in Nottingham: the Mansfield group. The Aberdeen group suffered similarly when Bill Edelstein also left to work for GE. EMI pulled out of medical imaging and the system at the Hammersmith was sold to Picker. From then on commercialisation of MRI was largely conducted by companies based outside of the UK. As one of the chief members of the EMI project, Ian Young, said [5] *"...Britain snatched defeat from the jaws of victory..."*.

Still the period between 1980 and 1990 proved to be something of a golden era for the development of MRI at Nottingham. The acquisition of a 0.5 T superconducting magnet pushed the boundaries of field strength. Actively shielded gradients were developed [15, 16], to prevent the magnet from quenching during rapidly switched magnetic field gradients. This allowed Echo Planar Imaging [12] (EPI) to be implemented [17]. The extension of EPI to a three-dimensional acquisition known as Echo Volumar Imaging (EVI) was also described [18].

Today the SPMMRC continues to be at the forefront of MRI technology. This is exemplified by the installation of an ultra-high field 7.0 T whole body MRI system in 2005, the first in the UK. The emphasis of this thesis is on the application of MRI to functional neuroimaging. A field that could not have been foreseen, or even contemplated, when imaging with NMR was first considered. I think Raymond Andrew summed this up best when he said [5] *"Now new horizons are being unveiled with the development of functional*

MRI. Not only can we think about MRI, but MRI can watch us thinking about MRI. Furthermore, MRI can watch us thinking about MRI recording our thoughts on MRI, and so on, to the n^{th} degree.". Who knows what the next 35 years have in store...

Name	Year	Category	Description
Paul Lauterbur	2003	Medicine	For their discoveries concerning magnetic resonance imaging
Peter Mansfield	2003	Medicine	
Kurt Wüthrich	2002	Chemistry	For his development of nuclear magnetic resonance spectroscopy for determining the three-dimensional structure of biological macromolecules in solution
Richard Ernst	1991	Chemistry	For his contributions to the development of the methodology of high resolution nuclear magnetic resonance (NMR) spectroscopy
Albert Kastler	1966	Physics	Optical methods for studying Hertzian resonances
Felix Bloch	1952	Physics	For their development of new methods for nuclear magnetic
Edward Purcell	1952	Physics	precision measurements and discoveries in connection therewith
Isidor Rabi	1944	Physics	For his resonance method for recording the magnetic properties of atomic nuclei

Table 1.1: Nobel prizes awarded for work in the field of magnetic resonance.

Name	Year	Category	Description
Norman Ramsey	1989	Physics	For the invention of the separated oscillatory fields method and its use in the hydrogen maser and other atomic clocks
Hans Dehmelt	1989	Physics	For the development of the ion trap technique
Alexander Müller	1987	Physics	For their important break-through in the discovery of superconductivity in ceramic materials
Nicolaas Bloembergen	1981	Physics	For their contribution to the development of laser spectroscopy
John van Vleck	1977	Physics	For their fundamental theoretical investigations of the electronic structure of magnetic and disordered systems

Table 1.2: Nobel prize winners who contributed to the field of magnetic resonance.

1.3 Thesis Overview

The aim of this work was to investigate the underlying mechanisms of the BOLD response. The following chapters describe the work performed in this endeavour.

Chapter 2 contains the background theory that underpins this thesis. It begins with the origins of nuclear magnetic resonance and continues with the general principles of magnetic resonance imaging. The application of these techniques to functional imaging are also discussed.

Chapter 3 presents relaxometry measurements of human blood at 1.5 T, 3.0 T and 7.0 T. The dependence of R_1 and R_2^* on blood oxygenation and paramagnetic contrast agent concentration is also investigated. The aim of these experiments is to inform models of intravascular signal.

Chapter 4 describes a method for measuring total cerebral blood volume changes with high temporal resolution. This work involves the use of a paramagnetic contrast agent.

Chapter 5 discusses the use of a biophysical model to simulate the experiment performed in chapter 4. Simulations are performed using a selection of modelling elements derived from the literature and fitting performed to the experimental data.

Chapter 6 summarises the results of chapters 3 to 5 and draws general conclusions about this work. Future work is also discussed.

Chapter 2

Background Theory

2.1 Introduction

This chapter aims to describe the background theory that underpins this thesis. This theory spans the basic principles of nuclear magnetic resonance, magnetic resonance imaging and functional imaging.

2.2 Nuclear Magnetic Resonance

The Pauli exclusion principle, formulated in 1924 by Wolfgang Pauli, paved the way for the discovery of spin angular momentum. The initial idea of a spin angular momentum associated with the electron was suggested by Ralph Kronig in order to describe the *Pauli degree of freedom*. However, following criticism of his theory by Pauli and Heisenberg he decided not to publish it. Instead it was left to Goudsmit and Uhlenbeck who in 1926 published [19] their *spinning electrons* hypothesis. Despite Pauli's initial reservations he formalised these ideas using the then new theory of quantum mechanics. Finally in 1928 Paul Dirac formulated [20] a relativistic quantum mechanical wave equation to describe spin-$\frac{1}{2}$ particles, for which he was awarded the Nobel Prize for Physics.

The field of Nuclear Magnetic Resonance (NMR) and Magnetic Reson-

ance Imaging (MRI) exists due to the discovery of the intrinsic spin angular momentum associated with elementary particles. The following sections describe the utilisation of spin in order to *spy* on the microscopic environment of such particles.

2.2.1 Spin Angular Momentum

Classically, a rotating object possesses angular momentum, $\boldsymbol{l} = \boldsymbol{r} \times \boldsymbol{p}$, and this can take any finite value. However in quantum mechanical systems angular momentum is quantised, requiring changes in angular momentum to occur in discrete steps between allowed rotational states. A simple example of such a system is a diatomic molecule. For a diatomic molecule the total angular momentum, l_{tot}, of each state is given by,

$$l_{tot} = \hbar\sqrt{J(J+1)} \tag{2.1}$$

where $\hbar$ is Planck's constant divided by 2π and J is an integer value. The molecule may possess any value of angular momentum permitted by equation 2.1. This value determines the rotational rate of the molecule but not the axis with which it rotates. In order to determine this a second quantum number, m_J, must be defined. This quantum number can take one of $2J+1$ integer values: $m_J = -J, -J+1 \ldots + J$. The value of m_J gives information about the direction of rotation. In the absence of a magnetic field these states are degenerate. This is due to the fact that there are several different states, i.e. combinations of angular momentum and direction of rotation, with the same energy. By applying an electric or magnetic field this degeneracy is removed causing each of the $2J+1$ states to possess a slightly different energy.

Spin angular momentum, l_S, or *spin* is also quantised and can take values of the following form,

$$l_S = \hbar\sqrt{S(S+1)} \tag{2.2}$$

where S is the spin quantum number. All nuclei have an intrinsic value of this spin quantum number, although not all have non-zero values, see

Isotope	Intrinsic Spin	Natural Abundance	Gyromagnetic Ratio / MHz T^{-1}
^{1}H	$\frac{1}{2}$	100 %	42.58
^{2}H	1	0.015 %	6.54
^{3}H	$\frac{1}{2}$	0	45.41
^{12}C	0	98.9 %	-
^{13}C	$\frac{1}{2}$	1.1 %	10.71
^{14}N	1	99.6 %	3.08
^{15}N	$\frac{1}{2}$	0.37 %	-4.32
^{16}O	0	100 %	-
^{17}O	$\frac{5}{2}$	0.04 %	5.77
^{19}F	$\frac{1}{2}$	100 %	40.08
^{31}P	$\frac{1}{2}$	100 %	17.25

Table 2.1: The MR properties of a selection of nuclei [21].

table 2.1 for some examples. These values can either be whole integer ($S = 0, 1, 2 \ldots$), or half integer ($S = \frac{1}{2}, \frac{3}{2}, \frac{5}{2} \ldots$). It is important to note that whereas rotational angular momentum is acquired during energetic collisions, spin angular momentum just exists, it cannot be increased nor decreased. As well as the magnitude of spin angular momentum, l_S, it is possible to define its direction through a second quantum number m_S with $2S+1$ integer states: $m_S = -S, -S+1 \ldots + S$. Therefore the magnitude of l with respect to the conventional axis, z, is given by,

$$l_z = \hbar m_S \tag{2.3}$$

For example, the intrinsic spin of a hydrogen nucleus (^{1}H) is $\frac{1}{2}$, therefore $m_S = \pm\frac{1}{2}$. However, a spin-1 particle, such as deuterium (^{2}H), has three possible states: $m_S = -1, 0, +1$. Figure 2.1 shows this splitting diagrammatically.

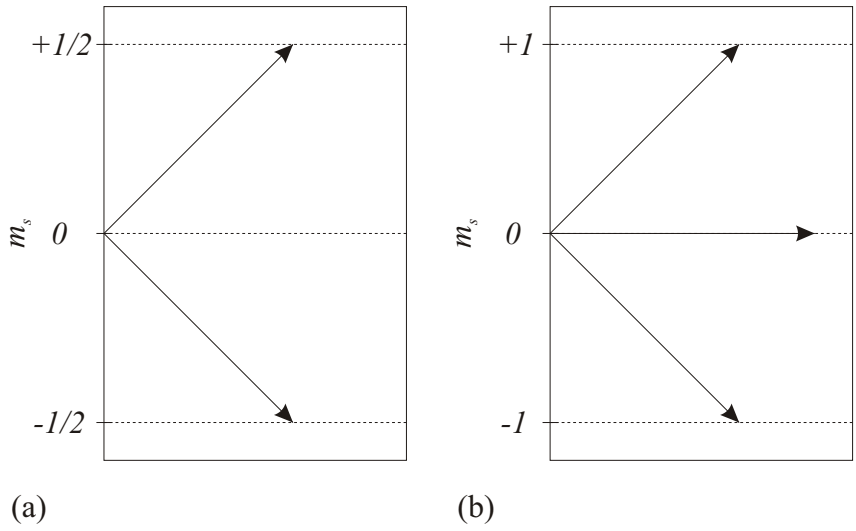

Figure 2.1: Fine splitting of (a) spin-$\frac{1}{2}$ and (b) spin-1 atoms.

2.2.2 Magnetic Field Interaction

The magnetic moment of a particle with non-zero spin has the following form.

$$\boldsymbol{\mu} = \gamma \boldsymbol{l_S} \tag{2.4}$$

The constant of proportionality linking spin and magnetism is the gyromagnetic ratio, γ. When the nucleus is placed in a magnetic field, B, the degeneracy of the $2S + 1$ spin states is destroyed. The energy, E, of the magnetic moment in this static field is,

$$E = -\boldsymbol{\mu} \cdot \boldsymbol{B} \tag{2.5}$$

This interaction between atoms and magnetic fields was first noted by Pieter Zeeman [22] in 1897, and is known as the Zeeman effect in his honour.

Assuming that the nuclear magnetic moment is parallel with the applied magnetic field, a combination of equations 2.3, 2.4 and 2.5 gives the following

relation.

$$E = -\hbar\gamma B_0 m_S \tag{2.6}$$

The magnetic field, B_0, is assumed to be static, uniform and parallel to the $z-$axis. The energy of a nucleus in a magnetic field is dependent on the magnetic field and its intrinsic spin. Therefore the allowable energy states of a given nucleus will be equally spaced. For example a spin-$\frac{1}{2}$ nucleus will exhibit two energy states corresponding to the $+\frac{1}{2}$ and $-\frac{1}{2}$ spin states. Hence the difference between these energy states, ΔE, is given by equation 2.7 and illustrated in figure 2.2.

$$\Delta E = \hbar\gamma B_0 = 2\mu B_0 \tag{2.7}$$

Transitions between the $+\frac{1}{2}$ and $-\frac{1}{2}$ states can be induced by the application of an oscillating magnetic field. The angular frequency of this field is related to its energy by $E = \hbar\omega$. By equating this relation with equation 2.7 it is possible to calculate the characteristic Larmor frequency, ω_0, associated with a given nucleus.

$$\omega_0 = \gamma B_0 \tag{2.8}$$

2.2.3 Bulk Magnetisation

The two energy states of a spin-$\frac{1}{2}$ nucleus, $+\frac{1}{2}$ and $-\frac{1}{2}$, are often described as the spin-up ($\uparrow$) and spin-down ($\downarrow$) states. This nomenclature represents the fact that the nuclear spins are aligned parallel or antiparallel to the main magnetic field. The spin-up state has a lower energy and is therefore the most favourable. However thermal energy permits changes of state from the low energy spin-up state to the higher energy spin-down state. At room temperature this leads to a small difference in the populations of spin-up and spin-down states. The Boltzmann distribution can be used to predict this population difference,

$$\frac{N_\downarrow}{N_\uparrow} = e^{\frac{\gamma\hbar B_0}{k_B T}} \tag{2.9}$$

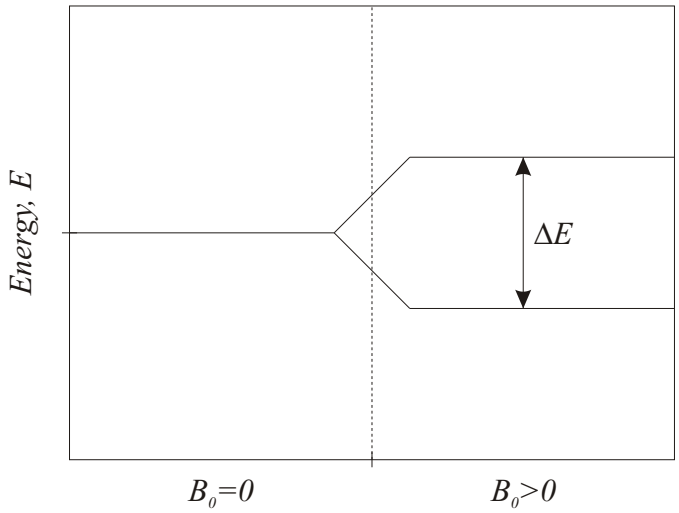

Figure 2.2: Zeeman splitting for a spin-$\frac{1}{2}$ nucleus.

where N is the number of spins in the spin-up ($\uparrow$) and spin-down ($\downarrow$) states, k_B is Boltzmann's constant and T is temperature. Expanding the exponential using a power series yields,

$$\frac{N_\downarrow}{N_\uparrow} \approx 1 + \frac{\gamma\hbar B_0}{k_B T} \tag{2.10}$$

when $\gamma\hbar B_0 \ll k_B T$. Therefore the fractional difference in the populations of the two spin states is,

$$\frac{N_\downarrow - N_\uparrow}{N_\uparrow} \approx \frac{\gamma\hbar B_0}{k_B T} \tag{2.11}$$

At room temperature in the presence of a 3.0 T magnetic field this population difference is of the order of 10^{-6}. It is this small population of spins that is used in the NMR experiment. Conveniently for ^{1}H NMR this Hydrogen isotope has almost 100 % natural abundance. A further consideration is the total number of spins available in the sample. From Avogadro's constant one mole of atoms contains 10^{23} particles. Therefore the population difference is approximately equal to $10^{23} \times 10^{-6} \approx 10^{17}$ spins per mole. However it is still possible to increase sensitivity through equation 2.11. This can be achieved by decreasing the sample temperature or increasing the magnetic

field. The former is not achievable in the clinical setting, hence the need to push to ever higher magnetic field strengths. Today's NMR systems have magnetic field strengths an order of magnitude larger than early systems, largely due to the development of the superconducting magnet. Other routes to higher sensitivity include hyperpolarised noble gases [23] and dynamic nuclear polarisation [24].

In the NMR experiment the bulk effect of this *ensemble* of spins is observed. The sum of the individual spin magnetic moments constitutes the bulk magnetisation, $\boldsymbol{M}$.

$$\boldsymbol{M} = \sum \boldsymbol{\mu} \tag{2.12}$$

2.2.4 Nuclear Induction

It was Felix Bloch who coined the term *nuclear induction* to describe the results of his early NMR experiments [25]. Simultaneously and independently Edward Purcell performed similar experiments [26] and together they were awarded the Nobel Prize for Physics in 1952. In mid-1946 Bloch formulated [27] a phenomenological description of the experiments he performed using classical mechanics. In order to simplify the description Bloch made two assumptions;

1. changes of orientation of each nucleus are solely due to the presence of external fields

2. the external fields are uniform throughout the sample

Evidently these assumptions are unrealistic, but relaxation effects can be reintroduced into the Bloch equation. The total spin angular momentum vector, $\boldsymbol{L_S}$, of the spin ensemble satisfies the classical equation,

$$\frac{d\boldsymbol{L_S}}{dt} = \boldsymbol{T} \tag{2.13}$$

where $\boldsymbol{T}$ is the total torque acting upon the nuclei and is equal to,

$$\boldsymbol{T} = \boldsymbol{M} \times \boldsymbol{B} \tag{2.14}$$

Therefore the presence of a magnetic field causes the magnetic moments of the nuclei to precess, in turn leading to precession of the bulk magnetisation vector. From equation 2.4 the bulk magnetisation can be rewritten as a function of the total spin angular momentum.

$$\boldsymbol{M} = \gamma \boldsymbol{L_S} \tag{2.15}$$

Combining equations 2.13, 2.14 and 2.15 it is possible to derive an expression for the rate of change of the bulk magnetisation as a function of time.

$$\frac{d\boldsymbol{M}}{dt} = \gamma \boldsymbol{M} \times \boldsymbol{B} \tag{2.16}$$

If equation 2.8 is substituted into this relation it can be shown that the frequency of this precession is equal to the Larmor frequency, ω_0.

$$\frac{d\boldsymbol{M}}{dt} = \boldsymbol{\omega} \times \boldsymbol{M} \tag{2.17}$$

If an ensemble of spins, with randomly and isotropically distributed magnetic moments, are placed in a magnetic field the magnetisation vector, $\boldsymbol{M}$, will begin precessing about an axis parallel to that field. This is conventionally designated the z-axis. In this special case, where relaxation effects are ignored, this vector will also have a persistent component in the transverse x-y plane. The magnetisation vector will trace out a precessional cone as detailed in figure 2.3. However this is unrealistic, as stated in the introduction to this section. Section 2.2.6 discusses relaxation processes that cause this component of the magnetisation in the transverse plane to decay.

2.2.5 Excitation

In practice the NMR experiment uses an oscillating magnetic field to manipulate the energy states of an ensemble of spins. This magnetic field is termed B_1 and oscillates in the radio frequency band.

$$\boldsymbol{B_1} = \begin{pmatrix} B_1 \cos \omega t \\ B_1 \sin \omega t \\ 0 \end{pmatrix} \tag{2.18}$$

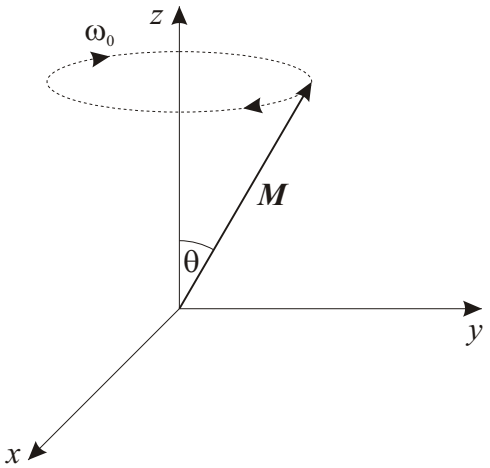

Figure 2.3: Precessional cone of the bulk magnetisation vector, $\boldsymbol{M}$, around the magnetic field $B_0\boldsymbol{k}$.

At this point it is useful to transform equation 2.16 into a frame of reference rotating with respect to the z-axis at the Larmor frequency, ω_0. Axes x, y and z are then transformed into x', y' and z' to give,

$$\frac{d\boldsymbol{M}}{dt} = \gamma \boldsymbol{M} \times \boldsymbol{B_{eff}} \tag{2.19}$$

where $\boldsymbol{B_{eff}}$ is the effective magnetic field in the rotating frame and incorporates the effects of B_1.

$$\boldsymbol{B_{eff}} = \begin{pmatrix} B_1 \cos \omega t \\ B_1 \sin \omega t \\ B_0 - \frac{\omega_0}{\gamma} \end{pmatrix} = \begin{pmatrix} B_1 \\ 0 \\ 0 \end{pmatrix} \tag{2.20}$$

The effect of this transformation into the rotating frame is to remove the time dependence of B_1 and to reduce the apparent magnetic field by $\frac{\omega_0}{\gamma}$. As this relation is equivalent to B_0 this serves to remove the z'-component of the total magnetic field for spins that are on resonance. Therefore the application of a B_1 field causes the magnetisation to rotate away from the z-axis through an angle θ, see figure 2.4. In the laboratory frame this would be equivalent to increasing the angle between the precessional cone and the z-axis. This

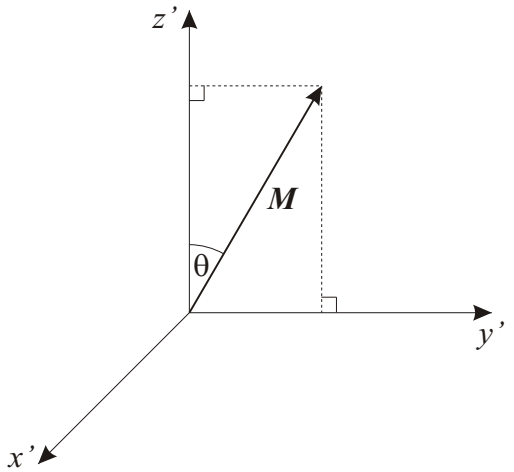

Figure 2.4: Magnetisation in the rotating frame following a θ° RF pulse.

angle is a function of the amplitude of the B_1 pulse and its duration, τ, for a constant amplitude pulse.

$$\theta = \gamma B_1 \tau \tag{2.21}$$

A given flip angle can be attained either by a short, high amplitude pulse or a longer duration, low amplitude pulse.

2.2.6 Relaxation

In section 2.2.4 it was assumed that relaxation does not exist, in order to simplify the initial derivation. However in practice several mechanisms act to return the bulk magnetisation to equilibrium. Longitudinal relaxation of the z-component of the magnetisation occurs as the spins exchange energy with their surroundings. Transverse relaxation acts to return magnetisation in the $x - y$ plane to zero. This is achieved by the mutual interaction of the spins. Both relaxation mechanisms are characterised by time constants T_1 and T_2, respectively. In practice a pure T_2 relaxation is not observed. Inhomogeneities in the magnetic field experienced by the spins causes an additional relaxation term, T_2', to be incorporated. This produces the observed

T_2^* decay constant.

$$\frac{1}{T_2^*} = \frac{1}{T_2} + \frac{1}{T_2'} \tag{2.22}$$

The effects of relaxation can be incorporated into the mathematical description of magnetisation to produce the general form of the Bloch equations.

$$\frac{d\boldsymbol{M}}{dt} = \gamma \boldsymbol{M} \times \boldsymbol{B_{eff}} - \begin{pmatrix} M_x'/T_2 \\ M_y'/T_2 \\ (M_z' - M_0)/T_1 \end{pmatrix} \tag{2.23}$$

The magnetisation is represented by $\boldsymbol{M}$ and its components in the x', y' and z' dimensions. The magnetisation at equilibrium is represented by M_0.

For spin-$\frac{1}{2}$ particles the dominant relaxation mechanism is the dipolar coupling between two spins. Chemical shift anisotropy (CSA) also makes a significant contribution in macromolecular liquid systems. In both cases the relaxation is caused by the rapidly fluctuating magnetic fields produced by these processes. Spins within the sample tumble through space due to the thermal energy they possess. In direct dipole-dipole coupling the field imposed by one spin on the other is rapidly changing due to the relative motion of the two particles. Magnetic fields caused by the CSA effect are due to molecular electron currents induced by the external magnetic field. Together these processes add to the external field at each spin location to produce a tiny variation in both magnitude and direction of that field. For a given spin location this field will have zero mean and can be quantified by the mean square value.

$$< B_x(t) > \;=\; 0 \tag{2.24}$$

$$< B_x^2(t) > \;\neq\; 0 \tag{2.25}$$

The rate at which the field fluctuates can be determined using an autocorrelation function, $\mathbb{G}$. The correlation of the field over different time scales, τ, can then be determined.

$$\mathbb{G}(\tau) =< B_x(t) B_x(t+\tau) > \tag{2.26}$$

Correlation is generally large for small values of τ and zero for large values of τ. A model of this variation is generally assumed to be mono-exponential decay, where τ_c is known as the correlation time.

$$\mathbb{G}(\tau) =< B_x^2 > e^{-|\tau|/\tau_c} \tag{2.27}$$

The spectral density, $\mathbb{J}$, of the random field fluctuations is defined as twice the Fourier transform of the auto-correlation function.

$$\mathbb{J}(\omega) = 2\int_0^\infty \mathbb{G}e^{-\imath\omega\tau} \tag{2.28}$$

Rapidly fluctuating fields result in short correlation times and a broad spectral density. Conversely slowly changing fields have longer correlation times leading to a narrower spectral density. For an auto-correlation function of the form of equation 2.27 the normalised spectral density, $\mathcal{J}$, can be expressed by the following equation. Normalisation is performed with respect to the area under the curve.

$$\mathcal{J}(\omega) = \frac{\tau_c}{1+\omega^2\tau_c^2} \tag{2.29}$$

Relaxation is governed by transitions between spin states brought about by thermal motion of molecules in the system. Transitions between states are achieved when a spin is subjected to a magnetic field with a frequency equivalent to the spin's own resonant frequency, or harmonics thereof. In liquids the correlation time of the randomly modulated field corresponds to the rotational correlation of these molecules. Hence the spectral density function describes the probability of a spin moving from one state to another. The Solomon equations formalise this link and predict T_1 as a function of spectral density for the dipole-dipole interaction.

$$\frac{1}{T_1} = \frac{3}{10}b^2\{\mathcal{J}(\omega_0) + 4\mathcal{J}(2\omega_0)\} \tag{2.30}$$

The function $\mathcal{J}(n\,\omega_0)$ represents the spectral density at the n^{th} harmonic of the resonant frequency and b is the dipolar coupling constant,

$$b = -\frac{\mu_0}{4\pi}\frac{\hbar\gamma^2}{r^3} \tag{2.31}$$

where r is the distance between a pair of spins. Similarly an expression for T_2 can be found.

$$\frac{1}{T_2} = \frac{3}{20} b^2 \{3\mathcal{J}(0) + 5\mathcal{J}(\omega_0) + 2\mathcal{J}(2\omega_0)\} \tag{2.32}$$

Therefore the relaxation times T_1 and T_2 vary as a function of magnetic field. The spectral density of the rotational correlation times is independent of field. Therefore as the magnetic field increases the spectral density will vary at harmonics of the Larmor frequency, ω_0.

As noted above, the T_2' component of T_2^* is brought about by inhomogeneities in the magnetic field experienced by the spins. Aside from the inherent inhomogeneties of the external magnetic field, local fields are caused by the magnetic susceptibility, χ, of the sample. This modifies the resultant field at the spin location to give an effective magnetic field, B_{eff}.

$$B_{eff} = B_0(1 + \chi) \tag{2.33}$$

Where discontinuities in the sample are present, for example at sample boundaries, magnetic field gradients are produced. This causes an increase in spin dephasing, which reduces T_2^*. However this effect can be used in a beneficial way. For example by introducing a paramagnetic species into the blood stream, the contrast between blood vessels and tissue can be enhanced. The most common *contrast agents* contain Gadolinium, although Dysprosium has also been used as a shift agents.

2.2.7 A Simple Pulse Sequence

The simplest NMR experiment consists of a single RF excitation pulse. The sample, when placed in a magnetic field, is allowed to reach thermal equilibrium by relaxation of the previously disordered bulk magnetisation. The excitation pulse is applied to the sample at the spin resonant frequency, and longitudinal magnetisation is rotated into the transverse plane. Previously randomly distributed spin magnetisation vectors are brought into phase. This is followed by a short-lived decay, known as the free induction

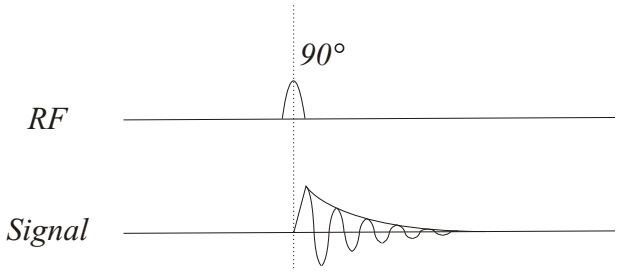

Figure 2.5: A simple pulse sequence.

decay (FID). The FID induces a signal in the RF coil. This signal is then amplified and recorded and represents the decay of transverse magnetisation due to T_2 and magnetic field inhomgeneity effects. Figure 2.5 describes this sequence diagrammatically.

2.2.8 Spin Echoes

The spin echo is critical to an extensive range of NMR techniques. It allows the magnetisation of the spin ensemble to be brought back into phase to produce what is known as a spin echo. This can be achieved in several ways, but two of the most common techniques are the Hahn spin echo and the gradient echo.

Following a 90°_x RF excitation pulse, the phase coherence of the induced transverse magnetisation begins to disperse. This dephasing effect is caused by inhomogeneities in the magnetic field, either inherent or due to susceptibility shifts within the sample. Using the method of Carr and Purcell (CP) [28] a 180°_x pulse is applied to the sample at a time τ. This causes the magnetisation that was initially oriented along the $+y$ axis to be flipped onto the $-y$ axis. Following a further time period τ phase coherence returns and an echo is formed. The phase accumulation of three spins, subjected to different field inhomogeneities, is shown schematically for the rotating frame in figure 2.6. Initially the differing inhomogeneities experienced by each spin causes the range of phase values to fan out, with those experiencing the

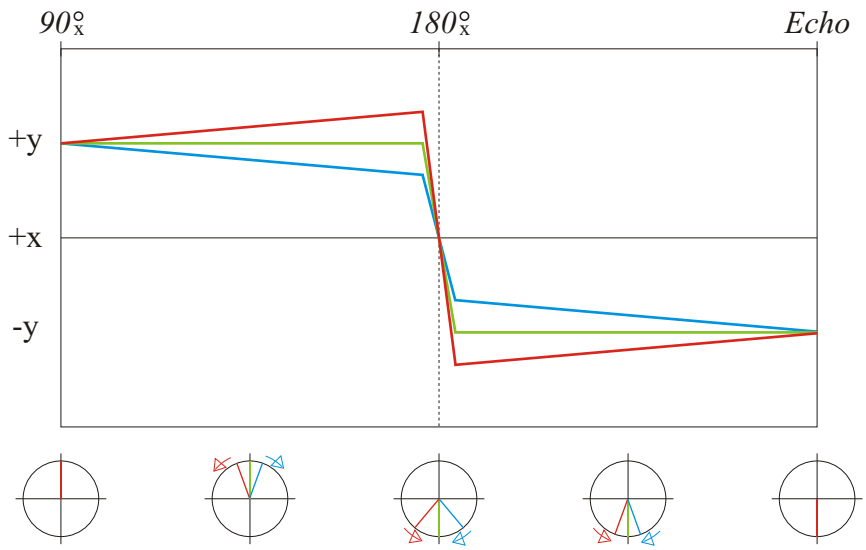

Figure 2.6: Hahn spin echo phase evolution.

largest effect accumulating the greatest phase difference. The 180°_x pulse causes the magnetisation to be mirrored through the x-axis. However phase changes continue to accumulate in the same sense, causing the magnetisation to become increasingly refocused along the $-y$ axis. In an alternative form of this sequence a 180°_y pulse can be applied, which mirrors the magnetisation through the y-axis, but allows the phase accumulation to continue in the same direction. Using a sequence such as this refocuses dephasing caused by static field inhomogeneities. Therefore by repeat application of this method for different τ values, known as echo times, it is possible to measure T_2. This sequence is often described as a Hahn spin echo, however this is not strictly true as in Hahn's original work [29] refocussing was performed by a second 90° RF pulse.

In the gradient echo pulse sequence, refocusing is instead performed using magnetic field gradients. Following the 90° RF pulse, an initial gradient is applied for a time τ, causing dephasing of the spin ensemble. This gradient is immediately followed by a gradient of the same magnitude, but with reversed polarity for a time 2τ. This causes the spins to become increasingly in phase,

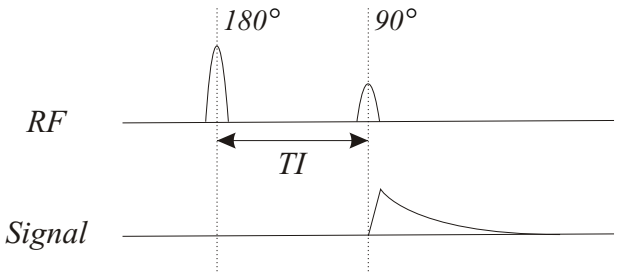

Figure 2.7: Inversion recovery pulse sequence for measuring R_1.

reaching a maximum at halfway through the second gradient application. Unlike the CP spin echo, phase dispersion due to field inhomogeneities is not refocused. Instead it contributes an additional T_2' component.

2.2.9 Relaxometry

The science of the measurement of NMR relaxation rates is known as relaxometry. The relaxation time constants have their associated relaxation rate.

$$R_i = \frac{1}{T_i} \qquad i = 1, 2 \tag{2.34}$$

The longitudinal relaxation rate is often measured using an inversion recovery technique. Figure 2.7 shows a simple inversion recovery pulse sequence. An initial 180° inversion pulse is followed a time TI later by a 90° pulse. This flips the current longitudinal magnetisation into the transverse plane where an NMR signal can be measured. Hence the magnitude of M_z is dependent on TI and R_1. Ideally the shortest possible echo time following the 90° pulse is used to maximise the acquired signal.

$$M_z = M_0(1 - 2e^{-TI\,R_1}) \tag{2.35}$$

Therefore by repeating this experiment for a range of TI values it is possible plot out the T_1 recovery of the longitudinal magnetisation. There are several important considerations to be made when performing this experiment. Firstly, when using equation 2.35, it is important that the longitudinal

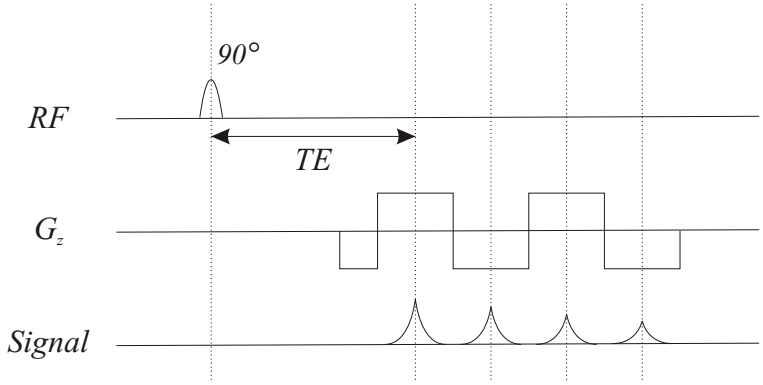

Figure 2.8: Gradient echo pulse sequence for measuring R_2^*.

magnetisation be allowed to fully recover before the experiment is repeated. Secondly equation 2.35 is strictly only true for a perfect 180° pulse, especially at high field. In practice this can be difficult to achieve due to inhomogeneities in the B_1 field. Therefore a generalisation of this equation can be derived for any arbitrary pulse angle, θ.

$$M_z = M_0(1 + (\cos\theta - 1)e^{-TI\,R_1}) \tag{2.36}$$

The transverse relaxation rate R_2^* is measured using a simple gradient echo technique. Figure 2.8 describes the timing of this pulse sequence. Following a 90_x° pulse, gradient echoes are formed by repeatedly reversing the polarity of the magnetic field gradient. This will yield multiple signal measurements at various echo time delays. Assuming that the the signal decay is mono-exponential, the magnetisation in the y dimension, M_y, is then dependent on the echo time, *TE*.

$$M_y = M_0 e^{-TE\,R_2^*} \tag{2.37}$$

In order to measure R_2 the effect of static field inhomogeneities needs to be taken into account. The simplest measurement technique utilises multiple repeats of the CP spin echo sequence, described above. These measurements trace out the exponential decay of M_y as a function of *TE*, enabling the

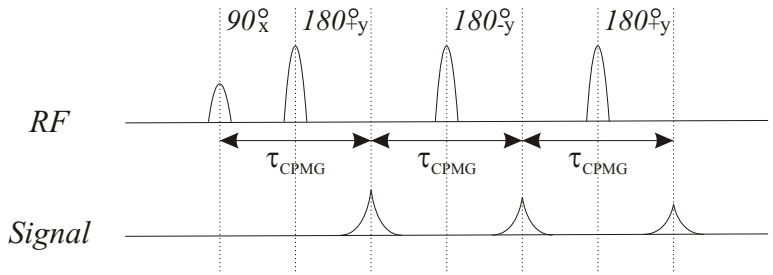

Figure 2.9: CPMG pulse sequence for measuring R_2.

calculation of T_2.

$$M_y = M_0 e^{-TE\ R_2} \tag{2.38}$$

However this sequence does not rewind dephasing due to diffusion. To measure a more accurate value of T_2 the Meiboom-Gill modification [30] of the CP spin echo technique [28] is used. This is known as the Carr-Purcell-Meiboom-Gill technique, or CPMG. Figure 2.9 displays the timing of a CPMG sequence. In common with the CP spin echo a 90°_x is followed by a series of 180° pulses. However this pulse is applied with a 90° phase shift with respect to the initial pulse by applying the 180° pulse along the y-axis. This yields a spin echo at time 2τ. The 180° pulse is then repeated with alternating phase, denoted in figure 2.9 by $+y$ and $-y$, for odd and even repeats. By alternating the phase of each 180°pulse imperfections in the pulse profile are balanced out. Therefore signal should only be acquired following pairs of 180°pulses. The echo spacing is described by τ_{CPMG} and is equal to 2τ. By keeping τ short the effect of diffusion can be minimised.

2.3 Magnetic Resonance Imaging

In the decades that followed the discovery of NMR, this fundamental property of matter had a large impact on a wide range of scientific fields. In particular the technique of NMR spectroscopy flourished. Work performed in the following decades would lead directly to several Nobel prizes for both

Physics and Chemistry.

In the first half of the 1970's a great amount of interest was generated in the idea of producing images using NMR, so called NMR imaging. Paul Lauterbur [3] realised that by applying a magnetic field which varied across the sample, local variations in the proton Larmor frequency could be induced. This enabled the spatial distribution of protons to be measured. This one-dimensional proton density profile could then be projected through space. By varying the angular orientation of the magnetic field gradient a number of projections could be acquired and back-projected [31]. This allowed an image of the sample to be produced. Lauterbur coined the term *zeugmatography* to describe this technique. This term is rarely used, and today NMR imaging is more commonly known as MRI (Magnetic Resonance Imaging).

At around the same time Peter Mansfield was working on an NMR technique to investigate crystal lattice structure in solids [4]. Due to limitations in their apparatus, resolving the structure of CaF_2 proved very difficult. Instead artificial one-dimensional lattices were produced using thin sheets of camphor. Later Mansfield acknowledged that by choosing to work with solids they had made the task far more difficult [6]. However, by making an analogy between optical diffraction and the Fourier transform of the NMR signal, Mansfield was able to thoroughly describe the imaging problem in terms of reciprocal space. By visualising the problem in this way it made it possible to imagine many ways to adequately sample this space and thus create an image.

Whilst both of these pieces of work added immeasurably to the nascent field of MRI they represent a small part of any imaging technique. The following sections describe the major components of an MRI pulse sequence.

2.3.1 Reciprocal Space

In 1973, Mansfield and Grannel [4] produced a generalised theory of how imaging could be performed using NMR. They noticed that when the NMR signal was transformed to reciprocal space there were strong mathematical

similarities between the resulting expression, and those used to describe diffraction of a plane wave.

When the spins within the sample are excited by an RF pulse, and are subject to time dependent magnetic field gradients, the resultant NMR signal can be described by the following expression,

$$S(t) = \int d\boldsymbol{r}\rho(\boldsymbol{r}) \;\; exp\left(\imath\gamma \int_0^t \boldsymbol{r}\cdot\boldsymbol{G}(t')dt'\right) \tag{2.39}$$

where $\rho(\boldsymbol{r})$ is the spin density at position $\boldsymbol{r}$. The magnetic field gradients, $\boldsymbol{G}$, are conventionally applied in three orthogonal dimensions; x, y and z.

$$\boldsymbol{G}(t') = \begin{pmatrix} dB_z(t')/dx \\ dB_z(t')/dy \\ dB_z(t')/dz \end{pmatrix} = \begin{pmatrix} G_x \\ G_y \\ G_z \end{pmatrix} \tag{2.40}$$

As was noted above, it is possible to perform a transformation to the reciprocal space domain. The reciprocal space domain represents the spatial frequencies present in the image. The transformation is achieved through the following parameter.

$$\boldsymbol{k} = \gamma \int_0^t \boldsymbol{G}(t')dt' \tag{2.41}$$

Reciprocal space is often known as *k-space* in reference to the wave vector, $\boldsymbol{k}$. This vector has an associated wavelength, λ.

$$\lambda = \frac{2\pi}{|\boldsymbol{k}|} = \frac{2\pi}{k} \tag{2.42}$$

Applying the k-space transformation to equation 2.39 gives,

$$S(k) = \int d\boldsymbol{r}\rho(\boldsymbol{r}) \;\; exp\left(\imath\boldsymbol{k}\cdot\boldsymbol{r}\right) \tag{2.43}$$

Application of the Fourier transform to this equation then yields the spin density at any point across the sample.

$$\rho(\boldsymbol{r}) = \int d\boldsymbol{r}S(k) \;\; exp\left(-\imath\boldsymbol{k}\cdot\boldsymbol{r}\right) \tag{2.44}$$

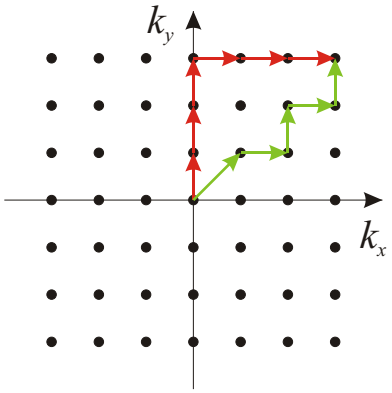

Figure 2.10: An example of the multiple ways in which a traversal across k-space can be achieved.

This suggests that in order to produce an image of an object, k-space must be sufficiently well sampled. For time dependent gradients the exponent of equation 2.44 can be expanded.

$$\boldsymbol{k} \cdot \boldsymbol{r} = \begin{pmatrix} xk_x \\ yk_y \\ zk_z \end{pmatrix} \tag{2.45}$$

The variables k_x, k_y and k_z are independent dimensions of the $\boldsymbol{k}$ vector. By allowing the x, y and z dimensions of the gradient $\boldsymbol{G}(t')$ to be modulated independently in time it is possible to contemplate many k-space sampling schemes. Figure 2.10 illustrates the variety of ways of moving between two arbitrary positions in a two-dimensional example of k-space. The ways in which movements through k-space are achieved are described in the following sections.

2.3.2 Spatial Encoding

Great care is taken when designing magnets for NMR applications to produce a highly homogenous magnetic field. However by introducing a carefully controlled magnetic field inhomogeneity it is possible to gain information

about the distribution of spins in a sample. In the simplest implementation of this idea a one-dimensional magnetic field gradient, G_x, is applied, in this case in the x-dimension. The resultant magnetic field, B_z, in the z-dimension at point x is,

$$B_z(x) = B_0 + G_x(x) \tag{2.46}$$

Evidently this can easily be expanded to three orthogonal dimensions, in order to produce a gradient in any arbitrary direction. By substituting this supplemented magnetic field into equation 2.8 a spatial variation in the Larmor frequency is observed.

$$\omega(x) = \gamma(B_0 + G_x(x)) \tag{2.47}$$

Spins located at each point in the sample corresponding to a given value of x will precess at the same frequency. The FID will, therefore, consist of frequency components corresponding to each value of x. The Fourier transform of the FID will give the spin density of the sample in the x direction, see figure 2.11. Extending this process to three-dimensions allows an image to be formed. This technique was the first to be used to produce images [3] and is known as projection reconstruction, see section 2.3.4.

However, *frequency encoding* is not the only way to impose spatial dependence on the NMR signal. An alternative, although often complementary, technique is that of *phase encoding*. Rather than rely on the frequency of the spin precession this method is dependent on a spatial variation in phase. This is possible due to the way the NMR signal is detected. This measurement approach is known as quadrature signal detection and allows measurement of phase information as well as frequency.

Following excitation of the spin ensemble a magnetic field gradient is applied. In this example a y gradient is applied with an amplitude, G_y, and a time, t_y.

$$\phi = \gamma G_y t_y y \tag{2.48}$$

This leads to an initial phase shift, ϕ, with respect to the original phase of the spins. Phase encoding is often used to allow traversal of k-space in

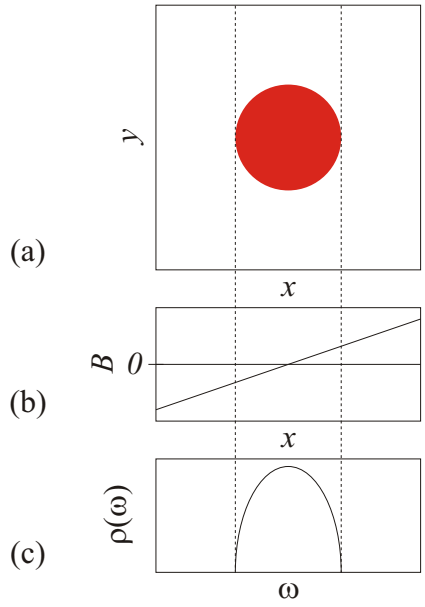

Figure 2.11: Application of a magnetic field gradient in the x-direction: (a) spatial variation of spin density in the sample, (b) applied magnetic field gradient and (c) frequency density plot.

the y direction and is a critical part of the spin warp [14] technique, see section 2.3.5.

2.3.3 Slice Selection

One of the most important elements of most acquisition strategies is *slice selection*. This technique allows a thin slab of spins within the sample to be excited, prior to the application of switched magnetic field gradients. Therefore spatial encoding is then only required in two-dimensions.

The most common slice selective pulse profile has the form of a sinc function. The suitability of this pulse profile for slice selection can be derived from first principles. If it is assumed that the pulse is applied for a short period of time, then it is appropriate to neglect relaxation effects. Hence the

magnetisation can be described by equation 2.16.

$$\begin{aligned} \frac{d\boldsymbol{M}}{dt} &= \gamma \boldsymbol{M} \times \boldsymbol{B} \\ &= -\gamma \boldsymbol{B} \times \boldsymbol{M} \end{aligned}$$

During application of a modulated magnetic field, B_1, and a magnetic field gradient, $B_z = G_z z$, the effective magnetic field, $\boldsymbol{B}$, in the rotating frame of reference is,

$$\boldsymbol{B} = \begin{pmatrix} -\gamma B_1 \\ 0 \\ -\gamma B_z \end{pmatrix} = \begin{pmatrix} \omega_1 \\ 0 \\ \omega_3 \end{pmatrix} \tag{2.49}$$

where ω_1 represents the magnitude of the RF field and ω_3 is the frequency offset with respect to resonance. Therefore,

$$\begin{aligned} \frac{d\boldsymbol{M}}{dt} &= \begin{pmatrix} \omega_1 \\ 0 \\ \omega_3 \end{pmatrix} \times \begin{pmatrix} M_x \\ M_y \\ M_z \end{pmatrix} \\ &= \begin{pmatrix} -\omega_3 M_y \\ \omega_3 M_x - \omega_1 M_z \\ \omega_1 M_y \end{pmatrix} \end{aligned} \tag{2.50}$$

By assuming that ω_1 is small it can be assumed that M_z has a constant value of M_0, i.e. very little longitudinal magnetisation is rotated into the transverse plane. This is known as the *low flip angle* approximation. The magnetisation in the transverse plane can then be expressed in terms of the complex transverse magnetisation, $\boldsymbol{M}_\perp = M_x + \imath M_y$.

$$\begin{aligned} \frac{d\boldsymbol{M}_\perp}{dt} &= \frac{dM_x}{dt} + \imath \frac{dM_y}{dt} \\ &= -\omega_3 M_y + \imath \omega_3 M_x - \imath \omega_1 \\ &= \imath \omega_3 (M_x + \imath M_y) - \imath \omega_1 \\ &= \imath \omega_3 \boldsymbol{M}_\perp - \imath \omega_1 \end{aligned} \tag{2.51}$$

By inspection it is noted that,

$$\begin{aligned} e^{-i\omega_3 T}\left[\frac{d\boldsymbol{M}_\perp}{dt} - \imath\omega_3\boldsymbol{M}_\perp\right] &= -\imath\omega_1 e^{-i\omega_3 T} \\ \frac{d}{dt}\left[e^{-i\omega_3 T}\boldsymbol{M}_\perp\right] &= -\imath\omega_1 e^{-i\omega_3 T} \end{aligned} \tag{2.52}$$

Integration of this relation, between time points $-T$ and $+T$, yields the transverse magnetisation following an RF pulse with a profile described by ω_1.

$$\boldsymbol{M}_\perp(t) = -\imath e^{\imath\omega_3 T}\int_{-T}^{+T}\omega_1(t)e^{-\imath\omega_3(t)t}dt \tag{2.53}$$

By substituting ω_1 and ω_3 for B_1 and G_z, respectively, it is possible to describe $\boldsymbol{M}_\perp(t)$ in more familiar terms.

$$\boldsymbol{M}_\perp(T) = \imath\gamma e^{-\imath\gamma G_z z T}\int_{-T}^{+T}B_1(T)e^{\imath\gamma G_z(t)zt}dt \tag{2.54}$$

Therefore the slice profile of the magnetisation is the Fourier transform of the RF pulse envelope, $B_1(t)$. To produce a rectangular slice profile involves calculating the Fourier transform of a top hat function. This produces the sinc function, $\sin x/x$. Equation 2.54 also states that the magnetisation of the plane normal to z has a 1^{st} order phase shift. This is easily removed by applying a subsequent gradient, with reversed polarity, for a time T. Alternatively for a spin echo sequence a gradient with the same polarity may be applied following inversion of the spin phases by a 180°pulse.

Strictly this derivation is only correct for low flip angles of the order of a few degrees. However sinc pulses work very well at much higher flip angles, and are routinely used to produce 90°pulses.

2.3.4 Projection Reconstruction

The first MR imaging technique [3] was introduced by Paul Lauterbur in 1973. This work was inspired by the back-projection techniques already in use in X-ray computed tomography (CT). It is commonly known as projection reconstruction (PR).

In the two-dimensional implementation of this technique, a slice selective pulse is initially applied. A one-dimensional frequency encoding gradient is played out during sampling. Multiple excitations are required to sample the whole of k-space by rotating the direction of the gradient in the imaging plane. Thus the sequence is time consuming. This is achieved by using two gradients in the x and y dimensions.

$$G = \sqrt{G_x^2 + G_y^2} \tag{2.55}$$

$$\alpha = \tan^{-1} \frac{G_y}{G_x} \tag{2.56}$$

The angle, α, formed by the resultant gradient, G, is rotated through 0° to 180°. The data gathered from each gradient orientation are then subjected to a one-dimensional Fourier transform, to produce a plot of spin density in that direction. A projection of the spin density is then plotted in a direction perpendicular to the applied gradient. Back-projecting each of these profiles produces an image of the object. Unfortunately, as can be seen in figure 2.14, this process leads to a substantial background signal caused when a projection assigns spin density where there should be none. This effect can be reduced by using a filtered back-projection method. In this approach a high-pass filter is applied to the spin density data, in the frequency domain. This filtered data is then back-projected, reducing unwanted background intensity.

2.3.5 Spin Warp

Traditionally the most commonly used clinical acquisition technique, the spin warp method [14] was introduced by the Aberdeen group in 1980. It is an improvement of an earlier technique known as Fourier zeugmatography [13].

Following a slice selective RF pulse a phase encoding gradient pulse is applied in the y direction. This is followed by acquisition of the signal during the frequency encoding x gradient. A single line of k-space is acquired during this process. The remainder of k-space is covered by repeating this sequence whilst changing the amplitude or timing of the phase encoding

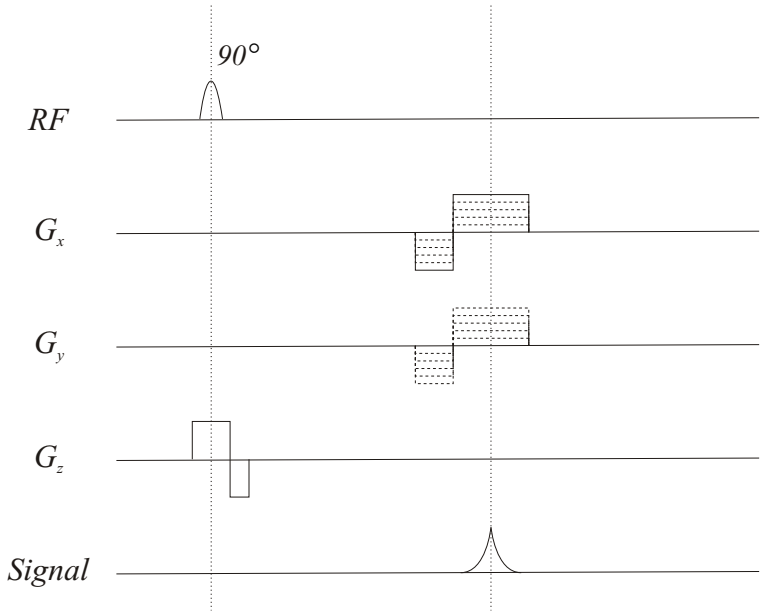

Figure 2.12: Projection reconstruction gradient echo pulse sequence diagram.

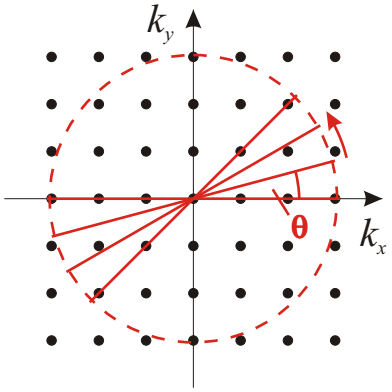

Figure 2.13: Projection reconstruction k-space trajectory.

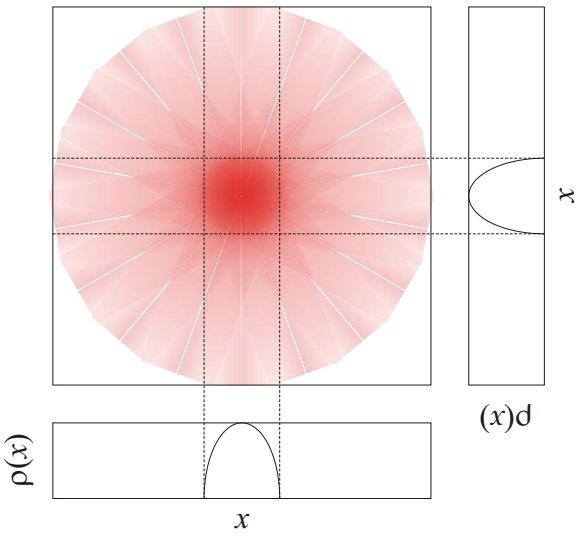

Figure 2.14: A simple example of back-projection reconstruction of a simple object.

gradient. Mathematically the reduction to two-dimensions simplifies equation 2.43 somewhat.

$$S(k_x, k_y) = \int dxdy\rho(x, y) \;\; exp\left(\imath\left(xk_x + yk_y\right)\right) \tag{2.57}$$

The wave numbers k_x and k_y describe the way in which k-space is sampled. In the y direction the addition of the variable n represents the step changes in G_y at the beginning of each k-space traversal.

$$k_x = \gamma G_x t_x \tag{2.58}$$

$$k_y = \gamma G_y n t_y \tag{2.59}$$

Application of a two-dimensional Fourier transform to the acquired data produces a two-dimensional proton density map in a single step.

$$\rho(x, y) = \int dxdyS(k_x, k_y) \;\; exp\left(-\imath\left(xk_x + yk_y\right)\right) \tag{2.60}$$

The subtle difference between the Fourier zeugmatography approach and that of spin warp is in the application of the phase encoding gradient. It is clear

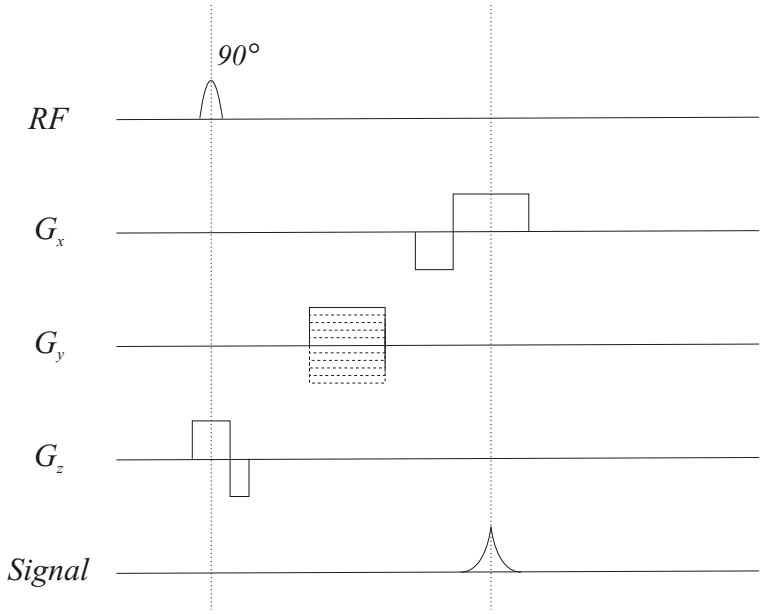

Figure 2.15: Spin warp pulse sequence diagram (Gradient echo variant).

from equation 2.59 that the overall induced phase shift is a function of time and gradient strength. Therefore the stepping of the phase encode gradient can be achieved by increasing the gradient strength and fixing the time or fixing the gradient strength and varying the time. The Fourier zeugmatography method uses the latter approach. This posed a problem in the early days of whole-body imaging as the homogeneity of magnet systems was not as high as it is today. From the calculations of Edelstein *et al.* [14] the contribution from the inhomogeneity of their magnet, at 20 cm from the iso-centre, was 12 μT. Contrast this with the gradient strength at this position, which was 20 μT, it is clear that this would lead to significant distortion. The spin warp technique solved this problem by maintaining a fixed gradient pulse length, but varying the gradient strength. The field inhomogeneity is still present but by keeping the gradient pulse the same length this extra phase shift is the same for each line of k-space.

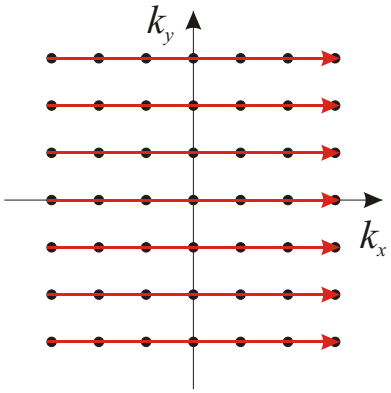

Figure 2.16: Spin warp k-space trajectory.

2.3.6 Echo Planar Imaging

The acquisition techniques described thus far have been inherently multi-shot techniques, requiring multiple excitations to form an image. However, in 1977 Peter Mansfield introduced the concept [12] of forming an image from a single RF excitation using a technique later named Echo Planar Imaging (EPI). Implementing this technique proved to be quite difficult due to the intensive gradient switching and the resultant magnetic field interactions with conductive structures of the magnet. All of the imaging performed in this thesis used EPI acquisition.

There are many different EPI implementations. One of the most successful, and an approach subsequently used in chapter 4, is the Modulus Blipped Echo planar Single pulse Technique (MBEST) [17]. The sequence, shown schematically in figure 2.17 begins with the conventional slice selection technique. An initial negative phase encoding gradient causes a traversal in the $-k_y$ direction, in order that the whole of k-space may be continuously sampled in the $+k_y$ direction. Similarly a negative frequency encode pulse places the sampling at the $-k_x$ extremity (figure 2.18). The frequency encoding gradient is then rapidly switched in order to produce a series of equally spaced spin echoes, acquiring k-space alternately in the $+k_x$ and $-k_x$ directions. Prior to each frequency encode lobe a short (blipped) phase encode

pulse increments k_y. When performing the two-dimensional Fourier transform of MBEST EPI data care must be taken to reorder alternate lines of k-space due to the opposing acquisition directions. However as odd and even lines of k-space are acquired under gradients of opposing polarity differences may exist between these gradients or their relative alignment. If these differences exist an artefact known as the Nyquist ghost can be observed. It is possible to remove this artefact by correcting the phase of the alternate lines of k-space. The correction method used in this thesis is described in section 2.5.4.

EPI suffers from several other artefacts. Chemical shift artefact in brain images is characterised by a bright halo shifted with respect to the brain. The protons present in fat and free water precess at a slightly different frequency due to their chemical environment. As the position of a given proton is frequency encoded this chemical shift causes a shift in position. Similarly inhomogeneities in the static magnetic field cause distortions in EPI images. Susceptibility differences in the head cause local magnetic field variations. In turn these variations cause the local precessional frequency to be shifted and hence the position of this volume to be shifted in the image.

Finally, in an extension to EPI is it possible to acquire 3-dimensional data in a single shot using Echo Volumar Imaging [18] (EVI). A second orthogonal phase encoding gradient is utilised to spatially encode a slab of the sample.

2.3.7 Partial Fourier Imaging

Partial Fourier imaging allows images to be reconstructed from insufficiently sampled k-space data. This is possible because the Fourier transform of a real object is Hermitian [31]. This means that the real part is symmetric and the imaginary part is asymmetric about the centre of k-space. Therefore, theoretically, only one half of k-space is required to reconstruct an image. In practice, due to imperfections in the instrumentation, the object is not purely real. By acquiring additional lines of k-space in the unsampled half of k-space it is possible to overcome this problem. The fraction of k-space

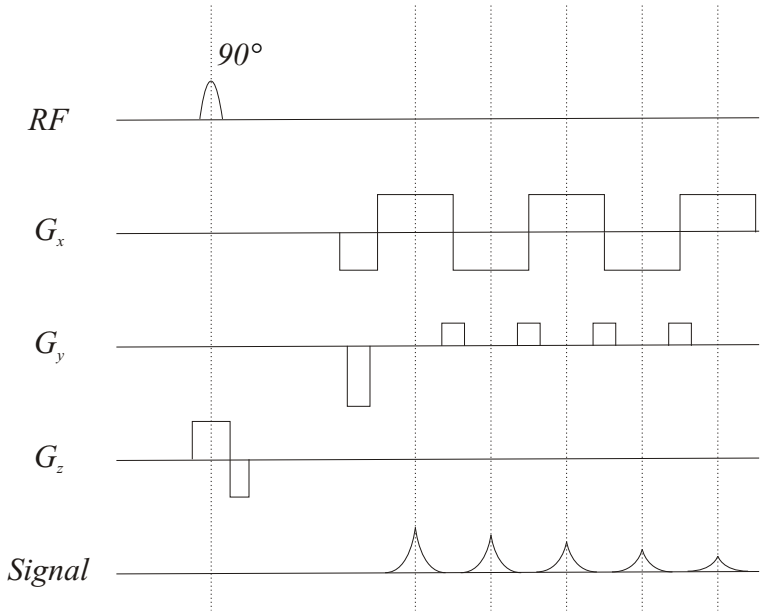

Figure 2.17: Echo Planar Imaging pulse sequence diagram.

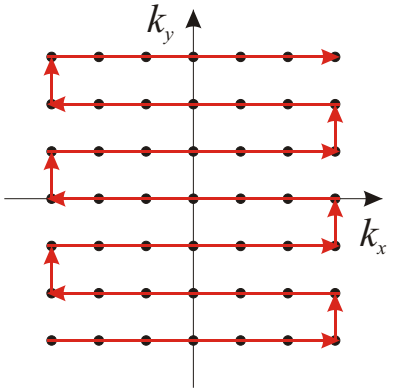

Figure 2.18: Echo Planar Imaging k-space trajectory.

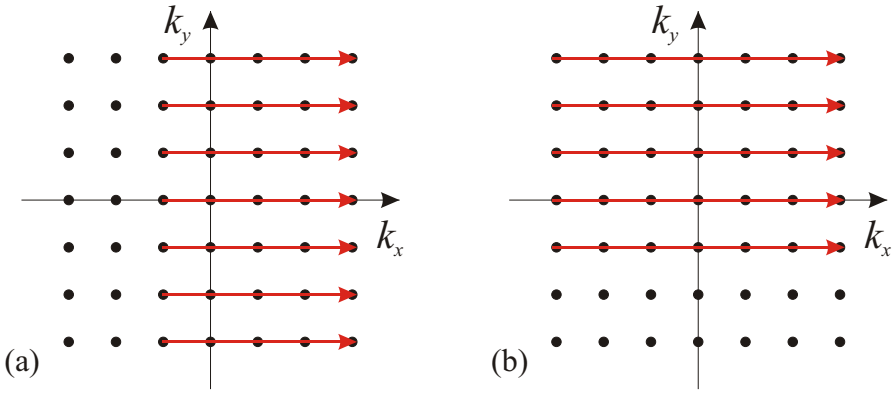

Figure 2.19: Partial Fourier acquisition in (a) the frequency encoding dimension and (b) in the phase encoding dimension.

is defined as 1 for full coverage and 0.5 for half coverage. In use the partial Fourier fraction is typically in the range 0.55−0.75, and is termed half scan on the Philips systems.

Applying the partial Fourier technique in the frequency encoding direction allows shorter echo times to be achieved. In the phase encoding direction, a reduction in scan duration can be achieved. In both cases the field of view is not affected but the signal to noise ratio (SNR) will be reduced and image artefacts introduced.

2.4 Instrumentation

The experiments described in this thesis were performed on four MRI systems based at at the University of Nottingham, see figure 2.20. The lowest field system, a Philips Achieva 1.5 T, was installed at the Brain and Body Centre in 2005. The remaining systems were based at the Sir Peter Mansfield Magnetic Resonance Centre. They include a custom-designed 3.0 T EPI scanner, a Philips Achieva 3.0 T and a Philips Achieva 7.0 T, the first to be installed in Europe. The Philips systems were installed in 2005 and the Nottingham system was developed in-house during the early 1990's. All of

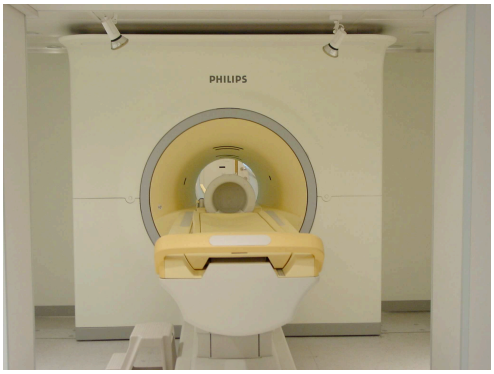

(a) Philips Achieva 7.0 T.

(b) Philips Achieva 3.0 T.

(c) Nottingham 3.0 T.

(d) Philips Achieva 1.5 T.

Figure 2.20: MRI systems used in this thesis.

these systems can be described in terms of four main components; control, magnet, gradient, RF subsystems.

2.4.1 Control

The MRI scanner is controlled by a computer workstation. The user enters the required scan parameters and the computer calculates the gradient and RF waveforms, along with timing information, to send to the spectrometer. Amplified signals are received by the spectrometer and passed back to the

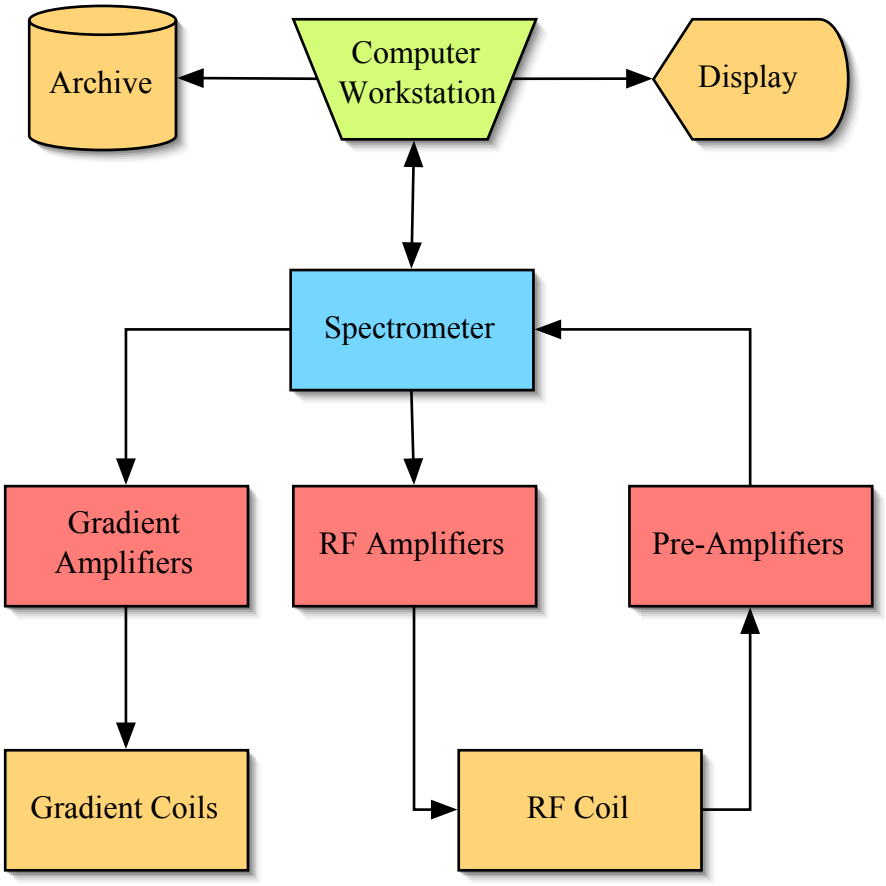

Figure 2.21: A schematic diagram of a typical MRI scanner.

computer to be reconstructed. The computer Fourier transforms the data and displays the image. The Nottingham 3.0 T saves the NMR signal as time data, which can be Fourier transformed off-line. The Philips systems save data in the DICOM format. There are also options to save the raw NMR signal for later reconstruction. Figure 2.21 shows a schematic diagram of a typical MRI scanner.

	Philips Achieva 1.5 T	Nottingham 3.0 T	Philips Achieva 3.0 T	Philips Achieva 7.0 T
Manufacturer	Philips	Oxford	Philips	Magnex
Field	1.5 T	3.0 T	3.0 T	7.0 T
Shielding	Active	None	Active	Fe Box
Cryogen	He	He / N_2	He	He
Cryocooler	✓	-	✓	✓
Bore	0.9 m	0.92 m	0.9 m	0.9 m
Length	1.57 m	2.5 m	1.57 m	3.4 m
Homogenity†	0.11	0.50	0.24	0.10
DSV	35 cm	30 cm	30 cm	25 cm
Fringe field‡	4 m / 3 m	16 m / 12 m	5 m / 3 m	12 m / 9 m

Table 2.2: Magnet system parameters for all four systems. †For the specified diameter homogenous spherical volume (DSV) at iso-centre. ‡Fringe field of 5 G measured axially / radially from iso-centre.

2.4.2 Magnets

The most common whole-body magnet systems rely on superconducting wire to produce very large magnetic fields. Typically this is a Niobium-Titanium (Nb-Ti) alloy wound into a solenoid. Ingots of Nb-Ti are drawn out to fine filaments, which are then bound together by solid Copper. This alloy is a type-2 superconductor with a critical temperature of 10 K [32]. Below this temperature the material becomes superconducting, that is it loses all resistance. However, this superconductivity can be destroyed by high magnetic fields, in this case 15 T [32], limiting the maximum magnetic field this magnet technology can produce. Higher fields are possible using a Niobium-Tin (Nb-Sn) alloy which has a critical field strength of 24.5 T [32], but this material is particularly brittle making it difficult to form wires for magnet production.

There are two main strategies for cooling the superconducting wires. The

Oxford magnet used in the Nottingham 3.0 T system uses liquid Helium as a cryogenic coolant. The liquid Helium cryostat is also cooled using liquid Nitrogen. Since liquid Nitrogen is relatively cheap it is allowed to boil-off in order to reduce the Helium boil-off rate and hence make the system more economical. Nitrogen gas is vented to the atmosphere, whilst Helium gas is piped to a liquefier allowing it to be reused in the School of Physics and Astronomy. Due to this relatively high boil-off rate, by modern standards, this magnet must be refilled with Nitrogen once a week and Helium once a month. The Philips and Magnex magnets differ slightly in their construction. They use a similar Helium cryostat but, instead of liquid Nitrogen, secondary cooling is provided by a cryocooler. This reduces boil-off to an even greater degree, reducing the frequency with which the system must be refilled with liquid Helium.

Due to the very high magnetic fields produced by superconducting magnets, siting a system can be very difficult. The magnetic field of the magnet travels way beyond the bore of the magnet and these *fringe fields* pose a risk to certain sections of the population. For instance heart pace makers can be caused to fail in relatively low magnetic fields and the torque imparted on aneurism clips can cause the implant to become dislodged with fatal consequences. In most cases an acceptable fringe field of 5 G is used when planning the installation of a magnet. The 5 G fringe field of the Oxford magnet, present in the Nottingham 3.0 T, is 16 m axially from the iso-centre and 12 m radially. In this case the 5 G line lies outside of the building and is isolated from the general public using shrubbery and fencing. Modern clinical systems use active shielding [15] to reduce this distance. This is achieved by placing additional counter wound loops around the ends of the superconducting solenoid. This causes the fringe field to decay far more rapidly and allows the 5 G line of the Phillips Achieva 3.0 T magnet to be reduced to 5.2 m axially and 3.0 m radially. Where active shielding is not suitable, i.e. at ultra high field (>7.0 T), one final recourse is passive shielding. By placing a large mass of ferromagnetic material, generally iron, around the magnet the

fringe field area can be substantially reduced. The Magnex 7.0 T magnet used in the Philips Achieva 7.0 T system uses this approach. Two hundred and thirteen tonnes of iron form a box surrounding the magnet and reduce the 5 G line to 12 m axially and 9 m radially.

A very high degree of homogeneity is required for both MRI and MRS (Magnetic Resonance Spectroscopy) applications. In MRI inhomogeneity leads to image distortion and in MRS to spectral line broadening. Superconducting magnets have inherently high homogeneity. This is improved further during installation of the magnet using passive shims. The passive shim set consists of a number of trays spread out around the bore that contain pockets in to which small pieces of ferromagnetic material can be placed [33]. After the magnet system is charged an initialisation sequence determines the current magnet homogeneity and determines the distribution of shim pieces to give optimum homogeneity. They are then placed within the pockets and are slid into place on rails. However, due to the effects of paramagnetism and diamagnetism within the sample this initial homogeneity can be reduced. Therefore a set of active shims are placed within the bore of the magnet. These shims consist of coil windings that produce a magnetic field which varies with position. First order shims vary linearly with position whereas second order shims vary quadratically. Currents are applied to the coil windings using stable power supplies to smooth out the distortions produced by the object being imaged. In the case of the Philips systems, these currents are determined automatically following several preparation steps which map out field inhomogeneity. The Nottingham system is set manually by the operator viewing a FID on an oscilloscope.

2.4.3 Gradients

The purpose of the gradient coil subsystem is to produce a spatial variation in the z-component of B_0 as a function of the three orthogonal directions x, y and z. A variation in the z-direction is conventionally achieved using a Maxwell pair coil arrangement, see figure 2.22. This system consists of

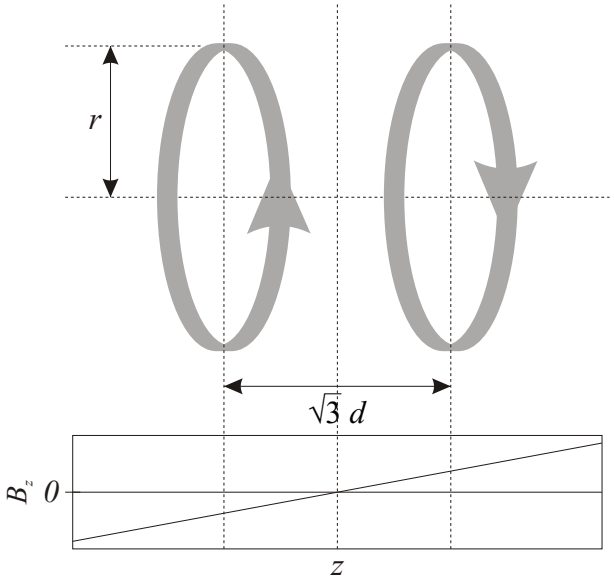

Figure 2.22: Maxwell pair coil arrangement [34].

a pair of coils with radius r, separated by a distance $\sqrt{3}d$, and yields a uniform magnetic field gradient with zero magnitude half way between the coils. This coil system is particularly well suited to MRI applications as it is easily integrated into a cylindrical geometry. Typically a magnetic field variation in the $x-y$ plane is accomplished using a saddle coil geometry. The Golay coil system uses two pairs of saddle coils distributed along the bore of the magnet, see figure 2.23. However simple coil elements such as this have been superseded by more advanced coil design techniques. Complex wire paths can be created through the use of numerical simulations.

Rapidly switching the magnetic field gradients can induce currents in nearby metal structures. This is a particular problem for MRI systems based on superconducting magnets. Currents induced in the cryostat and heat shield, which have low resistance, decay with long time constants destroying the intended gradient profile. This problem is exacerbated by the need to screen the far field of the magnetic field gradient. Further eddy cur-

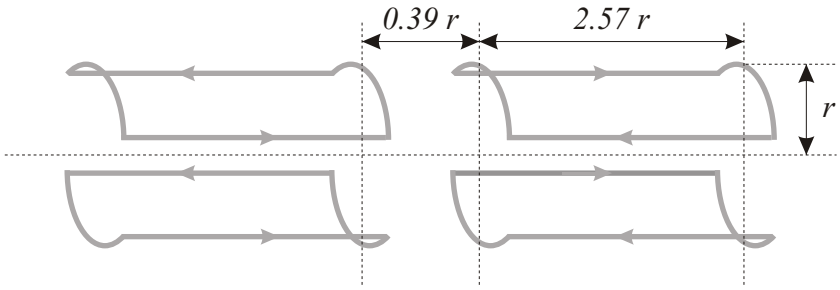

Figure 2.23: Golay coil arrangement [35].

rents are induced in this passive conductive screen. This effect limits the range of applications that can be implemented on a passively shielded system. However by using active shielding [15, 16, 36] techniques it is possible to obviate both of these problems. Extra coil windings are added between the magnet and the gradient coil to produce opposing magnetic fields, and hence null magnetic fields external to the gradient coil.

The currents required to drive the gradient coils, and hence produce the desired gradient profile, are digitally generated by the host console. These values are then converted to analogue voltages and fed to power amplifiers to generate the high currents required. Demanding acquisition techniques such as EPI require very rapidly switched magnetic field gradients. This requirement is made less demanding by using a resonant gradient coil design, such as that implemented on the Nottingham 3.0 T system. This enables it to produce switching frequencies up to 3.9 kHz. Different switching frequencies, ω, are achieved by modifying the capacitance, C, in the resonant circuit,

$$\omega = \frac{1}{\sqrt{LC}} \tag{2.61}$$

where L is the inductance. In practice the maximum switching frequency used in this thesis was 1.9 kHz.

The Philips systems use a non-resonant gradient design. All three systems have approximately similar specifications, see table 2.3. Both the 3.0 T and 7.0 T have a dual mode design. This allows the maximum amplitude of a

	Philips Achieva 1.5 T	Philips Achieva 3.0 T	Philips Achieva 7.0 T
Model	Nova	Quasar	Quasar
Mode	Single	Dual	Dual
Max. Amplitude†	66	40 / 80	30 / 60
Max. Slew Rate‡	160	200 / 100	100 / 50

Table 2.3: Gradient system parameters for the Philips MRI systems.†Units mT m^{-1}. ‡Units mT m^{-1} ms^{-1}.

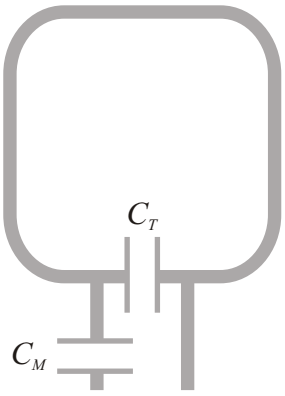

Figure 2.24: Simple RF coil design.

gradient pulse to be traded off against the maximum slew rate. This adds to the flexibility of the system.

2.4.4 RF

Spin excitation and signal reception are accomplished using RF coils tuned to the resonant frequency of the nuclei of interest. The simplest RF coil consists of a loop of wire connected to a capacitor in parallel, see figure 2.24. In addition the impedance of the RF coil must be matched to the impedance of the amplifier to maximise signal reception / transmission. By convention

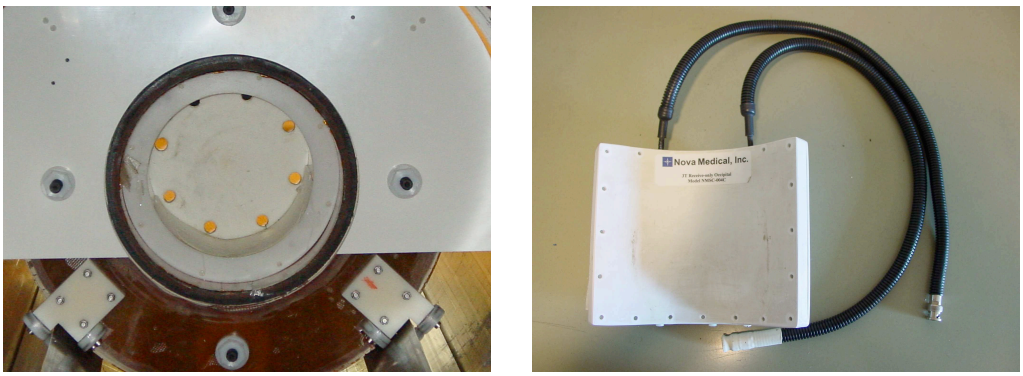

(a) Nova TEM transmit / receive coil. (b) Nova occipital receive coil.

Figure 2.25: Nottingham RF coils.

RF amplifiers have an impedance of 50 Ω. Another capacitor, C_M, connected in series is used to *match* the impedance whilst the capacitor, C_T, in parallel is used to *tune* the system to the Larmor frequency. A coil of this type could be used as a surface coil, allowing a specific region of the body to be studied with a high signal to noise ratio. When cross-sections of larger body parts are required, a volume coil is more appropriate. The most common volume coil design is known as a bird-cage coil.

The Nottingham system uses a TEM coil design and was built by Nova Medical. The data described in chapter 4 was acquired using the TEM transmit coil in conjunction with a quadrature occipital receive coil, also built by Nova Medical. This combination of coils allowed a homogenous RF field to be applied to the whole head, and high signal to noise images to be acquired from the anatomy of interest; the visual cortex.

The Philips systems have a number of interchangeable coils. The largest of these coils is the body coil and is based on a bird-cage design. This is largely used as a transmit coil, with reception using more localised coils, and is built into the bore of the system. Other coils include a quadrature Transmit / Receive (T/R) head coil and an 8-channel SENSE head coil. The 8-channel

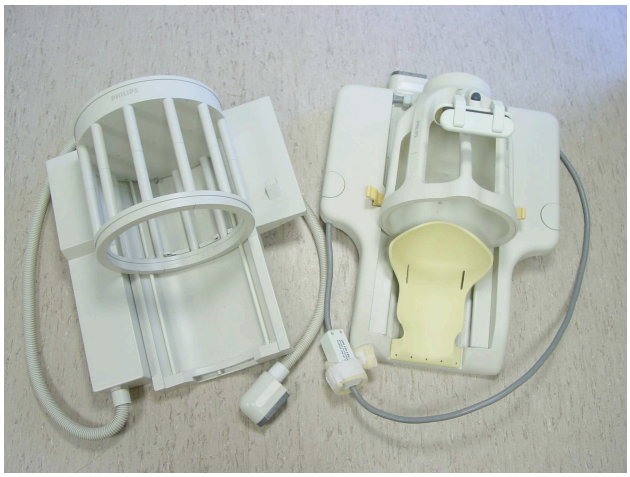

Figure 2.26: Philips' T/R (left) and 8-channel SENSE (right) RF coils.

SENSE head coil is a receive-only array allowing parallel imaging [37] to be performed. This is achieved by independently acquiring a reduced number of k-space lines from each coil element. Reducing the k-space coverage in this way reduces the field of view, causing each of the images to be wrapped in the phase encode direction. However an initial coil element sensitivity map (reference scan) is used to weight the reconstruction of a single unwrapped image from the 8 wrapped images. Currently the Philips Achieva 7.0 T system does not have a SENSE coil[1], hence the data acquired in chapter 3 used a T/R coil at all field strengths.

2.5 Functional Magnetic Resonance Imaging

The invention of EPI made it possible to *freeze* biological motion, due to the very short image acquisition time, allowing images free of motion artefact to be collected [17]. By applying this technique in a serial manner [38, 39] it was found that it was possible to detect functional changes *in-vivo* with unprecedented spatial resolution. The field of functional MRI (fMRI) grew

[1] A 16-channel SENSE head coil was delivered in April 2007

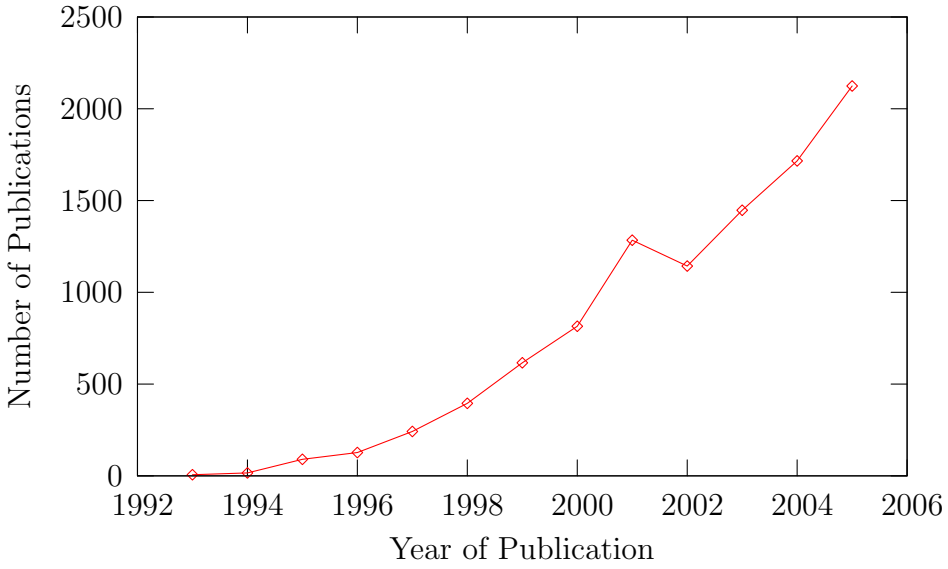

Figure 2.27: Growth in fMRI publications measured as the number of publications containing the keyword "fMRI" in the citation index Web of Knowledge.

rapidly during the 1990's, as can be seen in figure 2.27 by the increasing number of publications containing the keyword "fMRI".

The original, and most commonly used, fMRI technique utilises BOLD (Blood Oxygenation Level Dependent) contrast. This contrast mechanism relies upon the oxygenation level of the blood. Red blood cells within the blood contain haemoglobin, which under normal circumstances is diamagnetic. However deoxygenated haemoglobin is paramagnetic and hence forms local microscopic magnetic field gradients increasing proton dephasing. Neural activity is supported by a haemodynamic response in the local vasculature. This response leads to an increase in cerebral blood flow (CBF) to the active region. This serves to satisfy an increase in the rate of oxygen ($CMRO_2$) and glucose (CMRglu) metabolism by increasing the delivery of these substrates. In practice the haemodynamic response oversupplies the active region with oxygenated blood, increasing blood oxygenation down-

stream of the arteriole in the capillaries and veins. This reduces the concentration of paramagnetic deoxyhaemoglobin and hence reduces susceptibility induced dephasing. In turn this increases the MR signal. However the reasons for this mismatch are not fully understood and are the subject of ongoing research.

BOLD fMRI is by far the most common fMRI technique, but there are alternatives. Arterial Spin Labelling (ASL) techniques allow non-invasive measurements of CBF to be made, by magnetically *tagging* the blood water prior to its passage through tissue, enabling it to be used as a tracer. By monitoring the progress of this tagged blood water it is possible to quantify changes in longitudinal magnetisation and measure the modulation of CBF in response to a stimulus [40]. These measurements are arterially weighted and do not show changes in venous CBF as the tagged blood will have largely decayed prior to reaching the venous vasculature. Formerly these measurements were performed by injecting a paramagnetic tracer into the blood [41]. However such techniques are not easily repeatable as they rely on the passage of a single bolus of contrast agent limiting the utility of this method.

Similarly total cerebral blood volume (CBV) changes can be measured using contrast agents. This volume measurement consists of contributions from both the arterial and venous vessels. In humans this is achieved using techniques such as those described in chapter 4 of this thesis. Again the use of these techniques is limited and cannot be repeatedly used on a single subject. A further technique that does not suffer this problem is vascular space occupancy (VASO) fMRI [42]. By nulling the blood signal and measuring the effect of blood volume change on the tissue signal it is possible to perform CBV weighted measurements. This technique is hampered by a lack of quantitation [43] unlike contrast agent techniques.

2.5.1 Cerebral Vasculature

The arterial blood supply to the head is formed by the two common carotid arteries [44]. Each artery rises within the neck and bifurcates around the

level of the thyroid to feed the internal and external structures of the head. The exterior carotid supplies the exterior of the head, including the face and neck. The internal carotid artery supplies the intracranial space and is therefore more interesting in the context of this discussion. This vessel splits further forming a multitude of connecting vessels known as the circle of Willis. The importance of the brain can be appreciated from the many layers of redundancy built into the vascular network. For instance there are a pair of common carotid arteries, each of which branches from a different vessel of the thoracic network. The circle of Willis is a further example of this redundancy. If either of the carotid vessels were to become occluded this structure allows the redistribution of blood from the contralateral vessel in order to maintain tissue supply.

The cortical arterial system spreads out from the circle of Willis continually branching and reducing in size across the cortex. These branches are split into two types, long and short, and penetrate the cortex perpendicularly [45]. The long type pass through the grey matter in order to serve the white matter alone, whilst the short type only enter the grey matter. Further branching of the vasculature produces fine arteries known as arterioles. In turn the arterioles feed the capillary network either directly or through metarterioles that may serve 10-100 capillaries. Rather than terminate at the capillary bed, metarterioles connect to the venous system as so called *thoroughfare* channels. The capillary bed terminates when individual capillaries merge together to form venules, where blood collects prior to draining into the venous vasculature.

The surface of the cortex is drained via narrow diameter veins, which merge and connect with larger diameter vessels such as the superior sagittal sinus. Redundancy is maintained by linkage of several bilateral vessels at the cavernous sinuses. The blood continues to descend the intracranial cavity and joins the internal jugular veins. These vessels pass down into the neck alongside the internal and common carotid arteries [44].

Whilst the topology of the cerebral vasculature is important in functional

imaging, the morphology of those vessels is equally important. Arterial vessel walls consist of three layers [46]. The inner most layer is a base membrane called the endothelium, which lines the entire cardiovascular system. The intermediate layer provides the bulk of the thickness of the vessel and is formed from elastic fibres and smooth muscle fibres. This gives the vessel its strength and ability to cope with small changes in blood pressure. The final layer provides additional elastic fibres and collagen. Nerve fibres connect through this layer to the smooth muscle fibres allowing the tone of the vessel to be modulated to provide vasoconstriction or vasodilation. Arterioles close to the artery from which they branch differ only slightly from true arteries. They show a reduced diameter and contain less elastic tissue, the intermediate layer mainly consisting of smooth muscle. Arterioles close to the capillary bed show much reduced vessel wall thickness. The vessel wall is comprised of an endothelial membrane surrounded by smooth muscle fibres. The vessels described thus far control the haemodynamic response to increases in demand for oxygen and metabolites. The smooth muscle fibres allow the blood pressure into the capillary bed to be tightly regulated. At rest, perfusion of the capillary bed is maintained at a low level, but can be rapidly elevated by changing muscle tone within the arterial vasculature.

Capillary vessels are the narrowest vessel type and can be barely wide enough to accommodate a red blood cell passing through. The capillary vessel wall is formed purely by the endothelium. The function of the capillary is to exchange oxygen and metabolites for carbon dioxide and waste products. However cerebral capillaries differ from capillaries elsewhere in the body. They have an additional protective role that limits which molecules can pass through to the tissue space and forms the blood brain barrier (BBB). Unlike conventional capillaries, cerebral capillaries contain *tight junctions* in order to seal the gap between cells and produce a continuous blood vessel. It is possible for light molecules such as oxygen and carbon dioxide to diffuse through the endothelium and pericytes, but larger molecules cannot. Glucose has a specific transport mechanism through specialised membrane proteins.

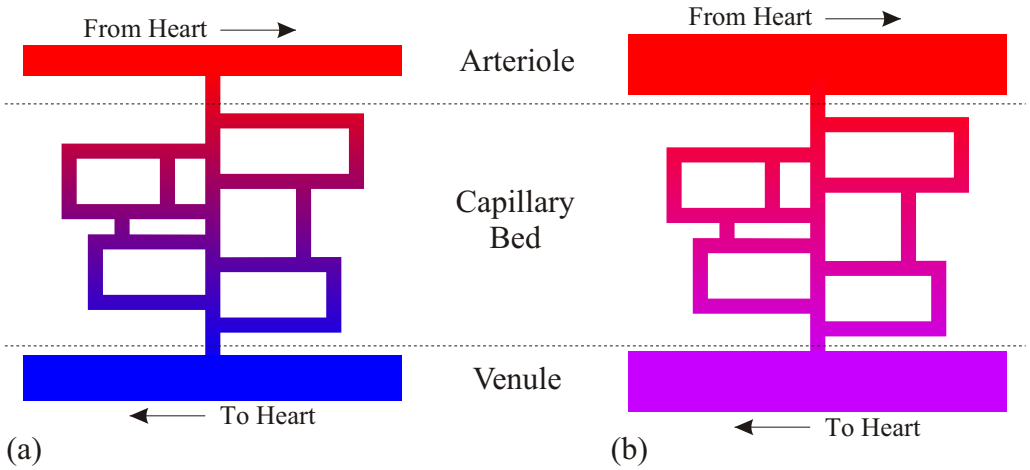

Figure 2.28: The cerebral vasculature (a) at rest and (b) during focal activation shown here for the situation where arterial and venous blood volume increases. Red and blue shading represent oxygenated and deoxygenated blood, respectively. Blended tones represent the mixed oxygenation states present in the capillary bed.

The vessel walls of veins consist of the same three layers as arteries, but with different thicknesses. The middle layer is considerably reduced with little smooth muscle, whilst the outer layer is the thickest and is constructed of collagen and elastic fibres. During functional activity increases in arterial blood pressure, and hence capillary blood velocity, are absorbed by expansion of the venule and smaller veins. The venous system is a passive system, due to a lack of smooth muscle and autonomic control, and hence changes in vessel diameter are driven by arterial pressure changes [47]. In general veins found in the rest of the body, particularly in the extremities, contain valves to prevent blood from flowing away from the heart. However in the brain these valves are absent.

2.5.2 BOLD Contrast

The purpose of the vasculature is to transport nutrients to tissue, and the medium through which this transport is achieved is blood. Blood is a suspension of cells dissolved in plasma. The plasma is a straw coloured liquid and is ∼92 % water [46], with the remainder formed by plasma proteins. The cells suspended within the blood are platelets, white blood cells and red blood cells. Red blood cells make up by far the greatest volume fraction of cells with ∼5 million cells per μl [46]. These cells increase the oxygen carrying capability of the blood by reversibly bonding oxygen molecules using haemoglobin molecules. This molecule consists of the globin protein and four iron containing haem molecules. Each iron ion reversibly combines with oxygen to produce oxyhaemoglobin. When required the reaction is reversed. Oxygen returns to the plasma space where it can be passed to tissue to fuel metabolism. Each red blood cell contains ∼280 million haemoglobin molecules allowing a large amount of oxygen to be carried. To aid the *absorption* of oxygen molecules these cells have a biconcave disc geometry in order to maximise their surface area.

The majority of the constituent components of blood have little effect on the MR signal, as they are only weakly diamagnetic. For instance the magnetic susceptibility shift of oxyhaemoglobin, relative to distilled water, is -0.26×10^{-7} [48], emphasising its diamagnetic nature. However deoxygenated haemoglobin (deoxyhaemoglobin) is paramagnetic with a relative magnetic susceptibility of $+1.57 \times 10^{-7}$ [48]. Water protons within the blood will experience enhanced dephasing causing a reduction in signal. As the volume fraction of blood in tissue is small this does not produce a marked effect. However, the magnetic susceptibility gradient formed by paramagnetic materials in the blood will enhance the dephasing of water protons diffusing around blood vessels. Assuming a cylindrical vessel aligned perpendicular to the field, the frequency shift due to this vessel can be expressed in polar

coordinates, r and θ, by the following relationship [49],

$$\frac{\omega_{local}}{\omega_0} = 2\pi\Delta\chi\left(\frac{a}{r}\right)^2(2\cos^2\theta - 1) \tag{2.62}$$

where ω_{local} is the local resonant frequency, a is the vessel radius and $\Delta\chi$ is the susceptibility shift between the vessel and the surrounding tissue. The polar coordinates r and θ represent the distance to the centre of the vessel and the angle of that line between that line and the z-axis. It is possible to substitute for $\Delta\chi = (1-Y)\Delta\chi_{dHb}$ in equation 2.62, where $\Delta\chi_{dHb}$ represents the deoxyhaemoglobin magnetic susceptibility relative to water. Assuming that the tissue has a susceptibility close to that of water, it is possible to simulate the effect of different oxygenation levels on local resonant frequency. Figure 2.29 displays the magnitude of this frequency shift in parts per million for three different blood oxygenation fractions (Y); 0.2, 0.5, and 0.8. Regions of tissue that are subject to these local field shift effects show increased proton dephasing and hence a reduction in MR signal. The effect of reduced blood oxygenation on the MR signal is therefore not confined to the vessel. Extravascular dephasing causes highly deoxygenated blood vessels to appear as dark lines in MR images. Dephasing is greatest when the vessel is perpendicular to the main magnetic field, and zero when oriented parallel. Fortunately the tortuosity of the cerebral vasculature means that there is almost always a component of the vessel that is perpendicular to the main magnetic field. This may, however, be a problem for structures of the brain that have an anisotropic distribution of vessels.

As large vessels cause a static dephasing effect the measured contrast is dependent on the imaging technique employed. Gradient echo techniques are used to create good contrast between blood vessels and tissue. Large blood vessels containing deoxygenated blood produce large frequency shifts in the surrounding tissue and hence good contrast between them. By employing a spin echo technique [50], it is possible to refocus this dephasing. However dephasing due to protons diffusing around very small vessels cannot be refocused. Mobile water protons that undergo a large displacement, during a TE period, with respect to the vessel diameter will dynamically average the

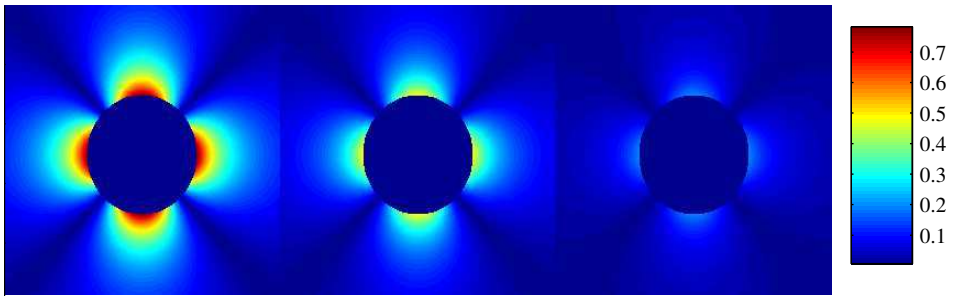

Figure 2.29: Simulation of the frequency shift due to a blood vessel of radius $a = 1$ in parts per million. Three blood oxygenation fractions were simulated, Y=0.2, 0.5, 0.8 (left-right).

vessel magnetic field gradient. This stochastic dephasing cannot be refocused and hence this contribution is retained. A lot of research [50–53] has been performed in this area with the aim of using SE to provide better localisation of neural activity.

Initially BOLD contrast was used to improve venous vessel contrast [54] by altering the inspired air mixture of mice and rats. Ogawa *et al.* noted that the type of anaesthetic used in these experiments had a bearing on the overall contrast, suggesting that it must alter cerebral haemodynamics by modulating blood flow. It was already clear that this result would allow dynamic changes in blood oxygenation to be measured.

2.5.3 BOLD Haemodynamic Response

Dynamic functional MRI utilising BOLD contrast was first described in humans in 1992 [38, 39]. By applying a stimulus to the subject, whilst serially imaging using fast imaging methods, it was found that it was possible to determine which region of the brain was exhibiting changes in blood flow and metabolism activity. It had been known [55] for sometime that during increased neural activity the average oxygenation of blood in the veins and capillaries increased. This somewhat counterintuitive result is due to

a mismatch between increases in CBF and oxidative metabolism ($CMRO_2$). Fox and Raichle [55] showed that whilst at rest good correlation was found between CBF and $CMRO_2$, this situation differed during dynamic changes. Metabolic changes of 5 % were accompanied by a CBF change of 29 % seemingly suggesting that these parameters may be transiently uncoupled. This mismatch has been described as "*watering the garden for the sake of one thirsty flower*" [56]. In recent years an alternative hypothesis [57], compatible with the results of Fox and Raichle, but which allows CBF and $CMRO_2$ to remain coupled has also emerged, known as the oxygen limitation model [57] (see chapter 5). The coupling of this metabolic response to neural activity has also been shown [58] to be closely coupled.

Early BOLD fMRI experiments utilised block paradigms, whereby stimuli were presented for between 30 s and 1 minute [38, 39] (ON period) followed by a similar length period of rest (OFF period). However with the increasing availability of MRI systems capable of high temporal resolution EPI these stimuli became ever shorter and an era of event related paradigms began. In this regime stimuli are of the order of a few seconds in length [59] or an instantaneous event, such as a button press. This enabled the temporal and spatial characteristics of the BOLD haemodynamic response function (HRF) to be investigated more fully. This only served to underline how little was known about the biophysical mechanisms underlying this method.

The BOLD haemodynamic response can be broken down into three distinct temporal features; the initial dip, the positive overshoot and the post-stimulus undershoot. The early response, or initial dip, is observed during the first 2-3 seconds following stimulus onset. It is manifested as a negative change in signal and is thought to be due to a temporal lag between increased oxidative demand and the corresponding increase in CBF. This would suggest that this process would occur in close proximity to the site of neural activation, most likely in the capillary bed or even the intracellular space. Evidently functional paradigms that utilise this feature should yield higher spatial resolution maps of activation and this has been shown by

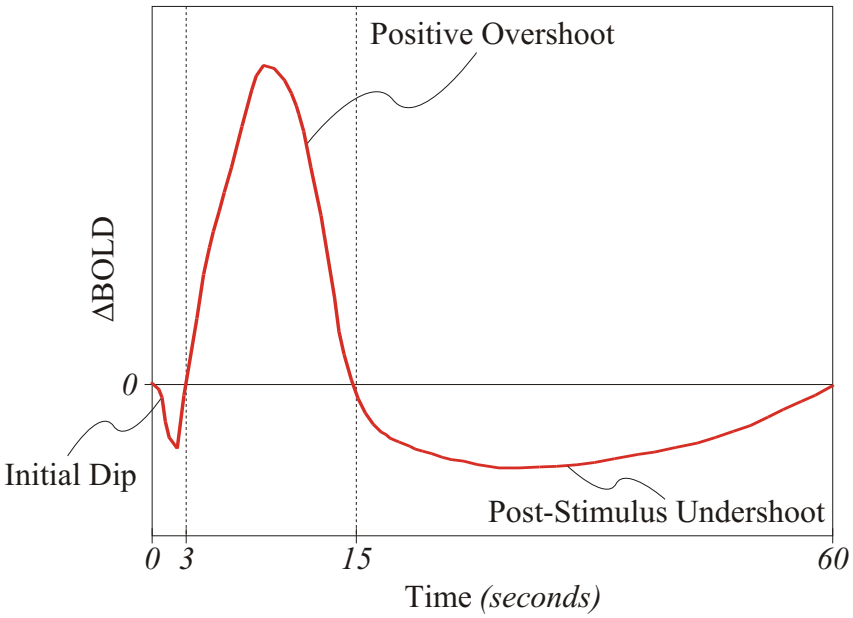

Figure 2.30: Temporal features of the BOLD response.

Yacoub *et al.* [60]. However, although the initial dip has been detected by a select number of groups [61–64], it is particularly difficult to detect routinely as the fractional change in BOLD signal is very small. This often leads to the initial dip being obscured by a combination of instrumental noise, signal drift and physiological noise. Therefore great care must be taken to remove physiological noise [65], reduce subject motion and keep instrumental noise and drift to a minimum.

The main feature of the BOLD response is the positive overshoot. The duration of this feature is dependent on the stimulus duration. As an example, a 5 s visual stimulus produces an overshoot of approximately 15 s duration. This overshoot represents the main haemodynamic response to increased neural activity and is a result of increased CBV and blood oxygenation. Both of these changes are due increases in CBF resulting from relaxation of the arteriole smooth muscle, causing dilation of the blood vessel. Dilation of pericytes that adjoin the vessel have also been shown to

control blood flow [66]. The vessel walls of the capillary bed are thought to be relatively rigid and expand only slightly, if at all, during changes in CBF. Instead changes in CBF are absorbed by expansion of the venule, downstream from the capillary bed. Blood oxygenation decreases along the length of the capillary bed, reaching a new steady state at the venule. Therefore the spatial specificity of this response is not as high as that suggested for the initial dip. Yacoub *et al.* [60] suggest that the limit of this specificity is 2-3 mm, whereas Turner [67] suggests 4 mm. However this response is very robust and can be routinely used to produce maps of functional activity.

The final feature is known as the post-stimulus undershoot. The duration of this feature, given a 5 s visual stimulus, can be anything between 20 s and 40 s, see figure 4.9. It is difficult to accurately determine the duration of the post-stimulus undershoot as it also displays a relatively small fractional change in BOLD signal. However, unlike the initial dip, the increased duration of the undershoot allows this feature to be routinely observed. The physiological origin of the undershoot has not been conclusively proved. The work of Mandeville *et al.* [68] suggested that the post-stimulus undershoot could be explained by the delayed compliance of the venous vasculature. In this scenario the additional blood volume provided by the compliant venule increases the concentration of deoxyhaemoglobin in the imaging voxel. A delay in the relaxation of this venous balloon, relative to the dynamics of CBF change, causes the BOLD signal to undershoot its resting state value. This idea was backed up by observations [69] in rats that showed a transient lag between CBF and CBV dynamics. An alternative to this explanation [70] is that the undershoot could be accounted for by elevated oxidative metabolism post-stimulus, in the absence of increased blood flow. The origin of this elevated metabolism is unknown, at present, but this effect has been observed in fNIRS (functional Near Infra Red Spectroscopy) experiments [71]. The reasons for the absence of a CBF response are similarly unknown. However, it has been suggested [72] that CBF change may be modulated in-directly by neural activity. Elevated metabolism post-stimulus may therefore represent a

separate metabolic process that takes place following intense neural activity.

It is clear that current understanding of BOLD haemodynamics is incomplete. With greater understanding it may be possible to improve the methodology and inference of BOLD fMRI experiments.

2.5.4 fMRI Data Preparation

Detecting the BOLD haemodynamic response in fMRI data is a multi-step process, see figure 2.31. The data is prepared using several pre-processing stages and then subjected to a statistical analysis. The first stage, following acquisition of data on the scanner, is to reconstruct time data into images. Data is acquired in k-space and is Fourier transformed into the image domain. This is an automatic process on the Philips systems, but requires user intervention on the Nottingham 3.0 T system. This process will now be described.

Raw data is transferred from the scanner control workstation, where it is saved as complex time data. In house software [73] is used to Fourier transform this data and perform ghost correction. EPI data is prone to an artefact known as the Nyquist ghost. Sampling of k-space is performed in alternating directions, due to the reversal of the switch gradient polarity. In order to perform a two-dimensional Fourier transform this data must be reversed. Instrumental timing inaccuracies and magnetic field inhomogeneities cause the signal from alternate lines to be modulated. This effect causes a ghost image to be produced in the phase encode direction. This ghost will have a displacement of $N/2$ pixels relative to the real image, where N is the image dimension in pixels. The simplest way to correct this phase shift is by applying a phase angle correction to each point in alternate lines of k-space. This is applied in the frequency encode dimension, which in this example is the $x-$axis.

$$\theta(x) = \theta_0 + x\theta_1 \tag{2.63}$$

The amount of correction required can be determined by eye and is applied to every image in the fMRI data set, assuming the phase error is time inde-

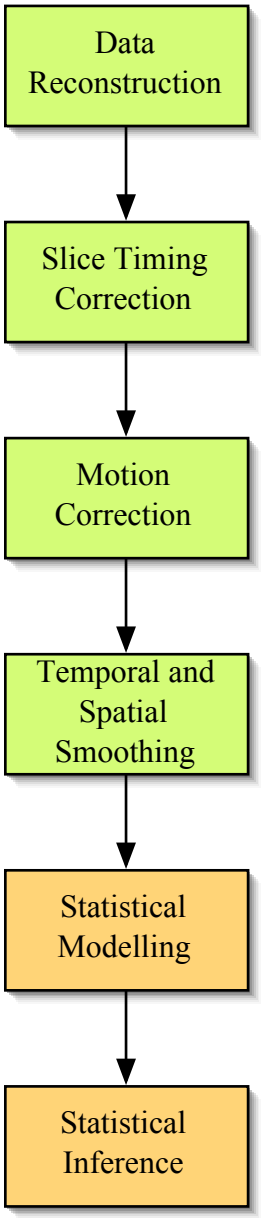

Figure 2.31: The processing steps required to analyse fMRI data. Items coloured green are pre-processing steps and items coloured orange are analysis steps.

pendent. A two dimensional Fast Fourier Transform (FFT) is then applied. Images are saved in the Analyze format [74] as 16-bit signed integers. The dynamic range of this data format ($-32,768 \rightarrow +32,767$) is maximised by using an appropriate scaling factor.

A typical fMRI data set will consist of many slices ($\sim$40) allowing the whole head to be covered. As each slice is acquired discretely, each will have been acquired at a slightly different time with respect to the other slices. This will lead to a phase shift of the BOLD haemodynamic response, across slices, and is of particular importance for event related paradigms. This can be corrected in SPM2 [75] by correcting the phase shift of each slice to the beginning of the volume TR, i.e. the time period in which all of the slices are acquired. In this thesis three slices were acquired in a volume TR of 300 ms, giving a slice TR of 100 ms. The stimulus paradigm was event related and consisted of 5 s of visual stimulation. The resulting haemodynamic response had a duration of approximately 45 s and therefore the phase shift introduced by this slice TR was negligible. Hence slice timing correction was not performed in this thesis.

Functional analyses rely on the change in a single voxel as a function of time, rather than space. Therefore it is important that each voxel represents the same volume of tissue throughout the experiment. This can often be difficult due to subject motion and instrumental drift causing displacement of the brain image within the field of view. In order to reduce the effect of this displacement various motion correction techniques have been developed. In this thesis, SPM2 [75] was used to correct subject motion. In SPM2 registration is performed between a pair of images. The first image is a reference image, conventionally the first image of the data set. The second image is the same imaging slice at another, usually later, time point and is known as the source. The rigid body transformation required to place the source image in the same space as the reference image is then calculated. Motion correction of fMRI data usually uses a $6-$parameter transformation. In translation they consist of the in-plane motion, x and y, and through plane

motion, z. The rotation about these axes are also included and are known as pitch, roll and yaw. For a set of points x_1, x_2, and x_3 of a source image, an affine mapping to points y_1, y_2, and y_3 of the reference image can be defined.

$$\begin{aligned} y_1 &= m_{11}x_1 + m_{12}x_2 + m_{13}x_3 + m_{14} \\ y_2 &= m_{21}x_1 + m_{22}x_2 + m_{23}x_3 + m_{24} \\ y_3 &= m_{31}x_1 + m_{32}x_2 + m_{33}x_3 + m_{34} \end{aligned}$$

SPM2 represents these mappings as a simple matrix multiplication, $\boldsymbol{y} = \boldsymbol{M}\boldsymbol{x}$.

$$\begin{pmatrix} y_1 \\ y_2 \\ y_3 \end{pmatrix} = \begin{pmatrix} m_{11} & m_{12} & m_{13} & m_{14} \\ m_{21} & m_{22} & m_{23} & m_{24} \\ m_{31} & m_{32} & m_{33} & m_{34} \end{pmatrix} \begin{pmatrix} x_1 \\ x_2 \\ x_3 \\ 1 \end{pmatrix}$$

Translation, $\boldsymbol{T}$, and rotation, $\boldsymbol{R}$, matrices can then be used to describe the transformation, $\boldsymbol{M}$, from the source space to the reference space.

$$\boldsymbol{M} = \boldsymbol{T}\boldsymbol{R} \tag{2.64}$$

Optimisation is performed for $6-$parameters using the Newton-Gauss algorithm [76]. The cost function for this optimisation is the mean squared error between the source and reference images. The resulting transformations can then be applied to the source image, and the process repeated for each image in the fMRI data set. These transformations are also inspected and if the subject is found to have moved by greater than one voxel then the dataset is typically discarded.

The data is often smoothed in both the temporal and spatial domains. Temporal smoothing is normally applied by filtering out nuisance frequencies in the pixel time-courses. Filtering out low frequency components of a time-course enables long term drift, due to scanner instability, to be removed. An increase in the SNR can be achieved by removing high frequencies. The selection of threshold frequencies must be chosen carefully, so that the frequencies which describe the haemodynamic response are retained, whilst extraneous

noise is removed. In the context of this thesis temporal smoothing was not performed. Low frequencies were required to examine the baseline signal change as a function of contrast agent concentration. High frequencies were retained in order that small features of the BOLD response were not removed.

Spatial smoothing can be applied by calculating a weighted sum of nearby voxels. This can increase the SNR of the image, but will also reduce the spatial resolution. The Full Width Half Maximum (FWHM) of the smoothing kernel must be selected based on the scale of the expected activated region [73]. For a given FWHM, an activated area greater than this size will see an increase in SNR, however areas smaller than the FWHM will see reduced SNR. Choice of FWHM is, therefore, a compromise and is obviously based on a prior hypothesis. Spatial smoothing is also important when performing group analyses. In group analysis individual subject data is registered to the Montreal Neurological Institute (MNI) template brain, to account for differences in brain morphology between subjects. Images from individual subjects in MNI space are then spatially smoothed and inter-subject comparisons made. Spatial smoothing was not applied to data in this thesis as data were analysed on an individual subject basis and it was important to retain high spatial resolution, and reduce the partial volume effect of averaging several voxels together. The partial volume effect was particularly important in this respect, as the expected volume change temporal dynamics could be drastically altered by contributions from large draining veins.

2.5.5 fMRI Data Analysis

Data analysis was also performed in SPM2 [75] in this thesis. SPM2 uses a General Linear Model (GLM) to detect the haemodynamic response in the fMRI time-series. A model is set up to describe the effect of interest including the timing of the stimulus. Hence a good fit between the model and the time-course data indicates that the data was probably caused by the stimuli. For a single voxel time-course the simplest model is,

$$y = \beta x + \epsilon \tag{2.65}$$

where the data, y, is described by an explanatory variable, x, the correlation of that model, β, and an error term, ϵ. It is likely that there are many variables, n, that can be used to explain the data and the model can be easily expanded to include them.

$$y = \beta_1 x_1 + \beta_2 x_2 + \ldots + \beta_n x_n \tag{2.66}$$

When this approach is extended to all pixel time-courses in an image it is convenient to represent this equation in matrix form.

$$\boldsymbol{Y} = \boldsymbol{X}\boldsymbol{\beta} + \boldsymbol{\epsilon} \tag{2.67}$$

In this case $\boldsymbol{Y}$ represents the time-course data, $\boldsymbol{X}$ are the explanatory models otherwise known as the design matirx, $\boldsymbol{\beta}$ are the correlation coefficients and $\boldsymbol{\epsilon}$ the errors. By fitting this model to the fMRI data it is possible to estimate the model correlation $\hat{\beta} = [\beta_1, \beta_2 \ldots \beta_n]^T$. Equation 2.67 can be re-written in the following way.

$$\boldsymbol{X}^T\boldsymbol{Y} = (\boldsymbol{X}^T\boldsymbol{X})\hat{\beta} \tag{2.68}$$

Hence if $(\boldsymbol{X}^T\boldsymbol{X})$ is invertable,

$$\hat{\beta} = (\boldsymbol{X}^T\boldsymbol{X})^{-1}\boldsymbol{X}^T\boldsymbol{Y} \tag{2.69}$$

This approach is particularly efficient in the case of SPM2 as it is implemented in MATLAB [77], a **mat**rix **lab**oratory. As the errors in the parameter estimates are known, and normally distributed, it is possible to calculate a $T-$statistic,

$$t = \frac{\beta_i}{SE_i} \tag{2.70}$$

where β_i is the ith correlation coefficient of $\hat{\beta}$ and SE_i is the standard error of the estimation of this parameter. If the correlation coefficient is low relative to its standard error, then the fit is not significant, and vice versa. A t-value can then be converted into a z-score or a p-value using the appropriate transformation.

From the estimation of $\hat{\beta}$ it is possible to produce statistical maps, displaying the significance of an explanatory variable at each pixel. To be able

to distinguish which of these pixels is statistically significant and hence determine *true* activations a threshold is applied to the map. The simplest threshold is determined by selecting a level of significance to apply to each pixel of the statistical map. In SPM2 the default uncorrected threshold is set at $p = 0.001$. This represents the probability of a pixel being activated purely by chance, and is obviously very small. However in fMRI, statistical maps generally consist of thousands of pixels. Therefore, despite the very low threshold it is likely that tens of false positives will be detected. This is known as the *multiple comparisons* problem. For example, a set of data consisting of a 64×64 matrix and 40 slices may contains >100,000 pixels inside of the head. An uncorrected threshold of $p = 0.001$ will give 100 false activations. In order to correct this error a Bonferroni correction can be applied. In this case the significance threshold is divided by the number of comparisons, i.e. the number of pixels for which $\hat{\beta}$ was estimated. In the example above this would give $p = 0.001/100,000 = 0.00000001$. Evidently this is overly conservative and it is not used in practice. Gaussian Random Fields (GRF) theory estimates the number of statistically independent pixels. This is lower than the total number of pixels and is due to clustering of significant pixels. GRF reduces the Bonferroni correction by a factor of approximately $2 - 20$ [78] and allows a corrected probability to be displayed, which is typically set at $p = 0.05$.

2.6 Further Reading

In order to gain a greater understanding of the topics covered in this chapter a wide range of reading was undertaken [21, 31, 73, 76, 78–82]. The author would like to acknowledge these works and suggest them as sources for further reading.

Chapter 3

Blood relaxometry

3.1 Introduction

BOLD fMRI techniques use the transverse relaxation properties of blood as a contrast mechanism. The BOLD effect [83] relies on the oxygenation state of haemoglobin, the oxygen carrying molecules within red blood cells. As the blood becomes more deoxygenated its susceptibility, relative to tissue, increases, which in turn reduces T_2 / T_2^* due to increased dephasing of water protons. Changes in metabolism brought about by neuronal activation cause an increase in venous oxygenation decreasing dephasing and increasing T_2 / T_2^*.

The measurement of the dependence of T_2^* on oxygenation and contrast agent concentration has particular relevance to chapter 5. In this chapter the BOLD signal is described as a weighted sum of the intravascular *blood* signal and the extravascular *tissue* signal [47]. These signal components are functions of blood volume change and deoxyhaemoglobin concentration. The extravascular signal is often modelled using the results of numerical simulations [84] or by analytical expressions [85]. However the intravascular signal is generally characterised by empirical results [86]. Measurements of oxygenation dependence have previously been performed at 1.5 T [86]. In order to compare the multi-component model, with experimental data from

chapter 4, measurements of the dependence of R_2^* on both oxygenation and contrast agent concentration at 3.0 T were required.

Alternative fMRI techniques include ASL fMRI, which directly measures CBF changes, and the VASO technique [42], which measures changes in CBV. These techniques rely on the longitudinal relaxation properties of blood. ASL uses a single RF pulse, or train of RF pulses, to modify the longitudinal relaxation of arterial blood proximal to the tissue of interest. After a period of time TI an (tag) image is acquired which elicits longitudinal signal changes in areas where blood is flowing. In typical implementations a second (control) image is acquired without modification of the magnetisation of in-flowing arterial blood. Tag images are then subtracted from control images to yield a perfusion image which is modulated by blood flow changes that occur on activation. As field strength increases the T_1 of arterial blood increases, giving rise to an increase in the perfusion weighted difference signal.

The VASO method assumes that the T_1 of blood is independent of its oxygenation state. Therefore, following an inversion pulse, blood with differing oxygenation will relax to the null point at the same time. This effect allows the blood signal to be nulled whilst leaving the tissue signal to be measured. Decreases in signal indicate increases in blood volume.

It is clear that characterising the relaxation properties of blood is very important. The aim of this study was to measure T_1 and T_2^* of whole human blood. The dependence of these parameters on blood oxygenation, contrast agent concentration and main magnetic field, B_0, was considered.

3.2 Theory

Contrast in MRI is due to variations in the relaxation rates R_1, R_2 and R_2^* for different tissue types. This contrast can be enhanced using a number of agents, and is often achieved by adding small amounts of a paramagnetic transition metal to the sample of interest. The most common clinical exogenous contrast agent is Gadolinium. In its ionic form this metal is toxic,

and it is chelated to form a stable inert complex for use as an *in vivo* contrast agent. Within the human body blood is an endogenous contrast agent. Oxyhaemoglobin is only weakly diamagnetic, whereas deoxyhaemoglobin is paramagnetic. This difference forms the basis of BOLD fMRI.

The mechanisms by which paramagnetic species modify R_1 and R_2 can be described by the Solomon-Bloembergen-Morgan equations [87–89]. In the first instance it will be assumed that the species of interest is Gadolinium, with the specific case of deoxyhaemoglobin discussed subsequently. The relaxation enhancement provided by the introduction of Gadolinium is an additive relaxation rate above the underlying diamagnetic effect.

$$R_i^{obs} = R_i^{dia} + R_i^{para} \qquad i = 1, 2 \tag{3.1}$$

The paramagnetic contribution increases linearly with concentration, where the constant of proportionality, r_i, is known as the relaxivity.

$$R_i^{obs} = R_i^{dia} + r_i[Gd] \qquad i = 1, 2 \tag{3.2}$$

Unpaired electrons, belonging to the Gadolinium ion, cause the local magnetic field to fluctuate rapidly in both magnitude and direction. The interaction of the proton nuclear spins with this field increases the relaxation rate. The origin of this increase in relaxation rate is generally divided into two components. They are the so-called *inner sphere* (IS) and *outer sphere* (OS) interactions.

$$R_i^{para} = R_i^{IS} + R_i^{OS} \qquad i = 1, 2 \tag{3.3}$$

The inner sphere contribution represents the interaction of the Gadolinium electrons and bound water in the first co-ordination sphere of the ion. This effect is transmitted to bulk protons by chemical exchange. Outer sphere effects consist of second sphere interactions and interactions of the Gadolinium ion with bulk protons. Second sphere interactions are caused by water molecules binding to the inner sphere water or the contrast agents protective ligand. Bulk protons experience the rapid translational motion of the Gadolinium ion and experience additional dephasing. The inner and outer sphere components can each be described by the following existing theories.

3.2.1 Inner Sphere Relaxation

Inner sphere proton relaxivity is dependent on exchange of co-ordinated water protons with the bulk. The theoretical results of Luz and Meiboom [90] and Swift and Connick [91] provide the description of inner sphere R_1 and R_2, respectively,

$$R_1^{IS} = \frac{qP_m}{T_{1m} + \tau_m} \tag{3.4}$$

$$R_2^{IS} = \frac{qP_m}{\tau_m} \frac{T_{2m}^{-2} + \tau_m^{-1} T_{2m}^{-1} + \Delta\omega_m^2}{(\tau_m^{-1} + T_{2m}^{-1})^2 + \Delta\omega_m^2} \tag{3.5}$$

where q is the number of bound water molecules per ion, P_m is the mole fraction of bound water molecules, τ_m is the bound water exchange constant, and $\Delta\omega_m$ is the chemical shift difference between bound and bulk water. Bound water protons relax via dipole-dipole (DD) and scalar or contact mechanisms (SC). The longitudinal and transverse relaxation time constants T_{1m} and T_{2m} are therefore a sum of the contributions of these relaxation mechanisms.

$$\frac{1}{T_{im}} = \frac{1}{T_i^{DD}} + \frac{1}{T_i^{SC}} \qquad i = 1, 2 \tag{3.6}$$

However the SC mechanism represents only a small change in relaxation rate, and is therefore neglected in this brief theoretical overview. The dipole-dipole mechanism dominates and the resulting relaxation time constant can be described by the Solomon-Bloembergen-Morgan equations.

$$\frac{1}{T_1^{DD}} = \frac{2}{15} \frac{\gamma_I^2 g_S^2 \mu_B^2}{r^2} S(S+1) \left(\frac{\mu_0}{4\pi}\right)^2 \left[7 \frac{\tau_{c2}}{1 + \omega_S^2 \tau_{c2}^2} + 3 \frac{\tau_{c1}}{1 + \omega_I^2 \tau_{c1}^2}\right] \tag{3.7}$$

$$\frac{1}{T_2^{DD}} = \frac{1}{15} \frac{\gamma_I^2 g_S^2 \mu_B^2}{r^2} S(S+1) \left(\frac{\mu_0}{4\pi}\right)^2 \left[13 \frac{\tau_{c2}}{1 + \omega_S^2 \tau_{c2}^2} + 3 \frac{\tau_{c1}}{1 + \omega_I^2 \tau_{c1}^2} + 4\tau_{c1}\right] \tag{3.8}$$

In equations 3.7 and 3.8, γ_I is the proton gyromagnetic ratio, g_S is the electron spin g factor, μ_B is the proton nuclear magnetic moment, r is the electron spin−proton distance, and ω_S and ω_I are the proton and electron Larmor frequencies, respectively. Both equations are only valid for ions with spin angular momentum quantum number, S, greater than $\frac{1}{2}$. Gadolinium-III is one such ion, with $S = \frac{7}{2}$. The correlation times, τ_{ci}, are a function

of the rotational correlation time of the species, τ_R, the electronic relaxation times, T_{ie}, and the water exchange constant $\tau_m = 1/k_{ex}$, where k_{ex} is the chemical exchange rate.

$$\frac{1}{\tau_{ci}} = \frac{1}{\tau_R} + \frac{1}{T_{ie}} + \frac{1}{\tau_m} \qquad i = 1, 2 \tag{3.9}$$

By substituting the normalised spectral density function (equation 2.29) into these expressions it is possible to determine R_i^{DD} as a function of the spectral density of the water protons, $\mathcal{J}_1$, and Gadolinium electrons, $\mathcal{J}_2$.

$$\frac{1}{T_1^{DD}} = \frac{2}{15}\frac{\gamma_I^2 g_S^2 \mu_B^2}{r^2} S(S+1)\left(\frac{\mu_0}{4\pi}\right)^2 [7\mathcal{J}_2(\omega_S) + 3\mathcal{J}_1(\omega_I)] \tag{3.10}$$

$$\frac{1}{T_2^{DD}} = \frac{1}{15}\frac{\gamma_I^2 g_S^2 \mu_B^2}{r^2} S(S+1)\left(\frac{\mu_0}{4\pi}\right)^2 [13\mathcal{J}_2(\omega_S) + 3\mathcal{J}_1(\omega_I) + 4\tau_{c1}] \tag{3.11}$$

When considering the field dependence of equations 3.10 and 3.11 it is worth noting that τ_R and τ_m are field independent. The electronic relaxation rate τ_{ie} is dependent on field and this is due to the zero field splitting interaction (see references [87–89] for more details). Hence the correlation times τ_{ci} are relatively unchanged with increasing magnetic field and the profile of the spectral density is similarly invariant. However the proton and electron Larmor frequencies are field dependent, and therefore maximum relaxation enhancement will occur when the spectral density maximum coincides with this frequency.

Gadolinium concentration dependence is controlled by variables q and P_m in equations 3.4 and 3.5. All of the currently approved clinical contrast agents have a single co-ordination site, i.e. $q = 1$. Inner sphere proton relaxivity is linearly dependent on q and would appear to be an easy route to higher relaxivity. However the limit of $q = 1$ is imposed by the need for a protective ligand. Ligands that allow more than one water molecule in the inner sphere are less stable and therefore increase the risk of toxic Gadolinium being released. As the number of co-ordination sites cannot be increased, enhanced relaxation can only be achieved by increasing the number of Gadolinium ions i.e. increasing the concentration.

3.2.2 Outer Sphere Relaxation

Further relaxation occurs through two mechanisms; second sphere relaxation and outer sphere relaxation. Second sphere relaxation occurs when water molecules hydrogen bond to the oxygen atom of bound water in the first co-ordination sphere. This interaction can be described by equations 3.4−3.5 and 3.10−3.11. In this case the relevant parameters are usually denoted by a prime, e.g. q', r', etc. However second sphere relaxation theory is still relatively poorly understood. The number of water molecules bound in this way, q', and the distance between the proton and the ion are unknowns. Therefore this component is often neglected.

Outer sphere relaxation is due to translation of the water protons near to the Gadolinium ion. In order to model this effect the water molecules and Gadolinium ions are treated as hard spheres allowing R_1^{OS} and R_2^{OS} to be described.

$$R_1^{OS} = C\,[3j(\omega_I) + 7j(\omega_S)] \tag{3.12}$$

$$R_2^{OS} = C\,[2 + 1.5j(\omega_I) + 6.5j(\omega_S)] \tag{3.13}$$

$$C = \left(\frac{32\pi}{405}\right)\gamma_I^2\gamma_S^2\hbar^2 S(S+1)\frac{N_A[Gd]}{1000aD} \tag{3.14}$$

In equation 3.14, N_A is Avogadro's number, $[Gd]$ is the Gadolinium concentration, a is the distance of closest approach of the water molecule and D is the diffusion constant of the water and Gadolinium solution. The spectral density functions, $j(\omega)$, are non-Lorentzian and mathematically complex. Several definitions can be found in the literature [88, 92, 93].

Again field dependence of R_1^{OS} and R_2^{OS} is due to increasing proton and electron Larmor frequencies versus static spectral density. In this case the spectral density function is dependent on the diffusional correlation time, $\tau_D = a^2/D$. The Gadolinium concentration dependence is linearly related to R_i by the variable $[Gd]$.

3.2.3 Susceptibility Effects

Susceptibility variations within the sample produce an additional contribution to transverse relaxation. The R_2' $(1/T_2')$ component of R_2^* $(1/T_2^*)$ is due to magnetic field inhomogeneities caused by these variations. The local magnetic field is described by equation 2.33 (restated below) and is derived from Curie's law.

$$B_{eff} = B_0(1 + \chi)$$

Curie's law states that the magnetisation of a paramagnetic material will increase linearly with applied magnetic field, B_0. This result was obtained experimentally and shown to be dependent on temperature, Θ, and a constant, C, which is a property of the material.

$$M = C\frac{B_0}{\Theta} \tag{3.15}$$

In a physical sense, this law describes the tendency of atomic magnetic moments to align with a magnetic field, in order to minimise energy. Therefore increasing B will increase M indefinitely. This cannot be the case as once 100 % of the atoms are aligned with the field, further increases in magnetisation are impossible. Once the fraction of aligned atoms becomes large, Curie's law begins to break down. At this point the material is said to be saturated. Equation 2.33 will break from linearity when the magnetic field is large enough to fully align the paramagnetic atoms.

3.2.4 Application to Gadolinium

The effect of a contrast agent as a function of solute concentration and magnetic field can be measured using specialised NMR relaxometry instruments. These systems measure R_1 as a function of magnetic field, or more typically proton Larmor frequency. Plots of this type are known as NMR dispersion (NMRD) profiles. For low molecular weight Gadolinium complexes, it has been shown using this technique [89, 94] that relaxivity reaches a minimum at typical MRI field strengths. A consideration of the Solomon-Bloembergen

equations would suggest that the spectral densities of the nuclear and electron spins are low in magnitude at the Larmor frequencies of these spins. The dependence of R_1 on solute concentration is predicted by equations 3.4 and 3.12. They suggest a linear increase with concentration, which has been confirmed by experiments [95].

The effect of Gadolinium on transverse relaxation R_2^*, is commonly assumed to be linear, as is shown for the R_2 component by equations 3.5 and 3.13. Similarly the susceptibility induced R_2' component would be expected to increase linearly with concentration. The relaxivity variation as a function of field strength is dependent on the saturation of Gadolinium. The work described in this chapter will test whether the Gadolinium atoms are saturated at any point over the range of static magnetic fields used in this work; 1.5 T $\rightarrow$ 7.0 T.

3.2.5 Application to Deoxyhaemoglobin

Red blood cells contain high concentrations of haemoglobin. Haemoglobin contains Fe^{2+} which when oxygenated is in the low spin diamagnetic state (S=0), and when deoxygenated is in the high spin paramagnetic state (S=2). This change of state causes the R_1 and R_2 to be dependent on blood oxygenation. Assuming that red blood cells (RBC) can be approximated by a sphere it is possible to apply the theory from the preceding sections to RBCs.

It is known that haemoglobin does not have co-ordinated water molecules in its inner sphere. This is due to the location of the Fe^{2+} ion deep within the protein structure. The Fe^{2+} is not exposed at the surface. Therefore the inner sphere relaxation mechanisms do not operate for haemoglobin [96]. The majority of the relaxation enhancement is caused by outer sphere effects through equations 3.12 and 3.13. The dependence of R_1 and R_2 on oxygenation is controlled by the concentration term $[Gd]$, where in this case $[Gd]$ is the concentration of deoxyhaemoglobin in the blood. Strictly this is only true for lysed blood as the inhomogenous distribution of susceptibility causes an additional effect [97, 98]. The magnetic field dependence is due to

the interplay between diffusional correlation time, τ_D, and the proton and electron Larmor frequency.

An R_1 NMRD profile of haemoglobin, in either its oxy- or deoxy- states, could not be found in the literature. Koenig *et al.* [94] state that they did not observe a change in R_1 with field strength. In the same work they present an R_2 NMRD profile for deoxyhaemoglobin. This result suggests that increases in R_2 are approximately linear over the range of field strengths used in this chapter (1.5→7.0 T). They also state that outer sphere relaxation effects are enhanced by the containment of haemoglobin in red blood cells. This process would produce the additive R_2' component to form R_2^*. It is difficult to predict the R_2' contribution with field, but following the Gadolinium predictions it could be assumed to be linear.

Additional relaxation due to susceptibility differences within the sample should increase linearly with field strength, as predicted by Curie's law. As with Gadolinium this effect may saturate during the range of field strengths tested, causing Curie's law to breakdown.

3.3 Method

The aim of this work was to measure the relaxation properties of whole human blood, and the variation in these properties with oxygenation, contrast agent concentration and magnetic field strength. As controlled blood sample preparation was crucial to the final result section 3.3.1 describes this process in detail. Relaxation properties were measured using imaging techniques and are described in the subsequent sections.

3.3.1 Blood Preparation

Ethical approval was obtained from the University of Nottingham Medical School Ethics Committee in November 2005. Informed consent was obtained from a single volunteer who donated 100 ml of blood. The subject was asked to abstain from physical exertion before the study, in order to obtain

samples with resting (low) oxygenation. The blood was stored in twenty 5 ml Lithium heparinised blood tubes in order to prevent clotting. Prior to the experiment, samples were stored in a refrigerator at 5°C and used within 48 hours of donation.

Blood oxygenation was modulated by slowly bubbling oxygen through the sample, in a fume cupboard. The gas flow rate was maintained at a low level [99] in order to prevent the viscous blood from foaming. Using this technique it was possible to obtain a range of blood oxygen saturation, Y, values between 0.48 and 0.84. This range represents the normal physiological range for venous oxygenation. An oxygenation approaching 1 would be expected in arterial vessels.

In order to investigate the blood relaxation dependence on contrast agent concentration small amounts of ProHance [100] were added to samples. Blood sample tubes were sealed wherever possible to prevent changes in blood oxygenation from occurring. Other than exposure to atmospheric oxygen, the oxygenation of these samples was not altered, and as such represented a resting level of oxygenation. The samples used in this experiment had a mean oxygen saturation of $Y = 0.66 \pm 0.05$ and a mean haematocrit of $HCT = 0.43 \pm 0.02$. The contrast agent was diluted from its initial concentration of 0.5 M to 50 mM by adding 1 ml of ProHance to 9 ml of distilled water. A micropipette was used to measure these volumes. In order to control for differing volumes of blood in each heparinised blood tube the mass of blood in each tube was measured. Additional blood tubes were weighed and the blood contained within the storage tube transferred to them. A repeat measurement of their combined weight was then made. A small volume of diluted ProHance was added to the samples in the range 25 μl to 250 μl, with the intention of covering a blood contrast agent concentration range of 0.3 mM to 3 mM. One final weight measurement, of the combined bottle, blood and contrast agent, allowed an accurate calculation of the blood contrast agent concentration to be made.

The oxygenation and haematocrit of the blood samples was repeatedly

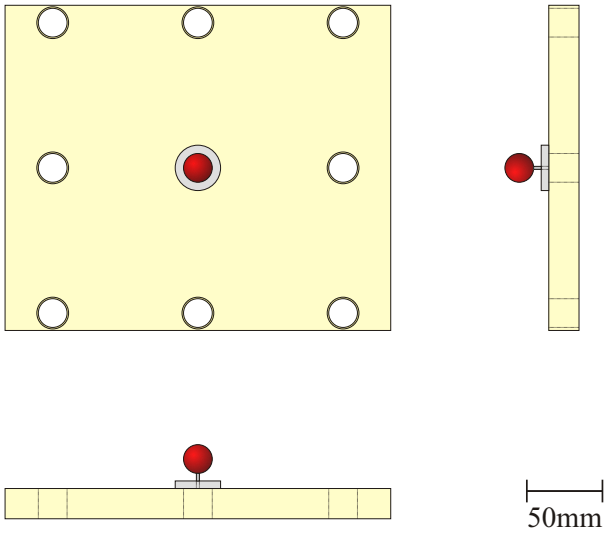

Figure 3.1: Blood sample holder: Various sample locations can be chosen, enabling imaging of several samples simultaneously.

measured throughout the preparation stage using a Radiometer ABL710 Blood Gas Analyser [101]. Prepared samples were transferred to spherical containers with an external diameter of 19 mm. Each sphere was sealed by a 2 mm diameter plastic screw. This enabled removal of the blood sample, post-experiment, in order to measure blood oxygenation and haematocrit. A spherical geometry was chosen to minimise the susceptibility artefact associated with the sample-air boundary. A custom sample holder was used during experiments, see figure 3.1. It allowed the samples to be suspended above the surface of the holder thereby retaining the geometrical advantages of a sphere. Throughout this preparation phase the blood samples were stored in an electrically heated water bath at 37 °C in order to replicate *in vivo* conditions.

3.3.2 Imaging

Imaging was performed on Philips Achieva whole body scanners at magnetic field strengths of 1.5 T, 3.0 T and 7.0 T. A sample holder was used to place the blood samples at the centre of a quadrature head coil, which was used for transmission and reception. Samples were not heated or stirred whilst within the scanner. However prior to the experiment they were heated to 37°C and agitated to ensure complete mixing of the blood components. Due to the short scan durations ($<\sim$ 100 s) of the pulse sequences used in this experiment it was decided that cooling and settling of the blood would not have a deleterious effect on the results. The details of the pulse sequences used in the measurement of T_1 and T_2^* are described below.

T_1 Measurement

The T_1 measurement technique consisted of an Inversion Recovery sequence, with EPI image acquisition (IR-EPI). The preparation pulse was a 180° hyperbolic secant pulse followed by a crusher gradient to destroy residual transverse magnetisation. This was then followed by a set of 10 inversion delay (TI) times tailored to the field strength at which the experiment was performed. A further set of inversion times was selected for the experiments on samples containing contrast agent, and were used across all field strengths. These inversion times are summarised in table 3.1. Following the inversion delay a 90° RF pulse was applied and 19 lines of k-space acquired using a GE EPI switched gradient with blipped phase encoding. Due to the small sample size it was possible to acquire a 64 × 19 imaging matrix. This reduced the scan duration, and TE, as a complete image could be acquired following each inversion pulse in a single shot. The shortest TE was selected as 4.7 ms. An in-plane resolution of 1 mm × 1 mm was acquired, with a slice thickness of 3.3 mm. A repetition time, TR, of 10 s was used for the oxygenation samples. It was possible to use a shorter TR of 6 s for the contrast agent samples, due to the much reduced T_1. The total scan durations at these TR values were 101 s and 60.5 s, respectively.

1.5 T	3.0 T	7.0 T	Gd
100 ms	150 ms	200 ms	50 ms
250 ms	350 ms	400 ms	100 ms
400 ms	550 ms	800 ms	200 ms
600 ms	800 ms	1100 ms	300 ms
800 ms	1100 ms	1400 ms	400 ms
1100 ms	1500 ms	1900 ms	500 ms
1500 ms	2000 ms	2600 ms	600 ms
2000 ms	2700 ms	3200 ms	700 ms
3000 ms	4000 ms	4500 ms	900 ms
5000 ms	6000 ms	7000 ms	1150 ms

Table 3.1: Inversion times for T_1 mapping across field strengths. The final column lists the inversion times used at all field strengths for measurement of T_1 in the samples containing contrast agent.

T_2^* Measurement

The T_2^* measurement sequence utilised a single RF excitation pulse followed by an EPI switched gradient and acquisition module. However unlike a conventional EPI module the phase encoding blips were removed and replaced by an initial phase encode gradient. The phase encoding gradient was then stepped between repeats of the sequence [102]. This approach causes the same phase encoding to be applied to all of the gradient recalled echoes of each sequence block, allowing the acquisition of many closely spaced echoes for each line of k-space. These individual lines were recombined to produce 63 images with a matrix size of 128×128. The spacing of the echo times, ΔTE, was determined by the EPI switching frequency employed at each field strength. Hence ΔTE was 1.39 ms, 1.12 ms and 1.16 ms at 1.5 T, 3.0 T and 7.0 T, respectively. The slightly larger echo spacing at 1.5 T was due to lower specification gradient hardware. This did not effect the measurement of T_2^* due to the comparatively slow relaxation rate at this field strength. A field of view of 128 mm was chosen giving an in-plane resolution of 1 mm

$\times$ 1 mm with a 3.3 mm slice thickness. This was identical to the resolution used for the T_1 relaxation measurements. A TR of 267 ms was used giving a total scan duration of 35.2 s.

3.3.3 Analysis

Data analysis was performed in MATLAB [77] using custom written code. Transverse relaxation was measured by fitting a linear function to log intensity data versus echo time on a pixel by pixel basis.

$$\log S = -TE\ R_2^* + \log S_0 \tag{3.16}$$

The matrix inversion technique was used to perform this fit, in which weighting was applied to earlier high intensity echoes. An intensity threshold, of 3$\times$ the background noise, was applied to each of the echoes. This was particularly important at 7.0 T as the transverse signal decayed to zero within 30 echoes ($\sim 35\ ms$).

Mapping R_2^* at high and ultra-high field magnetic fields is a challenge. Macroscopic susceptibility changes, in this case at the sphere-air boundary, cause enhanced signal decay. This leads to an artificially enhanced measurement of R_2^*. It has been shown [102] that a linear magnetic field gradient along the z-axis causes additional signal decay with a sinc profile. This sinc component perturbs the general monoexponential decay of the sample causing an error in the calculation of R_2^*. In order to avoid pixels with large sinc components from biasing the overall result, the significance of each point was assessed by calculating the χ^2 value. These values were converted to p-values, to remove the bias due to varying numbers of echoes included in the fit. Regions of interest were then created by thresholding these maps, and the mean and standard error calculated. The only major susceptibility distortions were caused by small air bubbles at the top of the spheres.

Longitudinal relaxation was measured by fitting a non-linear function to the data using least squares fitting. Equation 2.36, reproduced below, was

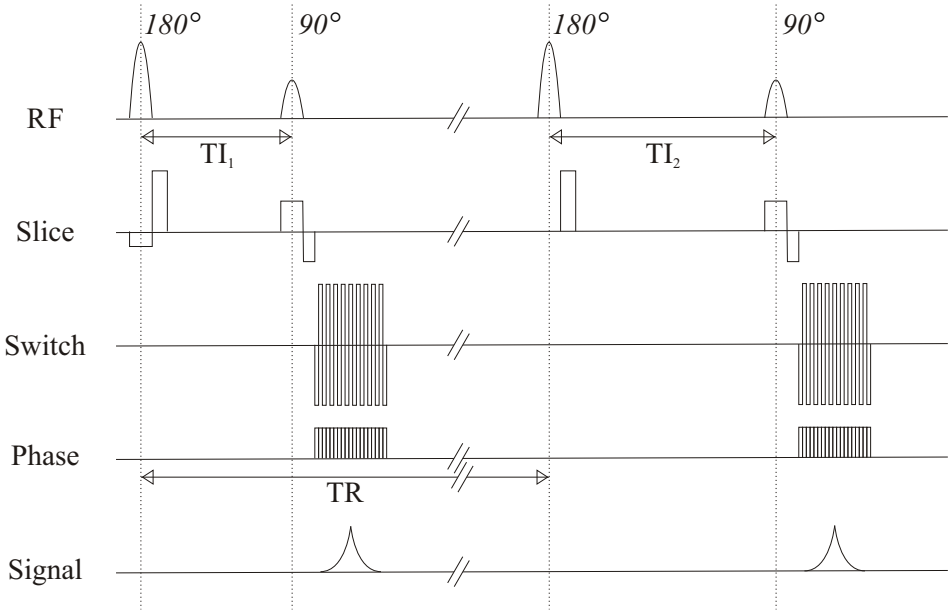

Figure 3.2: Inversion recovery pulse sequence with EPI image readout.

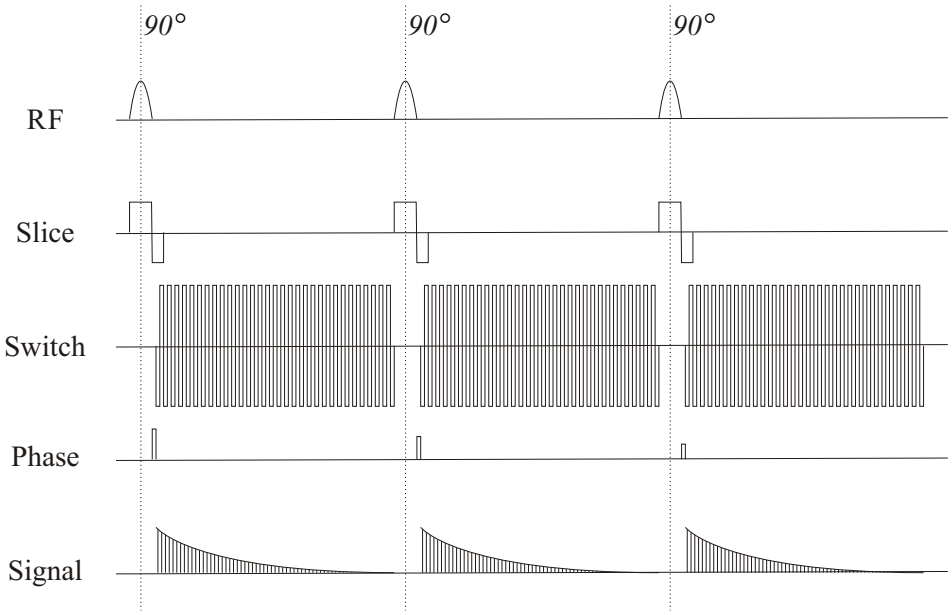

Figure 3.3: Rapid gradient echo pulse sequence.

used to model the data.

$$M_z = M_0(1 + (\cos\theta - 1)e^{-TI\,R_1}) \tag{3.17}$$

The angle θ was included in the fit to model imperfect inversion of the spin system. The shortest attainable echo time (TE=4.7 ms) was used for all TIs. Susceptibility induced distortion was therefore reduced to a minimum and region of interest selection by significance was not required. The region of interest was selected by thresholding an intensity image to create a mask. The mean and standard error of these time-courses could then be calculated.

3.4 Results

The results of this study can be separated into three sections. The following sections consider the changes in the relaxation times T_1 and T_2^* as a function of oxygenation, contrast agent concentration and main magnetic field strength. In each case these parameters are plotted as the relaxation rates R_1 and R_2^* which are equivalent to the reciprocal of the relaxation times T_1 and T_2^*, respectively.

3.4.1 Oxygenation

Figure 3.4 plots the longitudinal relaxation rate, R_1, as a function of deoxyhaemoglobin content, $1 - Y$. Each sample data point is plotted as the mean and the error bars represent the standard error. Due to the relatively large number of pixels in the maps of R_1 the standard error is rather small. However this neglects the errors introduced during production of the samples which probably accounts for the dispersion from the line of best fit. These errors consist of differences in oxygenation and haematocrit, as well as the amount of heparin dissolved in the sample and damage caused to the red blood cells during handling and storage. The best fit to this data has a linear form and represents the longitudinal relaxivity of whole blood as a function

B_0/T	r_1^{dHb} / ms^{-1}	r_1^{Gd} / $ms^{-1}mM^{-1}$
1.5	$(-5.2 \pm 7.6) \times 10^{-5}$	$(3.6 \pm 0.5) \times 10^{-3}$
3.0	$(4.1 \pm 8.9) \times 10^{-5}$	$(2.9 \pm 0.5) \times 10^{-3}$
7.0	$(7.6 \pm 2.9) \times 10^{-5}$	$(3.4 \pm 0.4) \times 10^{-3}$

Table 3.2: Longitudinal relaxivity of whole blood as a function of deoxyhaemoglobin content and contrast agent concentration.

B_0/T	$r_2^{*\,dHb}$ / ms^{-1}	$r_2^{*\,Gd}$ / $ms^{-1}mM^{-1}$
1.5	$(5.4 \pm 1.1) \times 10^{-2}$	$(1.5 \pm 0.2) \times 10^{-2}$
3.0	$(16.9 \pm 2.2) \times 10^{-2}$	$(3.7 \pm 0.5) \times 10^{-2}$
7.0	$(34.7 \pm 4.7) \times 10^{-2}$	$(8.2 \pm 2.3) \times 10^{-2}$

Table 3.3: Transverse relaxivity of whole blood as a function of deoxyhaemoglobin content and contrast agent concentration.

of deoxyhaemoglobin content, r_1^{dHb}, the values of which are summarised in table 3.2.

Figure 3.5 plots the transverse relaxation rate, R_2^*, against deoxyhaemoglobin content, $1 - Y$. The errors in the plotted data points are quite small. As noted above these errors do not take into account the variability introduced during sample preparation. Li *et al.* [86] have previously shown that for physiologically plausible values of Y these variables display a linear relationship. Hence the solid lines represent linear fits to the data from each field strength. The gradients of these lines represent the transverse relaxivity of whole blood as a function of deoxyhaemoglobin content, $r_2^{*\,dHb}$, and are summarised in table 3.3. These values were then used to model the change in R_2^* during activation.

3.4.2 Contrast Agent

Figure 3.6 plots R_1 as a function of contrast agent concentration. As suggested by NMRD data, the effect of the contrast agent on R_1 does not depend on magnetic field, for the range of fields tested. From a theoretical stand-

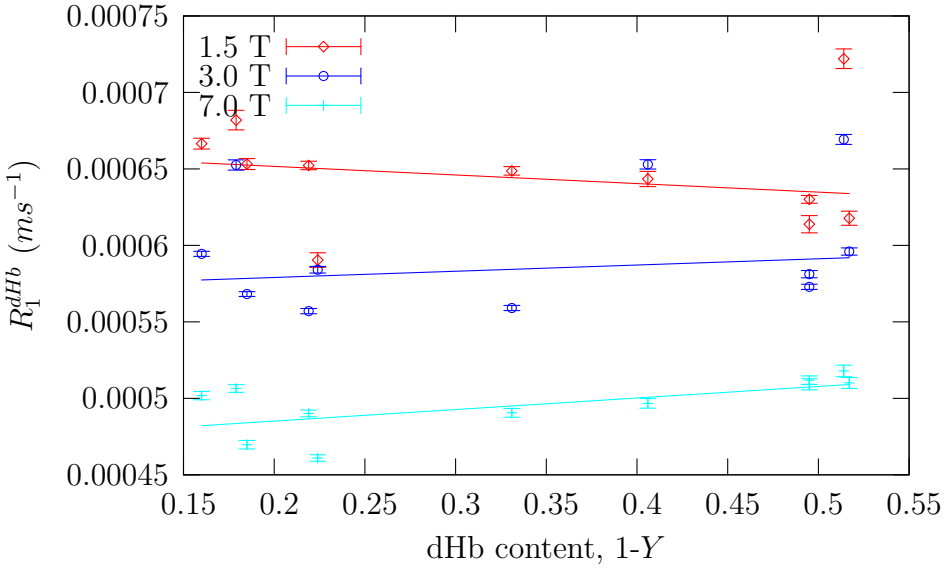

Figure 3.4: Longitudinal relaxation rate, R_1, of human blood plotted as a function of deoxyhaemoglobin content.

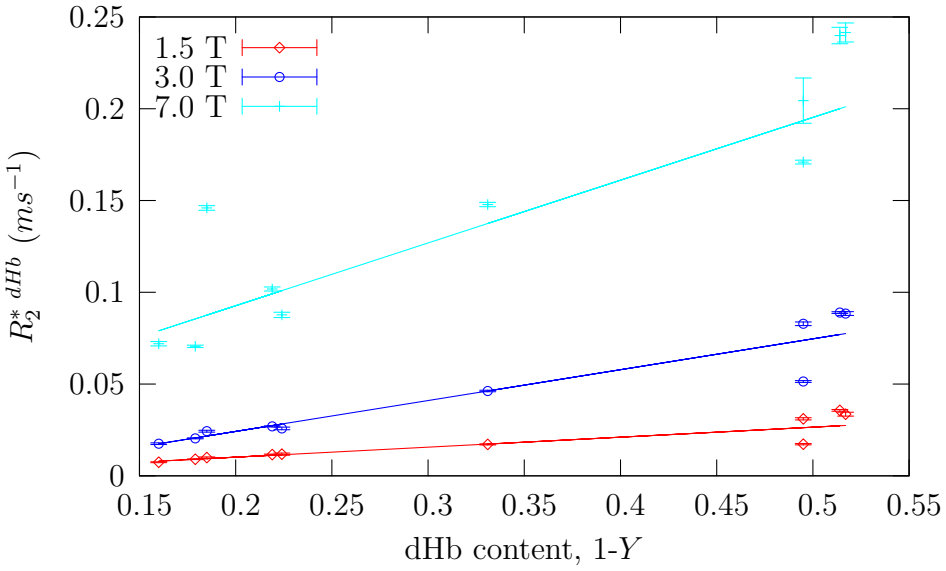

Figure 3.5: Transverse relaxation rate, R_2^*, of human blood plotted as a function of deoxyhaemoglobin content.

point this would suggest that at these field strengths the electron and proton Larmor frequencies do not occur at the same frequencies as the peak of the spectral density function. This is manifested by the tight grouping of the data points across field strengths. A linear fit to this data, at each field strength, yields the contrast agent relaxivity in whole blood, r_1^{Gd}. These values are summarised in table 3.2.

Figure 3.7 plots R_2^* versus contrast agent concentration. The relationship between these quantities is typically thought to be linear. However this result was not observed. The data in figure 3.7 display a parabolic form. An explanation for this result was sought and Monte Carlo simulations were performed to confirm the parabolic nature. The hypothetical origin of this effect is discussed in more detail in section 3.5. Due to this effect, relaxivity, $r_2^{*\ Gd}$, was measured by fitting a linear function to the positive slope region, beyond the null point. These values are summarised in table 3.3, allowing a cross field relaxivity comparison to be performed.

3.4.3 Magnetic Field

Figure 3.8 shows the relationship between longitudinal relaxivity, r_1^{dHb}, and magnetic field strength, B_0. The error in this data is the error in gradient of the curve fit performed to calculate r_1. Despite this relatively large error the data appears to suggest that deoxyhaemoglobin relaxivity increases approximately linearly with magnetic field strength. As was noted in section 3.2 it was not possible to find a NMRD profile in the literature for deoxyhaemoglobin. Work performed on Gadolinium chelates shows that at high field the T_1 shortening effect is expected to reach a maximum. This is not the case for deoxyhaemoglobin and obviously requires further research. Figure 3.9 plots the effect of B_0 on r_1^{Gd}. As expected the relaxivity appears to have reached a maximum in the range 1.5 T to 7.0 T.

Figure 3.10 plots transverse relaxivity, $r_2^{*\ dHb}$, as a function of magnetic field strength. The relationship between $r_2^{*\ dHb}$ and field is approximately linear, but appears to depart slightly from linearity at ultra-high field. Fig-

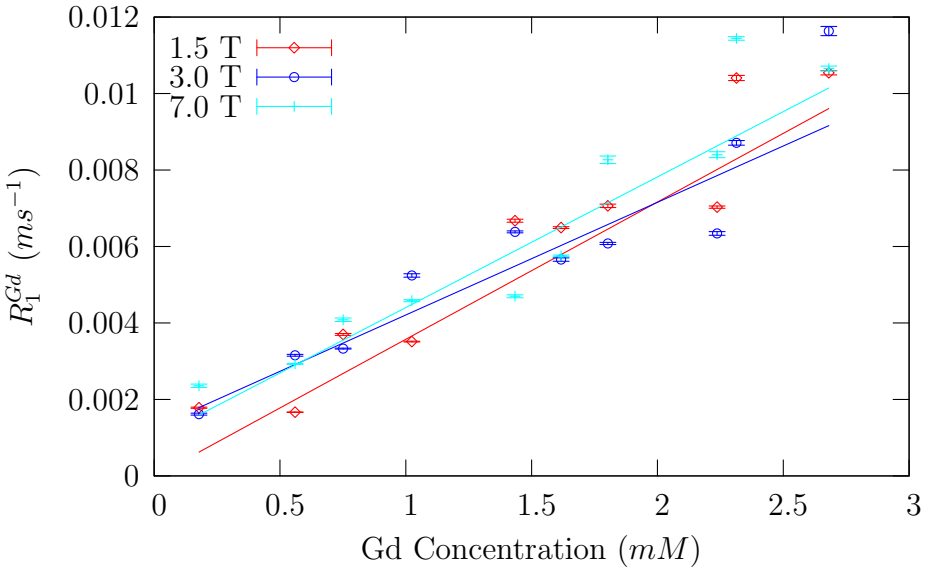

Figure 3.6: Longitudinal relaxation rate, R_1, of human blood plotted as a function of Gadolinium concentration in mM.

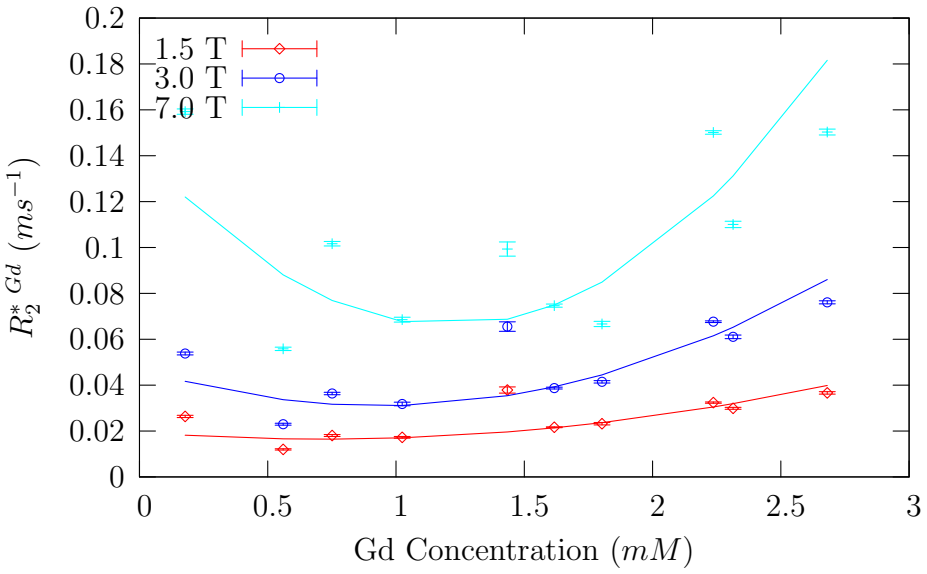

Figure 3.7: Transverse relaxation rate, R_2^*, of human blood plotted as a function of Gadolinium concentration in mM.

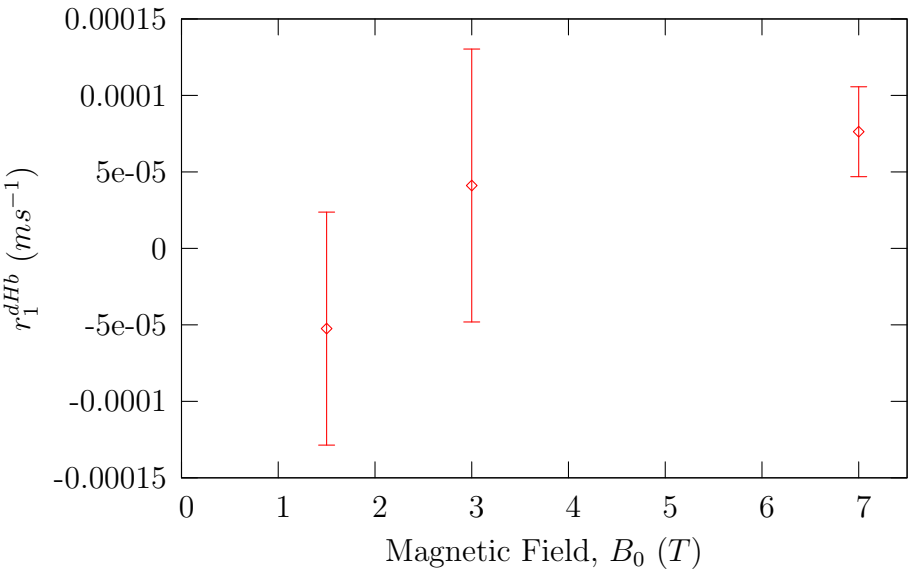

Figure 3.8: Longitudinal deoxyhaemoglobin relaxivity, r_1^{dHb}, plotted as a function of main magnetic field strength, B_0.

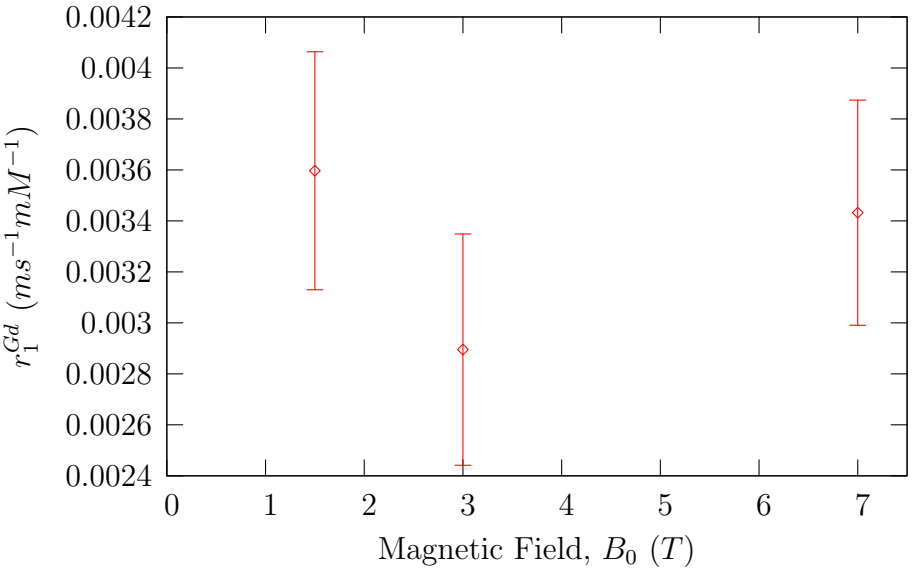

Figure 3.9: Longitudinal Gadolinium relaxivity, r_1^{Gd}, plotted as a function of main magnetic field strength, B_0.

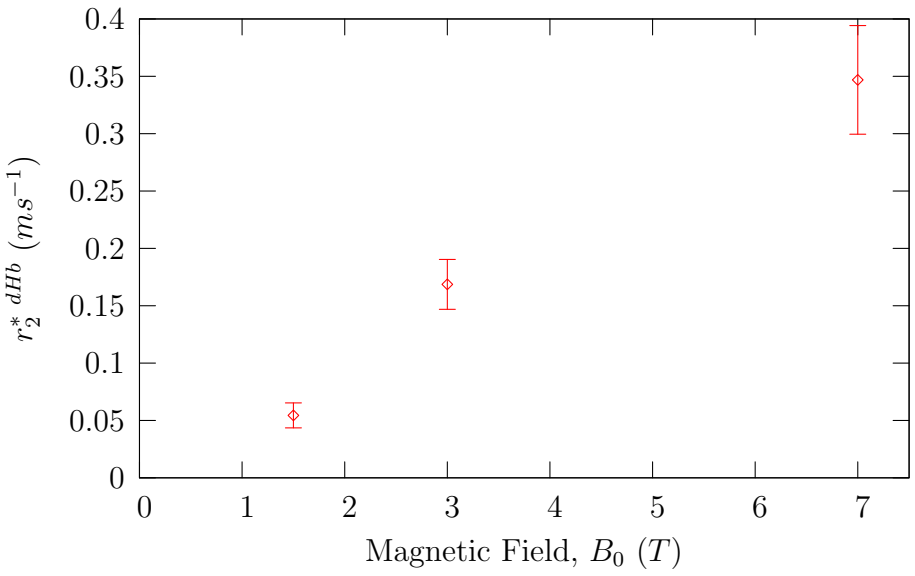

Figure 3.10: Transverse deoxyhaemoglobin relaxivity, $r_2^{*\,dHb}$, plotted as a function of main magnetic field strength, B_0.

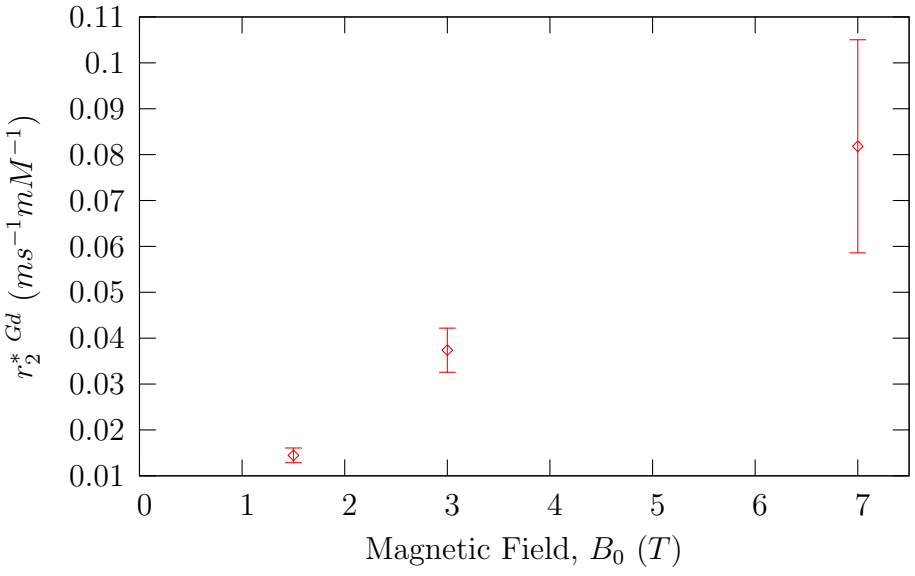

Figure 3.11: Transverse Gadolinium relaxivity, $r_2^{*\,Gd}$, plotted as a function of main magnetic field strength, B_0.

ure 3.11 shows a linear relationship between $r_2^{*\ Gd}$ and magnetic field strength. In both cases this linearity suggests that susceptibility effects are still contributing in a linear manner. Hence Curie's law may still hold.

3.5 Simulation

As a consequence of the anomalous result recorded in the contrast agent experiments (figure 3.7) a description of the theoretical mechanism was sought. It is suggested that the origin of this effect is the inhomogeneous distribution of paramagnetic species in the blood. In terms of magnetic properties, whole blood can be separated into two main components. Red blood cells account for between 38 % and 54 % of blood volume. These cells incorporate molecules of haemoglobin which contain iron. The magnetic state of these molecules is dependent on their oxygenation. Oxygenated haemoglobin, or oxyhaemoglobin, is diamagnetic and deoxygenated haemoglobin, or deoxyhaemoglobin, is paramagnetic. Diamagnetic plasma makes up the majority of the remaining blood volume, as white blood cells and platelets make up less than 0.5 %. Microscopic magnetic field gradients are set up between paramagnetic deoxyhaemoglobin containing red blood cells and diamagnetic plasma. Water protons diffusing through these gradients are dephased, increasing the relaxation rate R_2^*. Contrast agents such as ProHance dissolve in blood plasma. They cannot cross the intact blood brain barrier or pass through the plasma membrane of red blood cells. Therefore the contrast agent acts to increase the susceptibility of the plasma, reducing the susceptibility difference between the red blood cells and the plasma. This results in a reduction in the magnitude of the microscopic field gradients, reducing dephasing and reducing R_2^*. When the susceptibility of the plasma matches that of the deoxyhaemoglobin, magnetic field gradients are neutralised and an R_2^* minimum is observed. Increases in contrast agent concentration beyond this point reverse the polarity of the microscopic magnetic field gradients and the dephasing effects return. In order to investigate this hypothesis further

a model of intravascular susceptibility was developed and combined with a Monte Carlo simulation to simulate R_2^*.

3.5.1 Susceptibility Model

A model of the susceptibility differences present in blood was produced in order to test the hypothesis in the preceding section. In this context the R_2^* null-point represents the point where the susceptibility difference, $\Delta\chi$, between red blood cells and plasma is zero. For this to be the case, the susceptibilities of the various diamagnetic and paramagnetic components of blood would have to be delicately balanced. The components present in the model are deoxyhaemoglobin, χ_{dHb}, oxyhaemoglobin, χ_{Hb}, plasma, χ_{plasma}, and contrast agent, χ_{CA}. These components represent the major components of blood. The overall susceptibility is a sum of these components weighted by several factors. The red blood cell compartment is weighted by the haematocrit (HCT), with the plasma space making up the remainder. In the case of haemoglobin, the susceptibility is dependent on the oxygenation state of the cells. It is assumed that each red blood cell has the same oxygenation state, i.e. the oxygen saturation, Y, in each cell is equal.

$$\Delta\chi = HCT\{(1-Y)\chi_{\mathrm{dHb}} + Y\chi_{\mathrm{HbO}}\} - (1-HCT)\{\chi_{\mathrm{plasma}} + \chi_{\mathrm{CA}}[\mathrm{CA}]\} \quad (3.18)$$

Measurements of the susceptibility components were taken from the work of Spees *et al.* [103]. In this work SQUID magnetometry was used to measure all four components, using pure water as a reference standard. The experimentally measured Y and HCT values of 0.66 ± 0.05 and 0.43 ± 0.02, respectively, were used. In common with the experiment the contrast agent concentration was varied between 0 mM to 3 mM. The resulting susceptibility difference ranged from $+2.39 \times 10^{-8}$ to -4.42×10^{-8} (cgs). Figure 3.12 plots the absolute value of $\Delta\chi$ versus contrast agent concentration. The R_2^* null-point of figure 3.7 falls within the range of the susceptibility model null-point.

Component	Variable	χ (SI)	$\Delta\chi^b$ (cgs)
Deoxyhaemoglobin	χ_{dHb}	-0.483 ppm	$+1.814 \times 10^{-7}$
Oxyhaemeoglobin	χ_{HbO}	-0.749 ppm	-0.275×10^{-7}
Plasma	χ_{plasma}	-0.714 ppm	0
Gadolinium	χ_{Gd}	$+11.55$ ppm^a	$+0.193 \times 10^{-7}\ mM^{-1}$

Table 3.4: The components of the blood susceptibility model and their respective susceptibility values [103]. All values are dimensionless unless otherwise stated. ^{a}Volume susceptibility of a 0.5 M Gadolinium based contrast agent Omniscan. $^b\Delta\chi$ calculated relative to plasma.

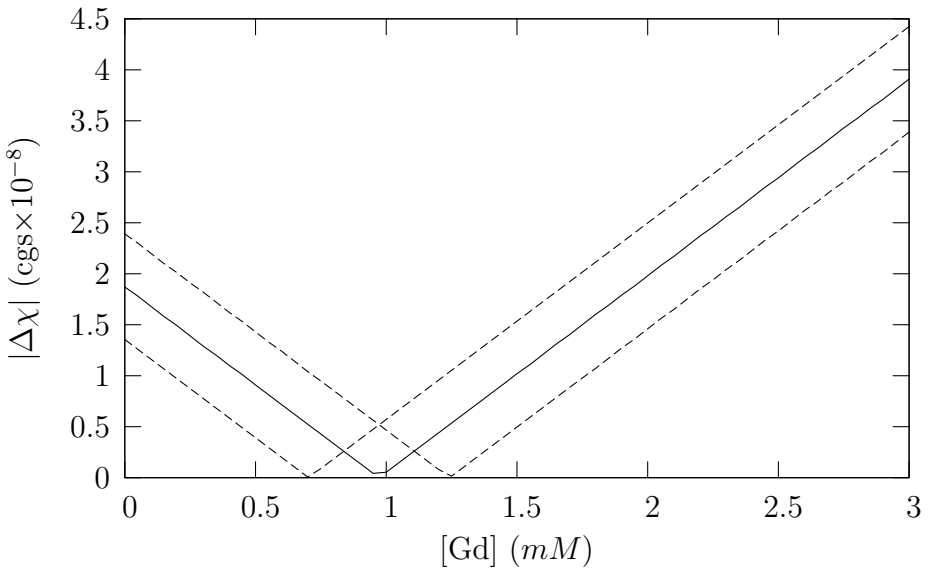

Figure 3.12: Blood susceptibility model as a function of contrast agent concentration, from 0 to 3 mM. The solid line represents the effect of the mean oxygenation and haematocrit ($Y = 0.66, HCT = 0.43$). Dashed lines reflect the maximum range of the oxygenation and haematocrit standard errors, i.e. $(Y = 0.62, HCT = 0.45) \rightarrow (Y = 0.71, HCT = 0.41)$.

3.5.2 Monte Carlo Simulation

Monte Carlo simulations followed the method of Weisskoff *et al.* [104]. The MR signal was calculated from the expectation value of the proton phase.

$$S = \langle e^{i\phi} \rangle \tag{3.19}$$

The expectation value was calculated over both the starting position of the proton and the random path taken due to diffusion. Therefore this expectation can be separated into two parts.

$$S(t) = \frac{1}{V} \underbrace{\int_v d\boldsymbol{x}}_{\text{Starting Position}} \underbrace{\int d\phi p(\phi, t; \boldsymbol{x}) e^{i\phi}}_{\text{Random Path}} \tag{3.20}$$

Here $p(\phi, t; \boldsymbol{x})$ represents the probability of a proton, starting at position $\boldsymbol{x}$, acquiring a phase ϕ in time t. In the method of Weisskoff *et al.* the integrals of equation 3.20 are combined to produce,

$$S(t) = \frac{1}{N} \sum_{n=1}^{N} e^{i\phi_n(t)} \tag{3.21}$$

where N represents the total number of proton random walks and $\phi_n(t)$ is the accumulated phase of the n^{th} proton at time t. Monte Carlo estimation is used to calculate the expectation value over different starting positions and the stochastic random walk of the protons.

For the purposes of this simulation it is assumed that red blood cells can be described as spheres with a radius R. It is also assumed that the vast majority of measured signal is derived from water protons diffusing through plasma. Free water within the red blood cells is severely constrained and subject to large field perturbations in deoxygenated cells. Therefore only extracellular protons were simulated and red blood cells were considered to be impermeable. The simulation consisted of a loop of the following 4 steps;

1. Randomly distribute M red blood cells throughout space to give a volume fraction equal to the blood haematocrit (HCT $= V_{\text{spheres}}/V_{\text{total}}$). Set the susceptibility difference between the red blood cells and plasma to a nominal value, i.e. 1×10^{-7}. Place a single proton at the centre of the system.

2. For every time step, Δt, displace the proton by a random amount in the x, y and z dimensions. Estimate displacement by using a normally distributed random number generator with mean 0 and standard deviation $\sqrt{2D\Delta t}$, where D is the diffusion coefficient.

3. Evaluate the magnetic field at this new location by summing over the field contributions for all perturbers.

4. Evaluate the accumulated phase by trapezoidal integration, $\Delta\phi = \gamma B \Delta t$.

For each proton, steps 2-4 were repeated, recording the evolution of phase, $\Delta\phi$, in 5 ms steps. Steps 1-4 were repeated for a proton count, N, of 10,000. Phase increments were stored for 5 ms blocks. This allowed the simulation of both Hahn spin echo and gradient echo pulse sequences. For a spin echo sequence the phase of a given TE was calculated by inverting the phase value beyond TE/2 prior to summation e.g. $\Phi_{20}^{SE} = \phi_5 + \phi_{10} - \phi_{15} - \phi_{20}$. Similarly for a gradient echo measurement the phase at a given TE is the sum of the preceding phase measurements e.g. $\Phi_{20}^{GE} = \phi_5 + \phi_{10} + \phi_{15} + \phi_{20}$. The signal was then estimated using equation 3.21. A simulated R_2^* value can then be calculated by fitting a mono-exponential decay to this data.

The slowest stage of the simulation was the random distribution of red blood cells (step 1). In the work of Weisskoff *et al.* the volume fraction of particles was chosen to be 0.02. However in order to simulate a realistic haematocrit (HCT) the volume fraction must be between 0.30 and 0.50. A cube with sides of 100 μm and HCT=0.40 requires the placement of almost 1500 spheres, with a radius of 4 μm. Initial experiments showed that for HCT$\leq$0.40 placement of red blood cells using the following method was feasible;

1. Generate the x, y and z co-ordinates of the red blood cell centre using a uniformly distributed random number generator.

2. Check that the distance between this newly generated red blood cell and existing red blood cells is greater than $2R$. If this distance is less than $2R$, discard new co-ordinates and return to step 1.

Steps 1 and 2 were repeated M times to produce M randomly distributed spheres. However for HCT>0.40 this method was unfeasible due to the less

than optimal packing of the spheres. In order to simulate a physiological range of HCT values a different distribution method was required. This new method shares some of its attributes of the simulated annealing technique described in chapter 5. All M red blood cells are initially generated with disregard for overlapping of adjacent spheres. Overlaps are then removed by randomly perturbing one red blood cell and testing whether it improves the minimum spacing between that sphere and the remaining spheres. In more detail this method processes through the following steps;

1. Generate the x, y and z co-ordinates of M red blood cell centres using a uniformly distributed random number generator.

2. Randomly select one red blood cell using a uniformly distributed random number generator. Calculate the minimum distance between this sphere and the other $M-1$ spheres.

3. Perturb the co-ordinates of this sphere in the x, y and z dimensions by adding a small value generated by a normally distributed random number generator.

4. Re-calculate the minimum distance between this sphere and the other $M-1$ spheres. If the minimum distance is increased then retain this new configuration, otherwise discard this solution.

These steps were repeated until no overlaps between adjacent spheres exist. Unlike the first distribution method this algorithm allows higher HCT values of between 40 % and 50 % to be achieved.

The field perturbation resulting from each spherical particle [104] has the following form,

$$\frac{\Delta B_z(r,\theta)}{B_0} = \frac{4\pi}{3}\Delta\chi\left(\frac{R}{r}\right)^3(3\cos^2\theta - 1) \tag{3.22}$$

where r and θ are the usual spherical co-ordinates and R is the radius of the particle. In order to simulate R_2^* as a function of field strength and susceptibility only a single simulation is required for each HCT and R value.

The magnetic field, ΔB_z^{tot}, at the protons current location is a sum of the contributions from each of the red blood cells.

$$\Delta B_z^{tot}(r_i, \theta_i) = \frac{4\pi}{3}\Delta\chi B_0 \sum_{i=1}^{M} \left(\frac{R}{r_i}\right)^3 (3\cos^2\theta_i - 1) \tag{3.23}$$

Hence the total magnetic field, $B = B_0 + \Delta B_z^{tot}$,

$$\Delta\phi = \gamma B_0 \Delta t + \gamma \Delta B_z^{tot} \Delta t \tag{3.24}$$

and therefore $\Delta\phi$ is a sum of a constant magnetic field component and a time-dependent component, which differs for each proton due to the different random paths they follow. The additional phase shift due to the main magnetic field, $\gamma B_0 \Delta t$, can be neglected during the Monte Carlo simulation and its effect added in post-processing. Similarly the nominal susceptibility, added in step 2 of the Monte Carlo simulation, can be divided out and any value multiplied in. Equation 3.24 reduces simulation time greatly and allows a much larger range of susceptibility values, and all three field strengths, to be simulated. Susceptibility values were calculated using equation 3.18.

3.5.3 Method

Following optimisation of the Monte Carlo simulation parameters (see below), the effect of varying haematocrit and sphere radius on the simulated value of R_2^* could then be determined. Male haematocrit values vary between 0.40 and 0.54 (mean 0.47), whilst females have a range of 0.38 to 0.46 (mean 0.42) [46]. For the purposes of simulation a haematocrit range between 0.30 and 0.50, in steps of 0.05 was chosen. The dependence of R_2^* on sphere radius was also investigated due to the significant difference in shape between a sphere and the biconcave disc form of a red blood cell. The average radius of a human red blood cell is $\sim$4 μm. Hence a range of R values were chosen between 3 μm and 5 μm, in steps of 0.5 μm. Simulations were performed on a 10 node HPC cluster. Each node consisted of two dual-core AMD Opteron 2.0 GHz processors and 8 Gb of RAM. Jobs were submitted in batches of 250

protons to a Sun Grid Engine queuing system, allowing 10,000 protons to be simulated simultaneously by utilising the entire cluster. With an average utilisation of 90 %, these simulations were performed over the course of two weeks.

These results were used to select an appropriate sphere radius and haematocrit. It was difficult to select a sphere radius that would adequately approximate a biconcave disc. It has previously been shown that the magnetic field distribution of a biconcave disc is very different to that of a sphere [105]. Hence a sphere radius was chosen such that its volume matched that of an average red blood cell. Using the measurements described by Gilles *et al.* [105] the volume of an average red blood cell was calculated. It was found that an equivalent sphere would have a radius of $\sim$3 μm. The haematocrit was chosen to approximate that measured in the preceding experiments as $HCT = 0.40$.

Optimisation

The simulated space was chosen to be a 100 μm $\times$ 100 μm $\times$ 100 μm cube. The diffusion coefficient, D, of the protons was set at 1.3 $\mu m^2 ms^{-1}$ [104] to represent diffusion in blood plasma. Therefore the maximum displacement of the proton following the maximum TE of 80 ms is 14.4 μm. A large maximum displacement may cause the protons to experience *edge effects*, whereby the contribution from distant particles is reduced due to the absence of spheres beyond the simulated universe dimensions. In practice the maximum displacement of the proton with respect to the universe centre will be much smaller. The high density of impermeable spheres used in this experiment reduces the mobility of the protons, reducing the chances of them travelling in a straight line for 80 ms.

Echo times between 5 ms and 80 ms were recorded, in steps of 5 ms. Each 5 ms echo time was further subdivided into smaller steps, allowing the proton to more accurately sample the magnetic field gradients. In order to investigate the optimum step size for this operation a number of step sizes

were evaluated, see table 3.5. A set of 50,000 red blood cell distributions were produced and reused for each step size. By simulating a large number of protons the accuracy of the result could be improved, and by reusing the same red blood cell distributions the time burden of this accuracy could be reduced. By summing the resulting phase measurements in blocks of 10,000 it was possible to calculate 5 separate *measurements* of R_2^*. This allowed a calculation of the standard error in these results to be determined from the standard deviation of this data. Table 3.5 summarises the step sizes evaluated and the mean and standard error of the R_2^* measurements. Figure 3.13 plots the R_2^* value versus the step size, given a sphere radius of 4 μm and $\Delta\chi = 1 \times 10^{-6}$. The value of R_2^* appears to plateau beyond 0.003125 ms, equivalent to 1600 steps per TE. Selecting the appropriate step size is a compromise between accuracy and computational speed, therefore an experiment was performed to assess the duration of a single proton simulation. This included the distribution of the red blood cells as well as the random walk of the proton. A comparison was made between the simulations perceived to be the fastest and slowest, which consisted of HCT values of 0.30 and 0.50, respectively, with a sphere radius of 4 μm. Ten protons were simulated for each step size and the mean and standard error of the simulation duration calculated. These results are plotted in figure 3.14 and show that the distribution of the red blood cells dominates the simulation duration. It was also important to determine how many protons had to be simulated in order to produce an accurate result. Using the data from the step size investigation (HCT=0.40) it was possible to calculate R_2^* and the error in this value for proton counts varying between 1,000 and 50,000. In this investigation ten simulated measurements were performed and the mean and standard error plotted in figure 3.15.

From these investigations a step size of 0.00078125 ms was chosen. The position of this step size on the plateau of figure 3.13 suggests that it is adequately sampling the magnetic field gradients of the spherical perturbers. As shown by figure 3.14 this does not add significantly to the overall processing

time. A proton count of 10,000 was chosen with reference to figure 3.15. This value was the minimum requirement to ensure acceptable results.

3.5.4 Results

The results of the Monte Carlo simulation provide an interesting insight into the intravascular component of the MR signal. The manifestations of this component will only be visible when imaging the macrovasculature. Figure 3.16 shows the relationship between haematocrit and R_2^* for a nominal susceptibility, $\Delta\chi = 1 \times 10^{-7}$. This result shows that this dependency is relatively weak. There is only a 15 % reduction in R_2^* for a 60 % reduction in haematocrit. Hence the value of R_2^* is only slightly effected by the density of the particles present. This is not the case at lower packing fractions (data not shown), as $R_2^* \to 0$ when $HCT \to 0$

Figure 3.17 considers R_2^* as a function of sphere radius. A much larger effect is observed here. A reduction in sphere radius by 60 % yields a decrease in R_2^* of 60 %. A plateau in R_2^* is not observed until the sphere radius surpasses 30 μm (data not shown). Hence the choice of sphere radius is very important. However a sphere is only a first approximation of a biconcave disc, as was previously noted. It is difficult to predict the effect of a more realistic field pattern, although it is likely that R_2^* would increase due to steeper and less spatially smooth magnetic field gradients.

By substituting the susceptibility model values (from equation 3.18) into a Monte Carlo simulation with $HCT = 0.4$ and $R = 3$ μm it was possible to calculate the effect of a contrast agent. Susceptibility values were calculated assuming a blood oxygen saturation of $Y = 0.633$ and a contrast agent concentration between 0.1 mM and 3 mM. This gave a susceptibility range of $+1.87 \times 10^{-8}$ cgs to -3.91×10^{-8} cgs. Figure 3.18 plots this dependence at field strengths of 1.5 T, 3.0 T and 7.0 T. The error bars represent the standard error calculated from 10 simulations of R_2^*. Of note is the prediction of a quadratic dependence of R_2^* on contrast agent concentrations. This function was used to empirically model the experimental data in figure 3.7,

Step Size (ms)	Number of Steps	$R_2^* \times 10^{-3}$	
		Mean	S.E.
0.2	25	7.16	0.05
0.1	50	7.24	0.03
0.05	100	7.35	0.07
0.025	200	7.39	0.01
0.0125	400	7.49	0.04
0.00625	800	7.59	0.08
0.003125	1600	7.72	0.05
0.0015625	3200	7.74	0.06
0.00078125	6400	7.72	0.05

Table 3.5: Step size range investigated during the optimisation of the Monte Carlo simulation.

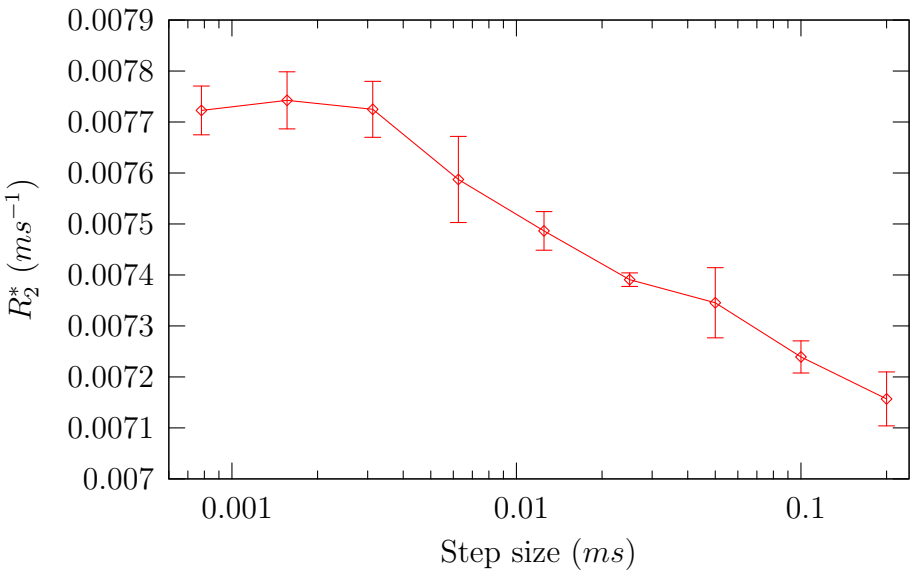

Figure 3.13: The effect of step size on calculated R_2^*. A plateau is observed at small step values. Sphere radius $R = 4$ μm, $\Delta\chi = 1 \times 10^{-6}$.

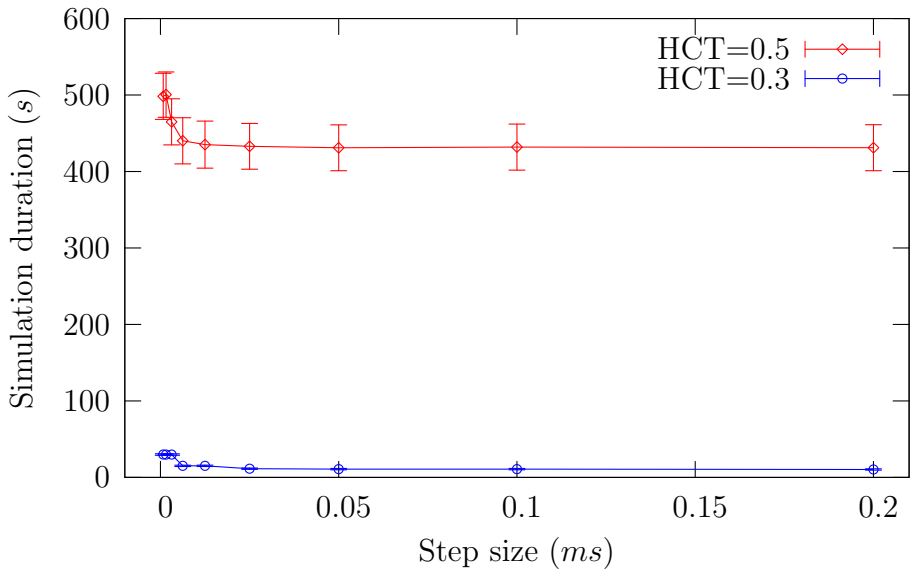

Figure 3.14: The effect of different step sizes on the time required to simulate a single proton. Sphere radius $R = 4$ μm, $\Delta\chi = 1 \times 10^{-6}$.

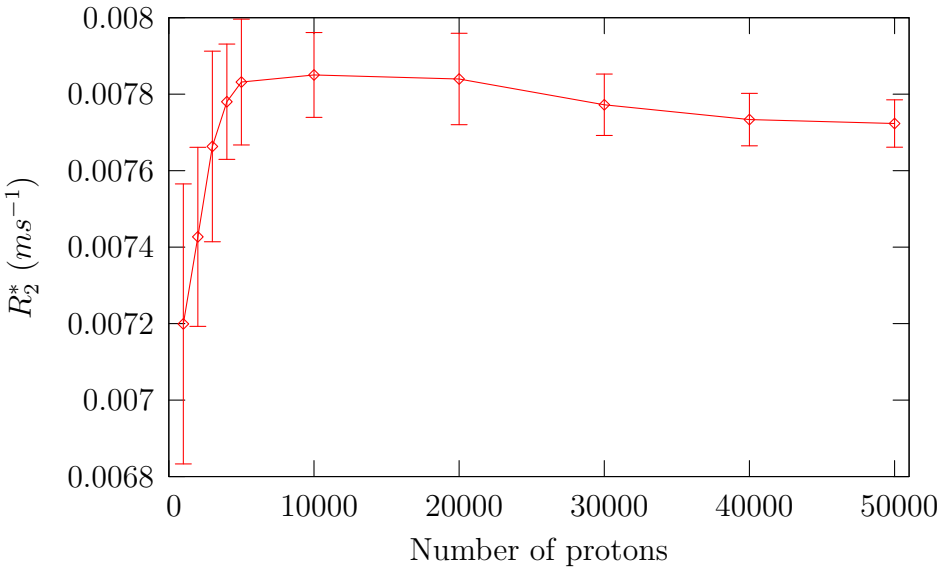

Figure 3.15: The effect of total proton count on the measured value, and error, of R_2^*. Sphere radius $R = 4$ μm, $\Delta\chi = 1 \times 10^{-6}$.

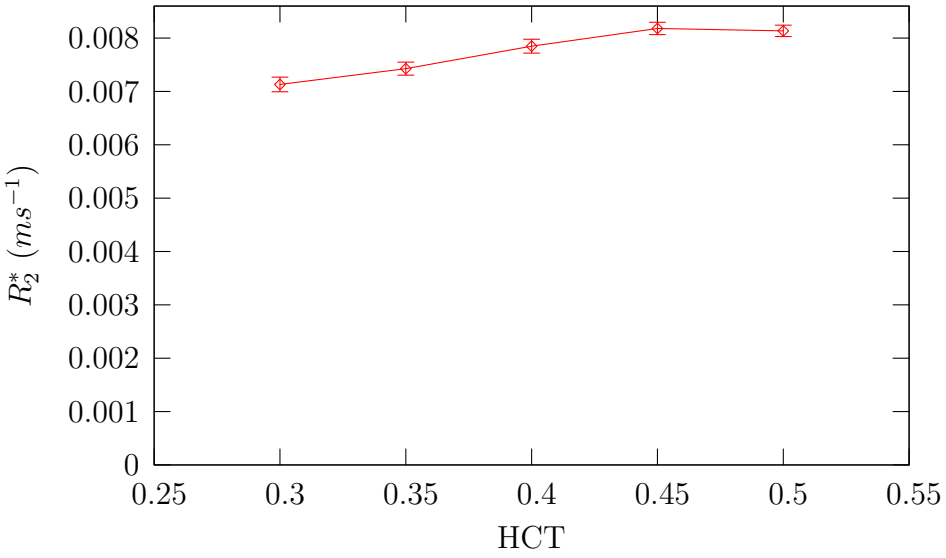

Figure 3.16: The relationship between R_2^* and blood haematocrit. Sphere radius $R = 4$ μm, $\Delta\chi = 1 \times 10^{-6}$.

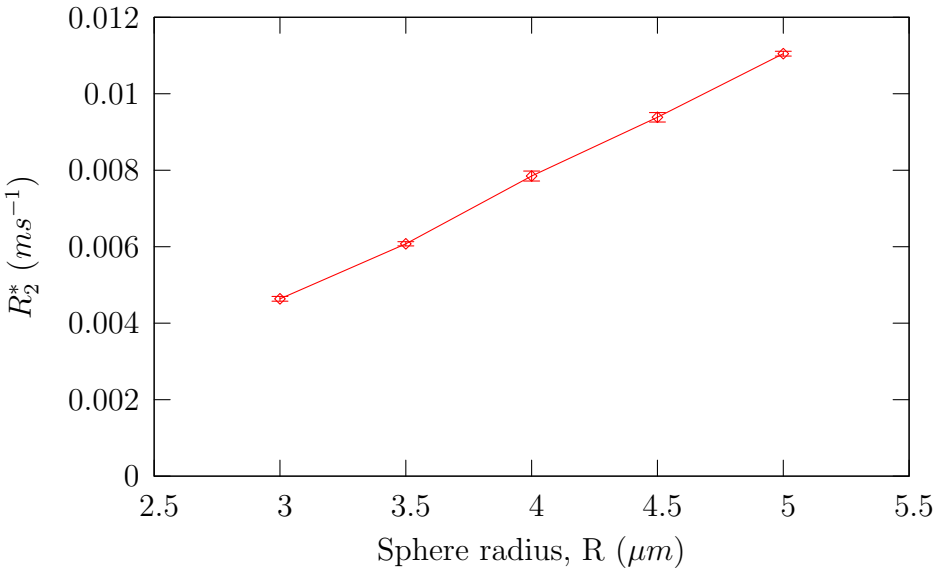

Figure 3.17: The relationship between R_2^* and sphere radius. $\Delta\chi = 1 \times 10^{-6}$.

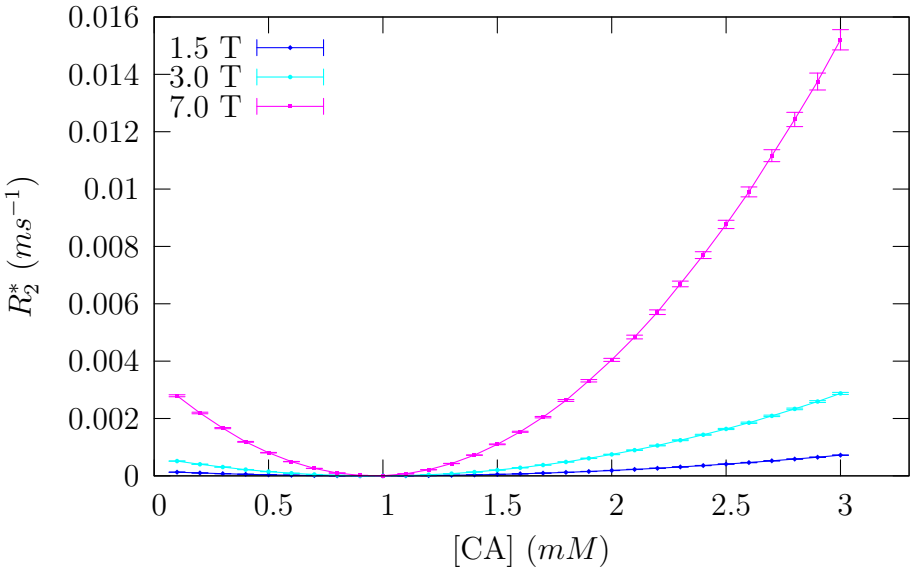

Figure 3.18: The effect of contrast agent on R_2^* as simulated using Monte Carlo methods. Error bars represent the standard error in the simulation of R_2^*. Susceptibility values calculated using equation 3.18. Sphere radius $R = 3$ μm, $Y = 0.663$, $HCT = 0.4$.

by performing a least squares fit.

Discrepancies between the simulated and experimental results are likely to be due to deficiencies in the model. As noted above, one of the largest sources of error is the approximation of red blood cell geometry to a sphere. It is also assumed that all of the signal is extracellular, i.e. due to protons in the plasma diffusing through magnetic field gradients. The spherical red blood cells are considered to be impenetrable. This means that intracellular signal is completely neglected and that exchange into, and out of, this space is not possible. If protons were allowed to diffuse within impenetrable spheres the signal contribution is likely to be negligible. However if these protons were allowed to exchange, with the bulk, an increase in the relaxation rate might be observed. In addition the model does not simulate dipole-dipole relaxation, giving rise to $R_2^* = 0$ at $\Delta\chi = 0$.

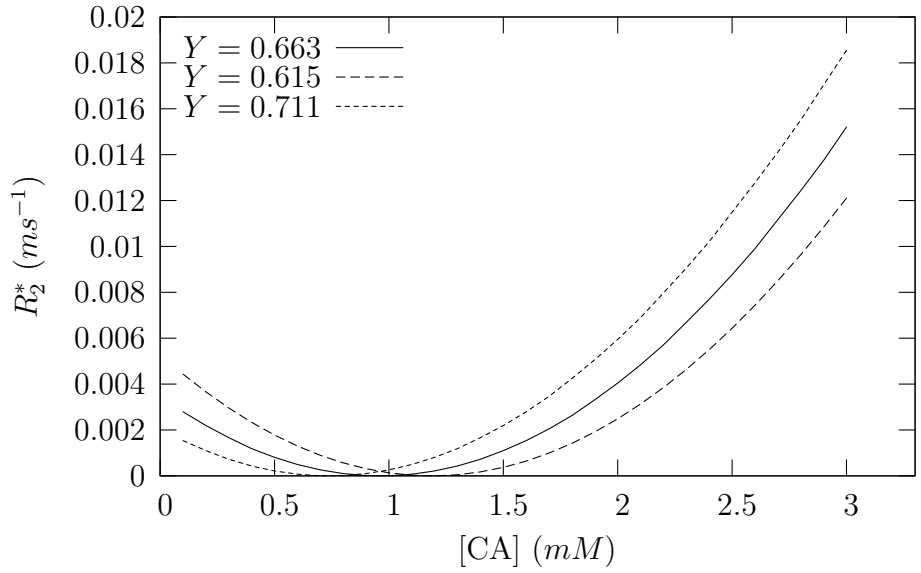

Figure 3.19: Range of 7.0 T simulation result given error in the measurement of blood oxygenation. The solid and dashed lines represent the mean and standard error range of Y, respectively. Susceptibility values calculated using equation 3.18. Sphere radius $R = 3$ μm, $Y = 0.615 \rightarrow 0.711$, $HCT = 0.4$.

Finally the expected range of the R_2^* curve was estimated based on the measured range of blood oxygenations. The susceptibility was re-calculated assuming a fixed haematocrit but with a variation of Y equal to the range of the standard error in the measurement of the blood oxygenation ($Y = 0.61 \rightarrow 0.71$). Figure 3.19 was calculated for a magnetic field of 7.0 T and clearly shows the sensitivity of this result to blood oxygen saturation.

3.6 Discussion

In this study the R_1 and R_2^* of whole human blood has been measured using imaging techniques. This was achieved using small samples of blood and high resolution imaging techniques at three different field strengths. These values were then used to calculate the R_1 and R_2^* relaxivities of deoxyhaemoglobin

and contrast agent in blood. A measurement of contrast agent relaxivity, $r_2^{*\,Gd}$, and deoxyhaemoglobin relaxivity, $r_2^{*\,dHb}$ was of particular importance to the modelling work of chapter 5 where the BOLD signal is split into intra- and extravascular compartments. Whereas the extravascular compartment is well modelled theoretically [85], the intravascular compartment has traditionally been described by empirical results [106].

It was found that R_1 of blood is dependent on oxygenation for field strengths greater than 1.5 T. The deoxyhaemoglobin relaxivity, r_1^{dhb}, increases with field strength, but appears to plateau for ultra high field clinical MRI systems. Within the errors of this experiment the dependence of R_1 on contrast agent concentration is independent of field strength, as is r_1^{Gd}. This is as predicted by NMRD measurements [89, 94].

Measurements of R_2^* show a linear dependence on oxygenation, as would be expected for the narrow range of oxygenation values measured [86]. The deoxyhaemoglobin relaxivity, $r_2^{*\,dHb}$, increases linearly as a function of magnetic field strength. It was expected that R_2^* as a function of contrast agent concentration would follow a similar trend. However what was observed was a quadratic dependence, with a minimum which was dependent on the oxygenation of the blood. Data points preceding the minimum therefore represented a negative relaxivity. This effect has previously been observed [107] in *in vivo* relaxivity measurements of guinea pig kidneys. In this thesis it was hypothesised that this effect was due to microscopic field gradients within the blood formed by the inhomogenous distribution of susceptibility. The minimum would then be due to a nulling of these magnetic field gradients. A similar hypothesis was later found in the work of Mulkern *et al.* [108]. They performed a similar experiment using dairy cream and a contrast agent, yielding similar results. In this case they hypothesised that the inhomogenous distribution of susceptibility was caused by lipid droplets in the cream.

Monte Carlo simulations were performed to test the magnetic field gradient hypothesis. The results of this simulation predicted a quadratic dependence of R_2^* on contrast agent concentration. They also offered an insight into

the factors affecting the intravascular MR signal. The dependence of R_2^* on haematocrit was shown to be weak. This is consistent with the experimental work of others [99]. These results also showed the weakness of the simplified blood cell geometry chosen, as R_2^* was strongly dependent on sphere radius. In addition the minimum was found to be very sensitive to oxygenation, as was demonstrated by figure 3.19.

In future work the application of this technique to measuring blood oxygenation will be investigated. It is hoped this will allow measurements to be performed clinically *in vivo*. This would be particularly useful, for example, in the treatment of cancer. The blood oxygenation in the vessels surrounding tumours is useful in diagnosing cancer types and treatment methods. However there are obstacles to overcome. The maximum licensed contrast agent dose is a 0.3 mM kg^{-1}. A rapid infusion of this amount would only give a plasma concentration of 1.4 mM. A concentration range between 0 and 3 mM is required to give a large enough dynamic range to measure the full range of Y values. It may be possible to gain a larger susceptibility range by using USPIO contrast agents. This could be tested through the use of the Monte Carlo technique described here. There are many improvements that could be made to the Monte Carlo simulation. In the first instance this technique could be extended to the use of realistic red blood cell shaped perturbers. It would also be interesting to model the dipole-dipole contribution to relaxation. Processing such models would require a substantial increase in computational power. Fortunately the University has invested in a 1000 node AMD Opteron cluster, which would allow such a simulation to be performed.

Chapter 4

Cerebral Blood Volume Change During Neural Activation

4.1 Introduction

The aim of this study was to investigate the time-course of cerebral blood volume (CBV) change following a short visual stimulus. This was achieved by measuring the change in R_2^* on activation during an infusion of a paramagnetic contrast agent (ProHance [100]). Previous work [95] at the SPMMRC produced measurements of the fractional change in CBV during a 12 s block stimulus paradigm with a 2 s temporal resolution. This work was itself preceded by similar animal [109] and human [110] studies involving SPIO contrast agents.

To further improve understanding of the BOLD effect this work [95] has been extended to a temporal resolution of 300 ms and an event related stimulus paradigm. A 16 minute triple dose of contrast agent was infused whilst multi-echo EPI images were acquired. Neuronal activation of the visual cortex was stimulated through the use of red LED goggles flashing at a frequency of 8Hz. This chapter describes the theory and methodology used to measure fractional CBV change in human visual cortex.

4.2 Theory

The aim of this section is to introduce the underlying theory behind the methods used later in this chapter. Section 4.2.1 describes how it is theoretically possible to measure the total blood volume change of the cerebral vasculature during focal neural activation. This requires the use of an exogenous contrast agent, the use of which requires certain precautions to be undertaken. Section 4.2.2 describes the potential risks and details additional exclusion criteria used during subject selection. Finally the theoretical pharacokinetics of the contrast agent used in this study (ProHance) are described in section 4.2.3.

4.2.1 Fractional Cerebral Blood Volume Change

Assuming, as Kennan *et al.* [109] suggest, that the transverse relaxation rate, R_2^*, is a function of the susceptibility difference, χ, between blood and tissue and the tissue blood volume, V, then:

$$R_2^* = \kappa V \chi + c \tag{4.1}$$

where κ is a proportionality constant dependent on vascular geometry and c is a constant dependent upon field homogeneity, other sources of dephasing and T_2. Recent research [111] suggests that CBV change during neuronal activation occurs not only in venous vessels, but also in the arterial vasculature, and therefore equation 4.1 can be reformulated to reflect this.

$$R_2^* = \kappa_v V_v \chi_v + \kappa_a V_a \chi_a + c \tag{4.2}$$

The cerebral vasculature is modelled as two compartments; arterial and venous. In equation 4.2, κ_v and κ_a represent the effect of tissue morphology on local field perturbations, V_v and V_a represent venous and arterial blood volume, and χ_v and χ_a the susceptibility difference between venous and arterial blood, respectively, and the surrounding tissue.

During neural activation BOLD contrast occurs due to a change in local CBV, ΔV, and blood susceptibilty, $\Delta\chi$. Susceptibility change is brought

about by increased venous oxygenation, which reduces the amount of paramagnetic deoxyhaemoglobin in the blood. By performing a two-dimensional Taylor expansion the following equation is produced.

$$\begin{aligned} \Delta R_2^{*\ act} &= \kappa_v(\Delta V_v\chi_v + V_v\Delta\chi_v + \Delta V_v\Delta\chi_v) \\ &\quad +\kappa_a(\Delta V_a\chi_a + V_a\Delta\chi_a + \Delta V_a\Delta\chi_a) \end{aligned} \tag{4.3}$$

It is assumed that arterial blood is nearly fully oxygenated ($\chi_a = 0$), that its oxygenation will not change during activation ($\Delta\chi_a = 0$) and that all contrast is endogenous (i.e. due to increased venous oxygenation). Therefore $\Delta R_2^{*\ act}$ will be determined by the negative $\Delta\chi_v$ terms. With the addition of an exogenous paramagnetic contrast agent to the vascular space the change in R_2^* during neuronal activation becomes,

$$\Delta R_{2\ agent}^{*\ act} = \kappa_v(\Delta V_v(\chi_v+\chi_{agent})+(V_v+\Delta V_v)\Delta\chi_v)+\kappa_a\Delta V_a(\chi_a+\chi_{agent}) \tag{4.4}$$

where χ_{agent} represents the susceptibility difference between the contrast agent and surrounding tissue. This additional susceptibility contribution is opposite in sign to $\Delta\chi_v$. The change in ΔR_2^{*act} due to the presence of contrast agent can be calculated by considering the difference between equations 4.3 and 4.4;

$$\delta(\Delta R_2^{*\ act})_{agent} = (\kappa_v\Delta V_v + \kappa_a\Delta V_a)\chi_{agent} \tag{4.5}$$

Likewise the difference between the resting value of R_2^* and its value in the presence of contrast agent is given by,

$$\delta(R_2^{*\ rest})_{agent} = (\kappa_v V_v + \kappa_a V_a)\chi_{agent} \tag{4.6}$$

With the final assumption that the blood vessels within an imaging voxel are uniformly and randomly distributed ($\kappa_v = \kappa_a$) it is possible to combine equations 4.5 and 4.6 to yield the following,

$$\frac{\delta(\Delta R_2^{*\ act})_{agent}}{\delta(R_2^{*\ rest})_{agent}} = \frac{\Delta V_{tot}}{V_{tot}} \tag{4.7}$$

where $\Delta V_{tot} = \Delta V_v + \Delta V_a$ and $V_{tot} = V_v + V_a$. Therefore by varying the contrast agent concentration whilst stimulating neuronal activation the fractional change in total CBV (i.e. venous and arterial) can be measured. This

is achieved by slowly infusing a contrast agent whilst performing multiple cycles of a stimulus paradigm. The gradients of plots of $\Delta R_2^{*\ act}_{\ agent}$ and $R_2^{*\ rest}_{\ agent}$ versus contrast agent concentration can then be used to calculate fractional CBV change (ΔCBV) using equation 4.7.

In theory it is also possible to measure blood oxygen saturation, Y, using this technique. At the point where the susceptibility change, due to oxygenation, change is balanced out by the susceptibility due to the contrast agent, $\Delta R_2^{*\ act} = 0$. The contrast agent susceptibility at this point is known as χ_{agent}^{null}. It is then possible to rearrange equation 4.4 to calculate the change in venous susceptibility, $\Delta\chi_v$, again assuming $\kappa_v = \kappa_a$.

$$\Delta\chi_v = -\frac{\Delta V_v(\chi_v + \chi_{agent}^{null}) + \Delta V_a(\chi_a + \chi_{agent}^{null})}{V_v + \Delta V_v} \tag{4.8}$$

In previous experiments of this type it has been assumed that ΔV_a is zero, and so $\Delta V_v = \Delta V_{tot}$. Under this assumption the derivation can be simplified,

$$\begin{aligned} \Delta\chi_v &= -\frac{(\chi_v + \chi_{agent}^{null})\Delta V_v}{V_v + \Delta V_v} \\ &= -\frac{\chi_v + \chi_{agent}^{null}}{\frac{f_v V_{tot}}{\Delta V_{tot}} + 1} \end{aligned} \tag{4.9}$$

where $f_v = V_v/V_{tot}$, the venous blood volume fraction. Using the known molar magnetic susceptibility of ProHance it would then be possible to calculate $\Delta\chi_v$. From this information it is then possible to calculate Y using a simple model of blood susceptibility. In this model it is assumed that oxygenated blood has the same susceptibility as tissue [48] and hence only the susceptibility of deoxygenated blood, relative to tissue, is required.

$$\chi_{blood} = HCT(1 - Y)\chi_{dHb} \tag{4.10}$$

Technically it is only possible to calculate the $HCT(1-Y)$ product without further assumptions about the haematocrit (HCT) in the activated voxel. The haematocrit of venous blood can be measured *ex vivo*. However it is known that blood within the capillary bed has a reduced HCT due to the narrow dimensions of the vessels. Therefore blood drawn from large venous

veins will exhibit a higher haematocrit than would be observed for capillary blood, which in practice is unobtainable.

Experimental evidence suggests that the arterial volume does change during activation. Pears *et al.* [95] showed that equation 4.9 is particularly sensitive to the estimation of venous blood volume fraction. In their simulations they suggested that a 20 % error in the estimation of f_v would lead to a 15 % error in ΔY. To correct this error they developed a *varying arterial volume* model from equation 4.8.

$$\begin{aligned}\Delta\chi_v &= -\frac{\Delta V_{tot}}{V_{tot}}\frac{V_{tot}}{\Delta V_v}\left(\frac{1}{\frac{V_v}{\Delta V_v}+1}\right)\left(\chi_v+\chi_{agent}^{null}\right) \\ &\quad -\frac{\Delta V_a}{\Delta V_v}\left(\frac{\chi_a-\chi_v}{\frac{V_v}{\Delta V_v}+1}\right)\end{aligned} \tag{4.11}$$

To calculate $\Delta\chi_v$ using the varying arterial volume model, the relative proportion of venous and arterial blood volume must be known during rest and activation. When the study presented in this chapter was performed, measuring arterial CBV change was not possible, therefore Y could not be estimated.

4.2.2 Contrast Agents

During this experiment a paramagnetic contrast agent was infused in order to alter the characteristics of the haemodynamic response. Most clinical MR contrast agents are based on Gadolinium, which has the largest number of unpaired electrons in the periodic table. In a review paper by Caravan *et al.* [88] the relative merits of two other lanthanide metals are discussed. They are Dysprosium and Holmium which have larger magnetic moments due to orbital contributions to electron angular momentum. However due to the asymmetric nature of these states this leads to a very rapid electron relaxation time. Gadolinium(III) has a more stable symmetric S-state producing a much slower relaxation rate.

There are several Gadolinium-based agents approved for human use. The

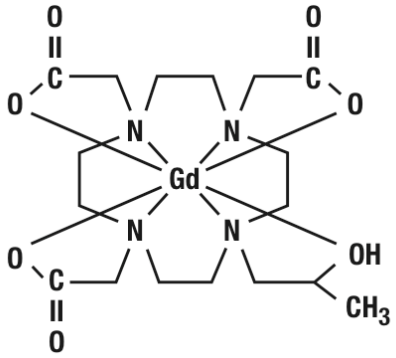

Figure 4.1: Gadoteridol structural formula [100].

most commonly encountered are gadopentetate dimeglumine, gadoversetamide, gadodiamide and gadoteridol (ProHance). Gadoteridol was considered to be the safest contrast agent and it was used throughout these experiments. The reasons for this decision are discussed in the following paragraphs.

The two main issues regarding contrast agent safety are toxicity and osmolality. When using power injectors a third problem, extravasation, may be encountered. Gadolinium is toxic in its ionic form, as well as being relatively insoluble at neutral pH values. Therefore it is commonly administered in a chelated form. Figure 4.1 shows the structural formula of gadoteridol. The ligand protects the body from the toxic Gadolinium ion within. However the free ligand can be similarly toxic. Dissociation of the complex could occur in several ways, via equilibration of the solution or a lack of chemical inertness. Dissociation through the former process would occur if the Gadolinium ions became substituted by endogenous metals or anions. To test this Wedeking *et al.* (see Caravan *et al.* [88]) studied bone deposition of Gadolinium in mice by the addition of radioactive isotopes, such as Gd-153 or Gd-159. Their results show that the percentage of the initial dose of gadoteridol deposited in bone was so small as to be undetectable (Table 4.1). The second method of dissociation would occur if the chelate could be broken down chemically. Caravan *et al.* [88] state that *"...an accumulated body of literature has shown*

that macrocyclic complexes tend to be significantly more inert." and that in particular analogues of DOTA, such as that used in gadoteridol, are *"...exceptionally inert as well as thermodynamically stable."*.

Table 4.1 notes the osmolality of the four most common agents. It is notable that gadodiamide and gadoteridol have the lowest osmolalities and were approved most recently. If an agent has an osmolality greater than that of blood, the osmolar pressure difference between the blood and the cells will cause an outflow of water from the cells. This will cause cell shrinkage and can ultimately result in cell death. Agents that act in this way are *hypertonic*. To compare how hypertonic each agent is, the ratio of the osmolalities of plasma (285 mOsmol/kg) and contrast agent can be calculated. At 2.2 times the osmolality of plasma gadoteridol is the lowest.

Finally the effect of extravasation was considered. Extravasation occurs when an agent is accidentally injected into tissue rather than into a venous vessel. It is thought that this is a greater problem when contrast agents are infused using power injectors, such as in this experiment. Runge *et al.* [112] studied the effects of extravasation of the same four contrast agents as discussed above. The study involved injecting 0.3 mL of each contrast agent into the hind limb of mice. After 48 hours the tissue was graded for necrosis, edema and inflammation. At all times the investigators were blinded to the identity of the contrast agent used in each mouse. The results show that gadoteridol causes the least tissue damage, and are summarised in table 4.2.

Brand Name	Generic Name	Chemical Name	% Initial Dose[a]	Osmolality[b]
Magnevist	Gadopentetate dimeglumine	$[Gd(DTPA)(H_2O)]^{2-}$	0.005	1960
Optimark	Gadoversetamide	$[Gd(DTPA\text{-}BMEA)(H_2O)]$	–[c]	1110
Omniscan	Gadodiamide	$[Gd(DTPA\text{-}BMA)(H_2O)]$	0.03	789
ProHance	Gadoteridol	$[Gd(HP\text{-}DO3A)(H_2O)]$	NDR[d]	630

Table 4.1: Currently approved Gadolinium Chelates. [a]Estimated mean percentage of initial dose/g in femur at 14 days [88]. [b]mOsmol/kg at 37°C [112]. [c]Data unavailable. [d]No detectable radiation.

Commercial Name	Necrosis	Edema	Inflammation
Magnevist	1.3	0.3	1.6
Optimark	0.7	0.3	0.9
Omniscan	0.3	0.1	0.7
ProHance	0.1	0.1	0.7

Table 4.2: Tissue histopathology results of extravastion at 48 hours [112]. Average rank scores (Higher score indicates more severe tissue damage).

The main acute side effect of these agents is a small risk of anaphylaxis. Anaphylaxis is characterised by respiratory, cardiovascular, or cutaneous reactions. In most previously examined cases of anaphylaxis due to contrast agent injection, the patient has had a history of respiratory difficulty or an allergic respiratory problem, such as asthma. There are a large range of anaphylactoid responses with acute reactions being relatively rare. The exact rate of occurrence of these reactions is difficult to determine but it has been suggested [113] to be between 1:100,000 and 1:500,000 of the whole population.

As a result of these investigations a number of exclusion criteria were used when selecting volunteer subjects, see table 4.3.

4.2.3 Pharmacokinetic Model

The work of McLachlan *et al.* [114] shows that the pharmacokinetics of ProHance are accurately modelled by an open two compartment model with renal clearance. Compartment 1 represents the vascular space, in essence the entire blood plasma volume, and compartment 2 the extracellular fluid space (e.g. tissue, muscle, etc.), see figure 4.2. This approach [115, 116] was applied in order to theoretically model the infusion and renal clearance phases of the experiment. The rate of change of the amount of contrast agent, A, within a compartment can be modelled by the following differential equation.

$$\frac{dA}{dt} = -kA \tag{4.12}$$

Criteria	Reason
Known hypersensitivity to any MR or X-ray contrast agent	Risk of anaphylaxis
A history of allergies	Risk of anaphylaxis
Any history of renal failure	Clearance
Any history of circulation problems (Vascular disease)	Extravasation
Pregnancy or breast feeding	Crosses placenta
A history of diabetes	Extravasation

Table 4.3: Exclusion criteria for subject recruitment

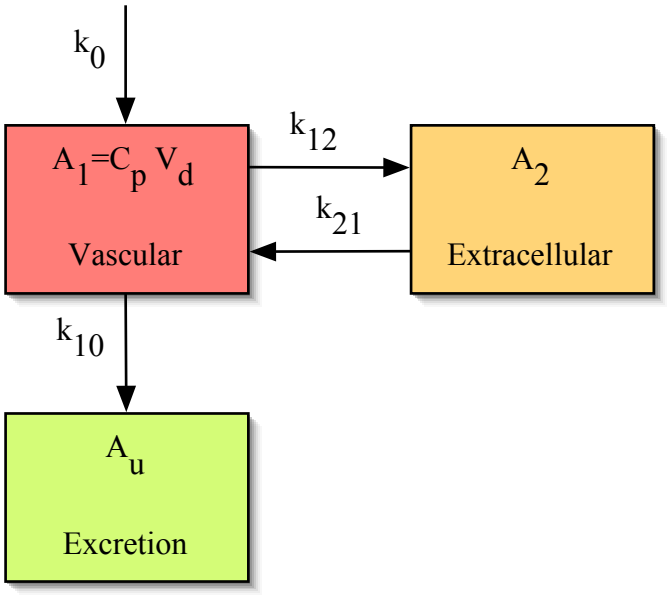

Figure 4.2: Open two compartment pharmacokinetic model.

The variable k represents a first order rate constant describing the clearance from the compartment. Consequently the following differential equations describe the changing amounts of contrast agent in each of the compartments, plus the amount excreted via the kidneys.

$$\frac{dA_1}{dt} = k_0 + k_{21}A_2 - k_{12}A_1 - k_{10}A_1 \quad (4.13)$$

$$\frac{dA_2}{dt} = k_{21}A_2 - k_{12}A_1 \quad (4.14)$$

$$\frac{dA_u}{dt} = k_{10}A_1 \quad (4.15)$$

Rate constants k_{12} and k_{21} characterise the movement of contrast agent between compartments and k_{10} is the rate of renal elimination from the system. Input into the system is denoted by a zeroth order rate constant, k_0, for intravascular injection. These rate constants are usually referred to as the *microscopic* rate constants. However the microscopic rate constants are not experimentally measurable. In practice the rate at which the agent is distributed, α, throughout the body and its elimination, β, from the body are measured. They are known as the *hybrid* rate constants.

$$\alpha + \beta = k_{12} + k_{21} + k_{10} \quad (4.16)$$

$$\alpha\beta = k_{21}k_{10} \quad (4.17)$$

If it is assumed that ProHance is a freely diffusable tracer then k_{12} is equal to k_{21}. Rearranging equations 4.16 and 4.17 gives equation 4.18 and its solution, equation 4.19.

$$k_{10}^2 - (\alpha + \beta)k_{10} + 2\alpha\beta = 0 \quad (4.18)$$

$$k_{10} = \frac{(\alpha + \beta) \pm \sqrt{(\alpha + \beta)^2 - 4 \cdot 2\alpha\beta}}{2} \quad (4.19)$$

McLachlan *et al.* obtained values for the distribution and elimination half-lives of (0.20 ± 0.04) hours and (1.57 ± 0.08) hours, respectively. The distribution and elimination half-lives are converted to rate constants using the following relationship.

$$k = \frac{\ln 2}{t_{\frac{1}{2}}} \quad (4.20)$$

In addition, the rate constants α and β are converted into units of minutes and are presented in table 4.4, alongside the solutions of equation 4.19.

Equations 4.13 to 4.15 were solved numerically in MATLAB to produce time-courses of the amount of contrast agent present in the plasma, tissue and urinary compartments. The infusion rate k_0 is normally expressed in units of mL min^{-1}. However by expressing k_0 in units of moles min^{-1} kg^{-1} it is possible to use equation 4.21 to calculate the plasma concentration, C_p, of contrast agent. A triple dose (0.6 mL kg^{-1} or 0.3 mmol kg^{-1}) of ProHance infused over 16 minutes gives a k_0 value of 1.875×10^{-5} moles min^{-1} kg^{-1}.

$$C_p = \frac{A_1}{V_d} \tag{4.21}$$

The volume of distribution, V_d, is defined as the volume in which the amount of contrast agent would need to be distributed to produce the observed plasma concentration. This does not necessarily reflect the true plasma volume and for ProHance it has been measured as (204 ± 58) mL kg^{-1}. The right hand y-axis of figure 4.3 displays the plasma concentration of ProHance in units of mM.

4.3 Method

Ethical approval for this study was obtained from the University of Nottingham Medical School Ethics Committee in September 2003. The experimental paradigm of the study is described in section 4.3.1. This section is followed by details of the method used to determine *in vivo* contrast agent concentration and a description of the image analysis used.

4.3.1 Imaging

Imaging was performed on the 3.0 T EPI scanner which was purpose built at the SPMMRC in the early 1990's. Excitation was via a TEM volume coil and reception by means of an occipital surface coil [117] located beneath the subject's head. Two images were acquired after a single excitation using

Rate Constant	Solution 1	Solution 2
α	0.0578	
β	0.0073	
k_{10}	0.0471	0.0181
k_{12}	0.0090	0.0235
k_{21}	0.0090	0.0235

Table 4.4: Distribution and elimination rate constant solutions for a compartmental model of Gadoteridol pharmacokinetics (min^{-1})

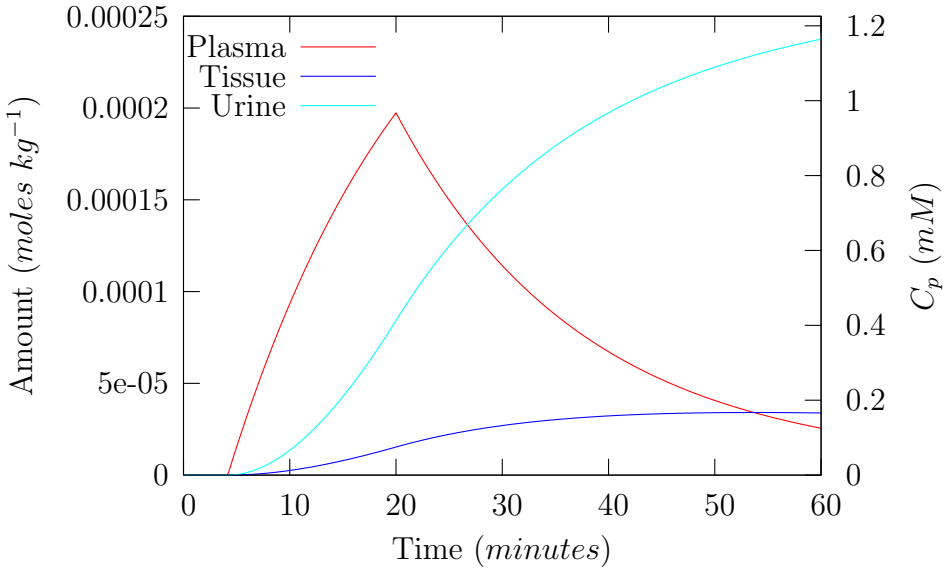

Figure 4.3: Numerical solution to equations 4.13 to 4.15 during a 16 minute infusion of a triple dose of ProHance (starting at 4 minutes, ending at 20 minutes). The rate constants used are listed in table 4.4 (Solution 1) and the right hand $y-$axis displays the plasma concentration in mM.

	Regime 1	Regime 2
Echo Times	27 ms, 52 ms	23 ms, 41 ms
Switch Frequency	1.38 kHz	1.90 kHz
Resolution	$4 \times 3 \times 4$ mm	$3 \times 3 \times 4$ mm

Table 4.5: Parameters used in scanning regimes.

a multi-echo EPI sequence, and a matrix size of 64×64. The cartesian MBEST [17] technique was used to encode EPI images. Initially echo times of 27 ms and 52 ms were used but were later superseded by shorter echo times of 23 ms and 41 ms. The parameters used in each regime are summarised in table 4.5. By increasing the switching frequency, shorter echo times could be selected and an increase in SNR was achieved, particularly in the case of the second echo. In turn this improved the estimation of R_2^*. In both regimes the volume repetition time was 300 ms. During scanning the RF power was controlled such that the flip angle operated at the approximate value of the Ernst angle.

Manual shimming was performed using a body shim set. A 16 slice single echo image set was initially acquired. These images were used to locate the three sagittal slices in the visual cortex to be used for the fMRI experiment. Prior to the fMRI experiment a multi-slice inversion recovery sequence was performed acquiring 5 slices per excitation at 10 different inversion times between 100 ms and 3000 ms (volume repetition rate 4 s). This was achieved by non-selectively inverting the whole volume and sampling each slice with a slice-selective 90° pulse. This results in a spread of inversion times across the slices, each slice being separated by the time taken to acquire the preceding image. Additionally the same 5 slices were acquired at 4 different echo times ($\Delta TE = 25$ ms or 18 ms), with a slice repetition rate of 2 s. This data was used to create resting state maps of T_1 and T_2^*, respectively.

Intravenous cannulation of both of the subject's forearms was performed prior to positioning them within the scanner. Extension tubing was used to connect the right arm cannula to two infusion pumps, located outside the

magnet room. Parallel pumps were used to achieve sufficient flow rate to infuse a triple dose of contrast agent over a period of 16 minutes. The left hand cannula was used to sample the blood at a selection of time points (see section 4.3.2). Additionally the subject was kept warm in order to retain patency of the cannulas and their head immobilised in the volume coil with foam padding to reduce motion.

The stimulus for the fMRI experiment was provided by a pair of red LED goggles, flashing at 8 Hz. The paradigm consisted of 20 cycles, each cycle comprising 4.8 s *on* and 55.2 s *off* periods. Each cycle of the paradigm produced 200 volumes of three slice, double-echo data. In addition the experiment was preceded by 20 volumes to allow a steady state condition to be attained, yielding a total of 4020 volumes. Contrast agent infusion commenced 4 minutes after the start of the experiment and ended 16 minutes later. During the visual stimulus paradigm, subjects were asked to press a button following an audible cue in order to maintain alertness. This additional button-press paradigm was placed 30 s after the visual stimulation had ended. By placing this *stimulus* at this time point it was hoped that it would not interfere with the visual haemodynamic response. Any small effect of the button-press would also have decayed prior to the onset of the subsequent visual stimulus cycle. A second set of T_1 and T_2^* maps were then acquired, following the fMRI experiment.

4.3.2 Determination of Contrast Agent Concentration

In order to determine the blood contrast agent concentration *in vivo* a number of 4 mL blood samples were taken from the left hand cannula. In early experiments time points spanned the length of the fMRI paradigm and in later experiments time points were spread post-infusion, see table 4.6. This allowed the pharmacokinetics of the infusion and clearance periods to be determined. Blood samples were stored in 5 ml heparinised bottles and maintained at a temperature of 37 °C. Prior to the start of the fMRI experiment a further seven 4 ml blood samples were taken and a measured volume of a

Sample	1	2	3	4	5
Infusion	7	11	15	19	29
Post-Infusion	3	6	13	20	30

Table 4.6: Approximate blood sample time points in minutes after the start of the fMRI experiment (Infusion) and after the end of the fMRI experiment (Post-Infusion), respectively.

50 mM contrast agent solution added; 10 μl, 20 μl, 30 μl, 40 μl, 50 μl, 60 μl. At the conclusion of the fMRI experiments the scanner was re-configured to slice coronally and both sets of blood samples were subjected to a single slice inversion recovery sequence, at 42 separate inversion times, between 14 ms and 4012 ms, to cover the whole range of expected T_1 values.

The samples containing added contrast agent were used to produce a T_1 versus contrast agent concentration calibration curve. Blood oxygenation was not measured and was assumed to change little during sample preparation. Calibration curves from all subjects were combined and a linear regression performed, figure 4.4a. In turn this was used to produce *in vivo* time-courses of contrast agent concentration, figure 4.4b. The maximum blood concentration of contrast agent was relatively consistent with the pharmacokinetic model of section 4.2.3, given the errors in the hybrid rate constants, α and β. To improve the model these constants would require measurement on a scale of minutes, rather than hours. However the appreciable difference between individuals means that accurate prediction is very difficult.

4.3.3 Image Analysis

Data from the fMRI experiment was treated with a number of post-processing techniques prior to analysis. Processes that would have applied significant temporal smoothing to the data were avoided, to retain features of the haemodynamic response that occur on short time scales. Similarly spatial smoothing was also omitted. For each of the steps described below, in-house

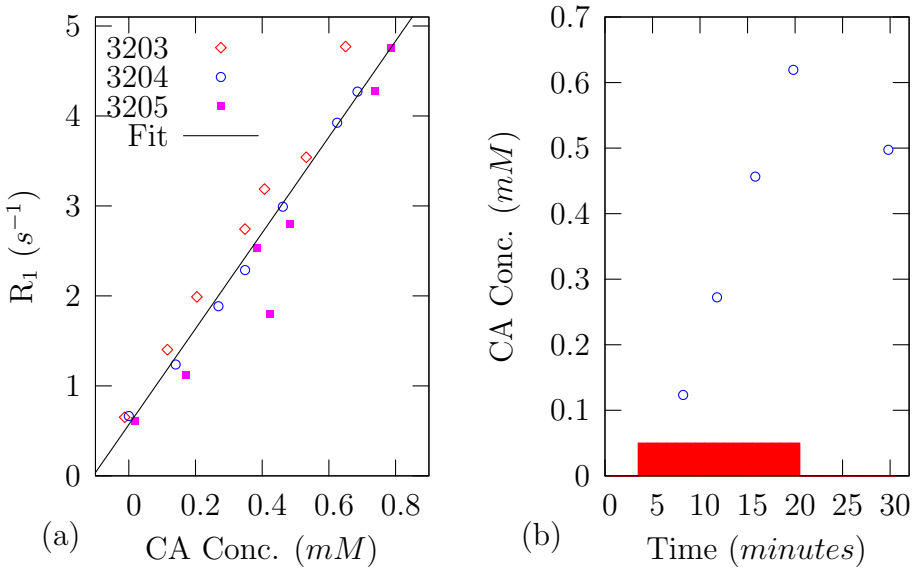

Figure 4.4: Contrast agent (CA) blood measurements: (a) R_1 calibration curve ($n = 3$), (b) example *in vivo* concentration curve. Infusion timing designated by the filled red box.

software was used unless otherwise stated.

Initially complex time data was Fourier transformed to the image domain and stored in the Analyze [74] format. Two separate files were created, containing each of the echoes, and motion correction was performed on the first echo data set in SPM2 [75]. The resulting motion transformations were applied to the second echo data set using a custom batch script. Realigned data was then used to create maps of T_2^*.

Activation maps were created from first echo data in SPM2, using an average *in vivo* contrast agent time-course as a regressor. This allowed the confounding effect of a continually changing baseline to be approximately corrected for, and therefore 20 stimulus cycles could be tested. Resultant activation maps were thresholded to produce a cluster of 20 pixels. Region of interest time-courses were then extracted from the T_2^* maps, using the cluster as a mask. These time-courses were averaged to produce a single

time-course. Subsequent analysis was performed in MATLAB to calculate the fractional change in total CBV ($\Delta V_{tot}/V_{tot}$).

The extracted T_2^* time-course was converted to R_2^* and plotted versus contrast agent concentration. Therefore R_2^* and ΔR_2^* can be found to be a linear function of contrast agent concentration. Using equation 4.7 it is possible to calculate $\Delta V_{tot}/V_{tot}$ from this plot. Firstly the 1st time point of each stimulus cycle was plotted as a function of contrast agent concentration. The gradient of a linear fit to this data yields $\delta(R_2^{*\ rest})_{agent}$. Secondly the difference between the 1st and nth time points of each cycle were calculated and plotted versus contrast agent concentration. In this analysis the 1st time point was chosen to represent a resting blood volume level. The nth time point is a point for which a ΔCBV value is required. The gradient of a linear fit to this data gives $\delta(\Delta R_2^{*\ act})_{agent}$. These values can then be substituted into equation 4.7. The gradient and intercept, of the linear fits described above, were calculated using a matrix inversion technique. The fitting error of the gradient was then calculated in order to estimate the error in the measured value of $\Delta V_{tot}/V_{tot}$.

4.4 Results

BOLD activation was detected in the visual cortex across all subjects (see figure 4.5). As the blood concentration of contrast agent increased a baseline drift was observed, as expected (see figure 4.6a). It was also observed that the peak amplitude of the BOLD response reduces with increasing concentration, figure 4.6b. An interesting feature of this experimental data is the increase in BOLD signal for the average of stimulus cycles 5-8, i.e. average contrast agent concentration 0.11 mM. This increase in signal may be caused by the infused contrast agent. At low concentrations the contrast agent can act to reduce microscopic magnetic field gradients in the blood, therefore reducing dephasing. For a more detailed discussion of this effect, see chapter 3.

Figure 4.7 shows an example of a fractional CBV ($\Delta V_{tot}/V_{tot}$) measure-

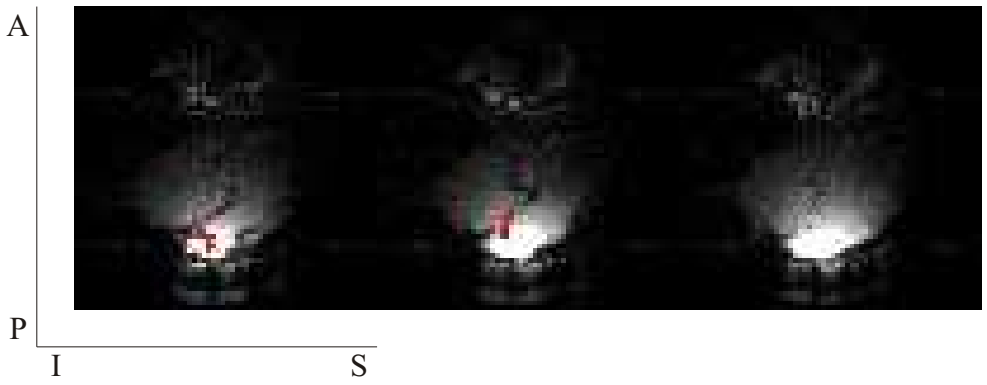

Figure 4.5: Activated cluster of 20 pixel time-courses located in the visual cortex determined using BOLD contrast. Base images were acquired in the sagittal plane.

ment, as described in section 4.2.1. Using this technique the peak volume change of each subject was calculated and these are summarised in table 4.7. It is unclear whether the magnitude of the BOLD response is related to that of the CBV change, figure 4.8. A 1st order fit to the data is statistically insignificant giving a p-value of 0.18. Many more subjects and a wider range of stimuli would be required to increase the statistical power. The fractional change in CBV is calculated to have a mean value of 0.23±0.10. This agrees well with previous work [95] where a mean value of 0.28±0.02 was calculated. It is likely that the difference in results is due to the length of the stimulus. In the previous work visual stimulus was applied for 12s, compared to 4.8 s in this experiment. It is a commonly held belief that the venous vessels post-capillary exhibit a visco-elastic ballooning effect. In this case a lower peak volume change might be expected if the visco-elastic limit of this balloon has not been reached.

Finally the same technique was applied to every time point, with respect to the same resting reference, to produce a volume change time-course, figure 4.9. Figure 4.9 suggests that total volume change lags behind the BOLD signal, particularly in the post-stimulus phase, and may not display a negat-

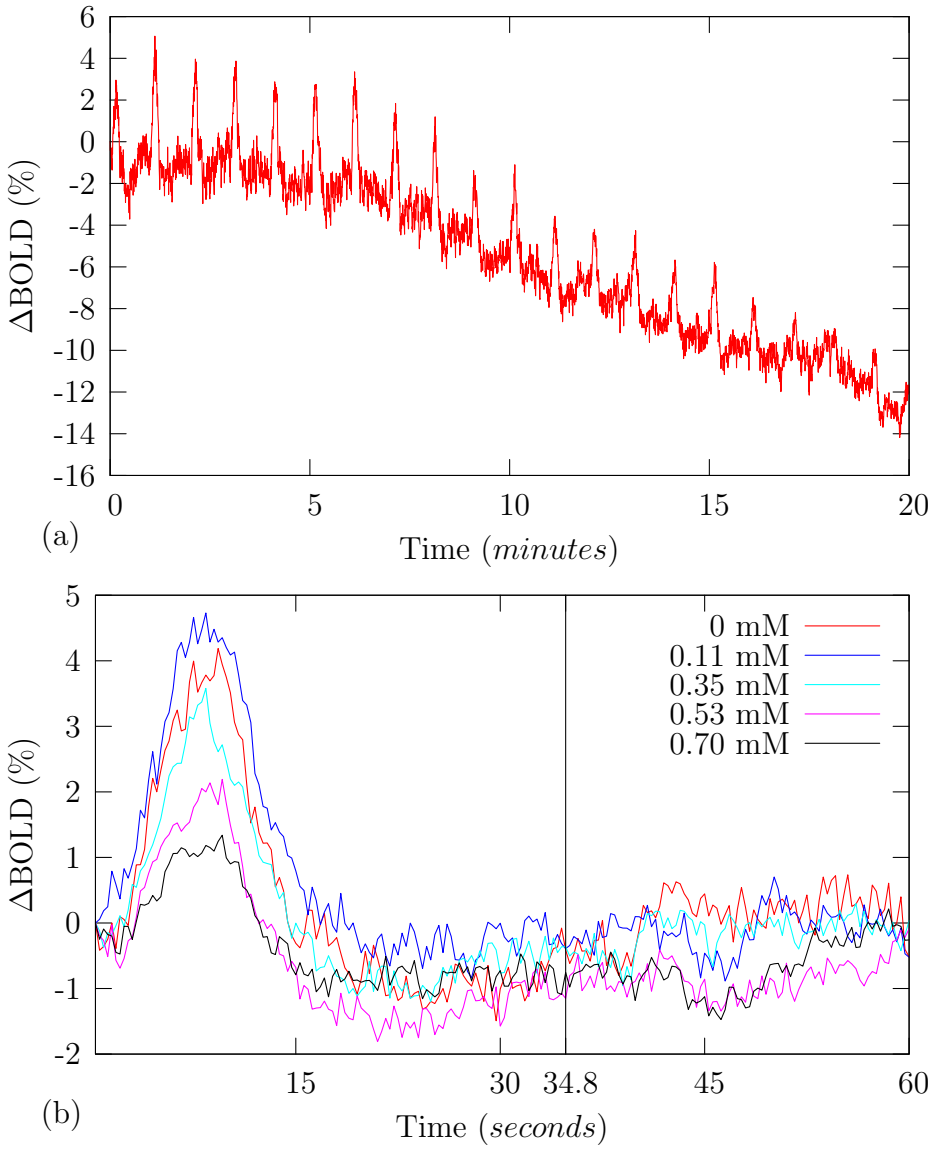

Figure 4.6: Experimental results: (a) inter-subject average BOLD signal ($n = 5$) and (b) baseline corrected data averaged as blocks of four cycles. A single vertical black line denotes the timing of the button-press paradigm.

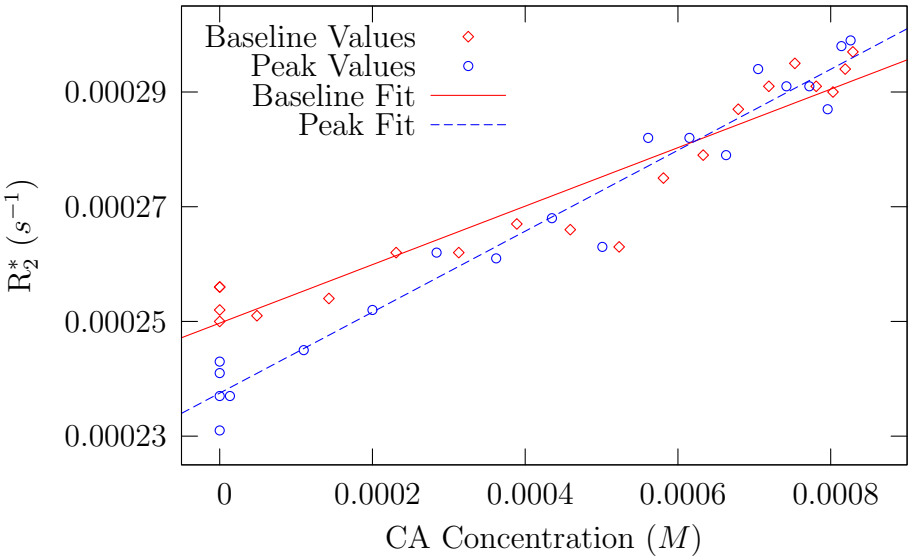

Figure 4.7: R_2^* values extracted at peak and baseline of the haemodynamic response, for each stimulus cycle (3205).

Subject	ΔCBV	ΔBOLD
3133	0.12±0.05	0.08±0.01
3204	0.27±0.16	0.10±0.01
3205	0.38±0.08	0.07±0.01
3259	0.22±0.10	0.04±0.01
3264	0.16±0.13	0.05±0.01
Mean	0.23±0.10	0.07±0.01

Table 4.7: Peak change in ΔCBV calculated at peak BOLD signal alongside BOLD signal change, both as a fraction of their resting values.

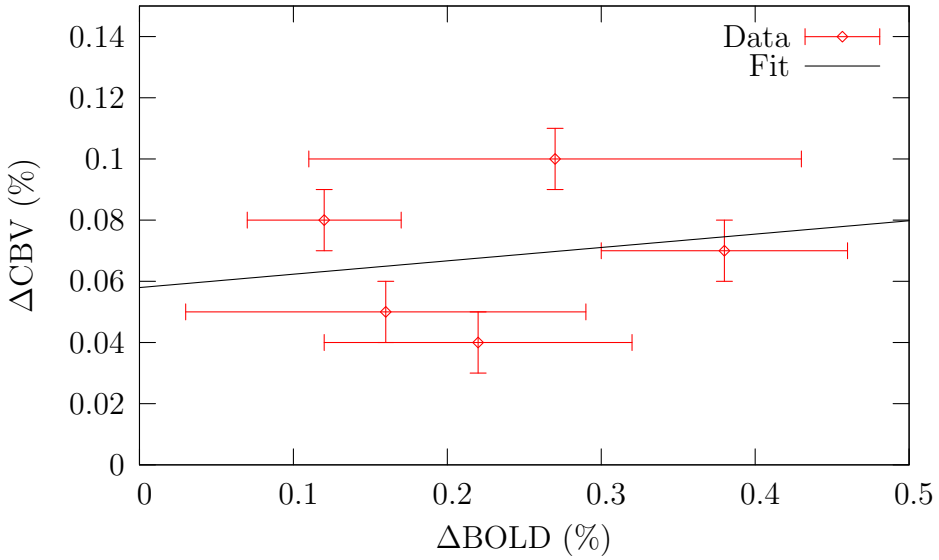

Figure 4.8: Peak ΔCBV versus peak ΔBOLD, from table 4.7, with a linear regression to the data. Each data point represents an individual subject.

ive initial dip. The BOLD post-stimulus undershoot (15 - 45 s) appears to continue beyond the point at which the volume returns to baseline, although it is difficult to confirm this in a quantitative way. It has previously been suggested [118] that the post-stimulus undershoot is due to a delayed compliance of the venous vessels. If confirmed this result would suggest that this is not the only cause of the post-stimulus undershoot.

4.5 Discussion

This study shows that it is possible to measure fractional CBV during an event related stimulus. Furthermore it shows that it is possible to produce high temporal resolution fractional CBV time-courses in humans.

This experimental methodology provides an interesting way of probing the BOLD haemodynamic response and teasing out one of the underlying contributors to the BOLD signal; volume change. This is due to the way

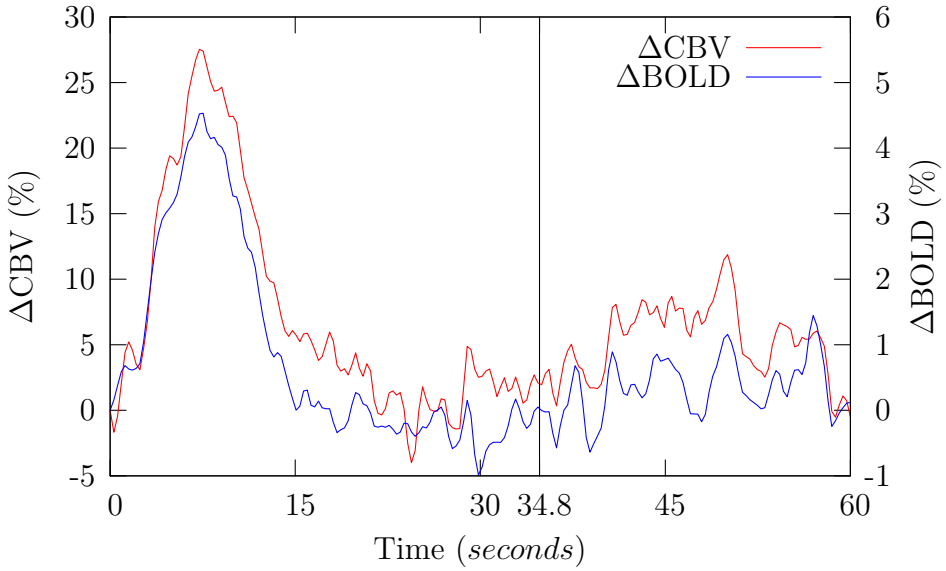

Figure 4.9: Experimental inter-subject average of BOLD and CBV measurements ($n = 5$). A single vertical black line denotes the timing of the button-press paradigm.

that temporal characteristics of the response are differentially affected by the contrast agent. Aspects of the response that are strongly dependent on volume change will see the greatest decrease in signal intensity, and hence increased R_2^*. In a qualitative way comparing the different curves of figure 4.6b demonstrates the volume dependence of the major features of the BOLD response. The BOLD overshoot signal intensity drops by a factor of 4 during the 16 minute infusion due to the contrast agent. This shows that this feature has the greatest dependence on volume change. The other major feature of the response is the post-stimulus undershoot, occurring between 15 seconds and 45 seconds (although possibly longer). Figure 4.6b suggests this feature has only a limited dependence on volume change. Variation in the magnitude of the signal could easily be explained by inter-stimulus variability, which can be appreciable. As noted in section 4.4, conventionally the post-stimulus undershoot is thought to be the result of a delayed

return to baseline of CBV relative to cerebral blood flow (CBF). However there is increasing evidence to suggest this is not the case. Lu *et al.* [70] measured CBF, CBV and BOLD and used this data to produce maps of activity. They then extracted the time courses of voxels that were activated in all three techniques. This enabled them to show that there were negligible changes in CBF and CBV during the post-stimulus undershoot present in the BOLD weighted time courses. This led them to the conclusion that oxidative metabolism is sustained beyond the recovery of flow and volume to baseline levels. In order to justify this conclusion they reference several pieces of supporting evidence. Firstly in the work of Devor *et al.* [119] it is suggested that their spectroscopic optical images show an increased concentration of deoxyhaemoglobin following the return to baseline level of total haemoglobin content. In this context the total haemoglobin content is the corpuscular equivalent of CBV. However this change is quite small and in their later work [120] deoxyhaemoglobin content appears to reduce in this time period. Secondly, Thompson *et al.* [121] performed measurements of pO_2 and spiking activity using the orientation selective visual pathway. As the optimal grating orientation of the neuron was approached, the spike rate increased to a maximum. This was accompanied by an increase in the extent of both the initial dip and post-stimulus undershoot in pO_2. Thirdly, Ances *et al.* [122] performed simultaneous Laser Doppler Flowmetry and pO_2 measurements. They showed a sustained tissue pO_2 decrease following the recovery of CBF.

Further evidence can be found in the literature. Toronov *et al.* [123] performed simultaneous fMRI and Near Infrared Spectroscopy (NIRS) of the motor cortex. They state that the lag between CBF and CBV change cannot account for the post-stimulus undershoot and suggest that it is due to an undershoot in CBF. This view is in disagreement with some of the work described above [70, 122]. In the work of Schroeter *et al.* [71] simultaneous fMRI and NIRS is also performed. However, this study concentrates specifically on the origin of the post-stimulus undershoot. They conclude that the

temporal characteristics of the deoxyhaemoglobin time course were highly correlated with those of the BOLD response and that the contribution of a delayed return to baseline of blood volume was 'ambiguous'.

In summary, the results presented in this chapter lend added support to the hypothesis that the post-stimulus undershoot is a feature of sustained oxidative metabolism. These results are in general agreement with the literature surveyed above.

Future work will involve modelling this experiment through the Balloon model [47]. This will allow an even greater insight into the underlying haemodynamic mechanisms to be gained. It will also help to test the response of existing models to an event related paradigm. There is also much to be gained by repeating this experiment. As was noted in section 4.2.1, by measuring arterial CBV, in an additional experiment within the same session, it will be possible to measure $\Delta\chi$, leading to *in vivo* measurements of blood oxygen saturation. Since this study a newly developed technique has emerged to measure arterial CBV [124], allowing the varying arterial volume model to be utilised. This experiment could also be performed at 7.0 T yielding a considerable increase in SNR. This will also allow total CBV change to be measured with higher spatial resolution, allowing the spatial specificity of the BOLD response to be probed.

Chapter 5

Modelling the BOLD Response

5.1 Introduction

Many theoretical models of the BOLD response have been proposed in recent years. However little has been done to validate these models experimentally. Therefore, the aim of the simulation work presented in this chapter is to test models of the BOLD response against experimental data. As was noted in chapter 4 the experimental paradigm, described therein, is an interesting way to probe the underlying mechanisms of the BOLD response. In this work an infusion protocol is simulated using the Balloon model proposed by Buxton *et al.* [47]. A multi-component signal model is also developed in order to account for susceptibility changes in the arterial vasculature.

5.2 State of the Art

In this section the current state of BOLD modelling is reviewed. The most significant attempt at modelling the BOLD response, thus far, was contributed by Buxton *et al.* [47] in 1998 in the description of the *balloon model*. This original work has been built upon to improve the predictive power of the BOLD model. The balloon model is based on a set of assumptions; (1) that there is no capillary recruitment, (2) volume change due to arteriolar

dilation is negligible and (3) that all of the deoxyhaemoglobin in the vasculature is present in the venule. In essence the BOLD response is presumed to be entirely due to the venous vasculature.

Input to the system is provided by a flow function, $F_{in}(t)$, mimicking the effect of arteriolar dilation. In order to simplify the model the flow out, $F_{out}(V,t)$, of the venule is defined as a function of volume. Conventionally this would be considered a function of the pressure into and out of the system, and the vascular resistance. However $F_{out}(V)$ is defined such that the difference between flow into and out of the system is equal to the change in volume of the venule.

$$\frac{dV(t)}{dt} = F_{in}(t) - F_{out}(V,t) \tag{5.1}$$

Similarly by considering the amount of deoxyhaemoglobin, $Q(t)$, entering and leaving the system the change in deoxyhaemoglobin can be defined as,

$$\frac{dQ(t)}{dt} = F_{in}(t)C_aE(t) - F_{out}(V,t)\frac{Q(t)}{V(t)} \tag{5.2}$$

where C_a is the arterial oxygen concentration and $E(t)$ is the oxygen extraction fraction. The first term on the right hand side of this equation is equivalent to the steady state definition of the cerebral rate of oxygen metabolism ($CMRO_2$).

$$CMRO_2 = F_{in}(t)C_aE(t) \tag{5.3}$$

The variables in equations 5.1 and 5.2 can be normalised by their respective baseline values to aid simulation, and are signified as such by lowercase letters.

$$\frac{dv(t)}{dt} = \frac{1}{\tau_{MTT}}\Big[f_{in}(t) - f_{out}(v,t)\Big] \tag{5.4}$$

$$\frac{dq(t)}{dt} = \frac{1}{\tau_{MTT}}\Big[f_{in}(t)\frac{E(t)}{E_0} - f_{out}(v)\frac{q(t)}{v(t)}\Big] \tag{5.5}$$

The constant τ_{MTT} is the mean transit time and is equal to V_0/F_0, where V_0 is the resting volume fraction and F_0 is the resting flow. Also note that it is assumed that arterial blood is fully oxygenated ($C_a = 1$) and therefore does not contribute to BOLD signal changes.

Three variables in the equations above require model definitions; $f_{in}(t)$, $f_{out}(v,t)$ and $E(t)$, where $f_{out}(v,t)$ is also dependent on $v(t)$. The models of these variables are described in the following sections.

5.2.1 Flow Models

Three models of neurovascular coupling were drawn from the literature and investigated. The first model was proposed by Miller *et al.* [125] and takes a largely empirical approach by considering non-linearity in cerebral blood flow measurements. The second model by Friston *et al.* [72] takes a more theoretical approach and relates flow to a flow inducing signalling mechanism. Lastly the model of Behzadi *et al.* [126] extends the work of Friston *et al.* by proposing that the signalling mechanism induces changes in the muscular compliance of the cerebral arteriole, which in turn leads to changes in flow. All three models represent a more realistic description of blood flow than the box car employed in the original work of Buxton *et al.* [47]. The following sections describe the models cited above.

Miller *et al.*

The model presented by Miller *et al.* [125] was based on experimental flow measurements acquired using the QUIPPSII arterial spin labelling pulse sequence. Visual and motor paradigms were performed with three separate stimulus lengths; 2, 6 and 18 s. The stimulus lengths were chosen specifically to allow linearity comparisons to be made. For example, the result from the 2 s stimulus was time shifted by 0, 2 and 4 s and summed. This summation was then compared with the 6 s stimulus. They observed that for the motor experiment flow was slightly over predicted by the summation, whereas for the visual paradigm it was strongly over predicted. With this in mind they postulated that non-linearities in the flow response were already present in the neural response, preserving a linear relationship between the two. A two step modelling approach was used to link stimulus to flow; stimulus input to neural activity and neural activity to flow change. The form of the neural

Paradigm	a	τ_n	τ_h	m	t_d	c
Visual	3.0	0.5	1.5	3.0	1.5	54
Motor	0.25	0.25	1.25	3.0	0.65	65

Table 5.1: Parameter values obtained by Miller *et al.* [125] by simultaneously fitting their model to experimental flow measurements.

response was chosen to model neural adaptation, characterised by a decay from a high initial neural firing rate to a lower steady state value during stimulation. This pattern has been observed in magnetoencephalography (MEG) recordings [127] and can be described by the following function,

$$n(t) = \begin{cases} 1 + ae^{-t/\tau_n} & 0 \leq t < T \\ 0 & \text{otherwise} \end{cases} \tag{5.6}$$

where a represents the amplitude of the initial overshoot, τ_n a time constant regulating the decay and T the time at which stimulation ceases. In the second stage of the model the neural function $n(t)$ was convolved with a gamma-variate $h(t)$, representing the haemodynamic impulse function,

$$h(t) = \frac{c}{\tau_h m!}\left(\frac{t - t_d}{\tau_h}\right)^m e^{-(t-t_d)/\tau_h} \tag{5.7}$$

where τ_h controls the falling edge of the curve, m affects the shape of the function, t_d delays the onset of the curve and c scales the response. Figure 5.1 plots equations 5.6 and 5.7 along with the convolution of the functions. Miller *et al.* then performed a six parameter fit of this model to the experimental flow data. Interestingly little variation in the parameters of the model across paradigms was observed. The exception, however, was the parameter a which varied from 0.25 in the motor experiment to 3.0 for the visual paradigm, see table 5.1. This parameter determines the magnitude of the high initial neural firing rate and hence adaptation in the response. Essentially this may distinguish passive (visual) stimulation from self-initiated (finger tapping) stimulation as the latter will likely involve less adaptation.

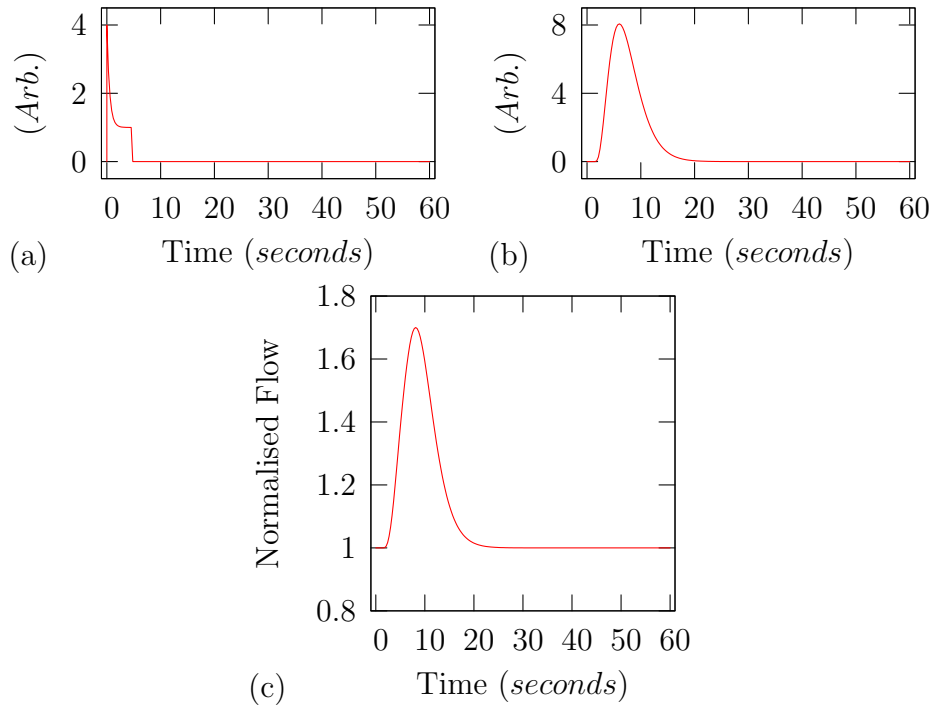

Figure 5.1: Model relating a 4.8 s stimulus to flow response using the fitted parameters for a visual paradigm described in Miller *et al.* [125]: (a) neuronal response $n(t)$, (b) haemodynamic response $h(t)$, (c) convolution of neuronal and haemodynamic responses, $n(t) \otimes h(t)$, to produce the normalised flow response.

Friston *et al.*

Although the model of Miller *et al.* satisfies their hypothesis it does not attempt to suggest an underlying mechanism for flow change. In the work of Friston *et al.* [72] such a mechanism was proposed. They suggested that flow change was mediated by a signalling mechanism that was dependent on the stimulus input function. As was suggested in Miller *et al.* this relationship was assumed to be linear, giving the following relationship between flow and a flow inducing signal, $s(t)$.

$$\frac{df_{in}(t)}{dt} = s(t) \tag{5.8}$$

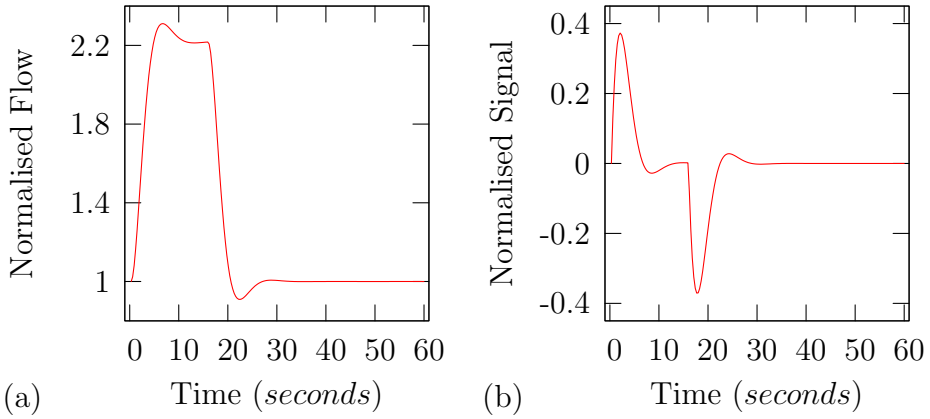

Figure 5.2: Mechanistic model (proposed by Friston *et al.* [72]) relating a 4.8 s stimulus to a corresponding flow change: (a) flow input response, and (b) signalling response.

The change in the flow inducing signal was assumed to be generated by neural activity, $u(t)$, but controlled by feedback from both the signal itself and autoregulation of flow. Autoregulation describes the capacity of the vasculature to maintain constant blood flow despite changes in arterial pressure.

$$\frac{ds(t)}{dt} = \epsilon u(t) - \frac{s(t)}{\tau_s} - \frac{(f_{in}(t) - 1)}{\tau_f} \tag{5.9}$$

The parameters ϵ, τ_s and τ_f determine the temporal characteristics of the change in flow. The constant, ϵ, was named the neuronal efficacy, and drives the increase in signal, τ_s represents the decay of the signal and τ_f controls autoregulatory feedback from flow.

Figure 5.2 shows the result of solving equations 5.8 and 5.9. The resultant model curves are consistent with the empirical data presented in Miller *et al.*. In addition the suggested mechanism linking neural activity to increase in flow is physiologically plausible. For some time it has been known that astrocytes are involved in the clearance of glutamate and its conversion to glutamine [128]. The physiological analogue of this model could be the glutamate mediated release of vasodilators causing changes in flow.

Behzadi *et al.*

The model proposed by Behzadi *et al.* [126] was a reformulation of the work of Friston *et al.*. This model was named the Arteriolar Compliance model, and proposed a simplified picture of arteriolar vessel compliance. The vessel walls are expected to experience both intravascular and extravascular forces. The balance of these forces changes during increases in flow and hence the radius of the arteriole varies. In order to simplify the modelling of arteriolar compliance they assumed that the extravascular forces were constant and that therefore the overall compliance of the vessel was determined by the circumferential stress of the vessel wall. The circumferential stress was described as being due to active and passive components. The active stress was attributed to changes in smooth muscle tone and the passive stress to elastic connective tissues. Over the operating range of the arteriole the relative contributions of these components was assumed to vary. It was suggested that at rest the compliance was dominated by the active component, whilst at large arteriole radii the passive stress component would dominate. This led to the dependence of total compliance on muscular compliance, for which a model was derived. Figure 5.3a presents the numerical results of this model showing the increasing dominance of passive stress at large radii. The muscular compliance, C_m, was a non-linear function of radius, as shown in figure 5.3b. The implication being that small changes in radius, and hence blood flow, were easily achievable.

A link was then established between normalised muscular compliance, c_m, and neural activity by adapting equations 5.8 and 5.9.

$$\frac{dc_m(t)}{dt} = s(t) \tag{5.10}$$

$$\frac{ds(t)}{dt} = \epsilon u(t) - s(t)k_s - (r(c_m)^{\gamma_b} - 1)g_f \tag{5.11}$$

Constants k_s and g_f control signal and flow feedback mechanisms, and are the reciprocal of τ_s and τ_f used by Friston *et al.* [72]. The change in arteriolar muscular compliance was then described as a function of the signalling quantity, $s(t)$. Similarly the flow term in equation 5.9 was replaced by the

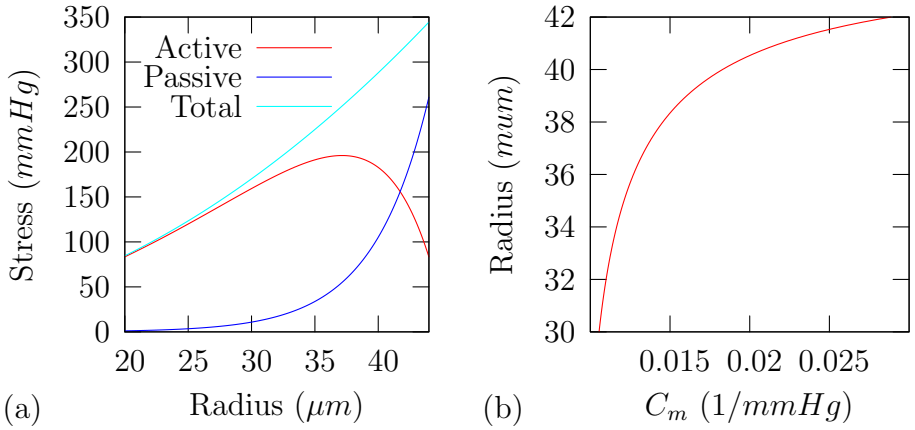

Figure 5.3: Model of the muscular compliance of an arteriole [126]: (a) balance of circumferential stresses in the vessel wall and (b) muscular compliance as a function of vessel radius.

arteriolar radius raised to the power gamma. Changes in arteriolar radius are dependent on muscular compliance. The value of gamma depends on the assumed relationship between flow and radius. For laminar flow $\gamma_b = 4$ and for plug flow $\gamma_b = 2$. In this work, flow was assumed to be laminar. In order to solve equations 5.10 and 5.11, the equation modelling the relationship between muscular compliance and arteriolar radius must be inverted. Inverting this relation is very difficult and therefore a look up table was used. Changes in CBF were calculated by raising the radius r to the power 4. Similarly the arteriolar volume change was calculated by r^3. Figure 5.4 shows the numerical solution produced by the parameters suggested by Behzadi *et al.* Whilst it appears that this solution is not consistent with the empirical data of Miller *et al.*, it was possible to produce curves resembling this work through judicious choice of the controlling parameters ϵ, k_s and g_f.

5.2.2 Volume Models

Three models of venous compliance were investigated. The first model is based on empirical observations by Grubb *et al.* [129]. The application of

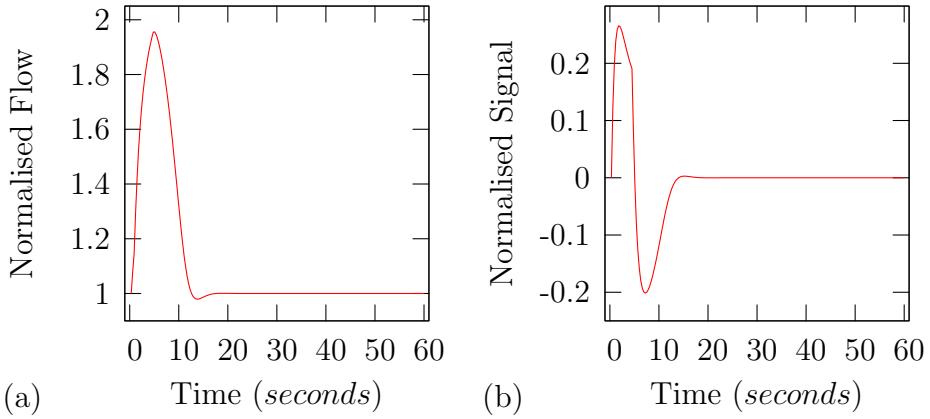

Figure 5.4: Mechanistic model (proposed by Behzadi *et al.* [126]) relating a 4.8 s stimulus to a corresponding flow change: (a) flow input response, and (b) signalling response.

this experimental evidence is best described in the work of Mandeville *et al.* [68] and relates blood flow to blood volume via a power law. The second model extends this work to account for dynamic changes in flow [130], and the third model, proposed by Kong *et al.* [131], extends the delayed compliance implicit in the Windkessel model [68]. All three models are described in further detail in the following sections.

Grubb *et al.*

Experiments to measure the relationship between cerebral blood flow and total cerebral blood volume were performed by Grubb *et al.* [129]. Flow and blood volume were measured in rhesus monkeys at different levels of Pa_{CO_2} using Positron Emission Tomography. The Pa_{CO_2} level was lowered by hyperventilation and raised by hypoventilation. A steady state was established at each Pa_{CO_2} level by waiting at least 15 minutes prior to imaging. From these experiments the relationship between flow and total blood volume was found to be best described by a power law, where the power constant is now known as Grubb's constant. In equation 5.12 CBV is defined as the total

cerebral blood volume and *CBF* as the cerebral blood flow.

$$CBV = 0.80\ CBF^{0.38} \tag{5.12}$$

Mandeville *et al.* [68] described the significance of this equation best, and reformulated the static model as equation 5.13. The sum of α and β (henceforth denoted γ_m) are equivalent to the reciprocal of Grubb's constant. It is assumed that $\alpha = 2$ for laminar flow and that $\beta > 0$ and is a function of the balloon's compliance and capacitance. Mandeville *et al.* [68] measured $\gamma_m = 5.5 \pm 0.9$ following a 6 second forepaw stimulation in rat. On extrapolating this result to the steady state they measured $\gamma_m = 2.8 \pm 0.7$, within the error of the value measured by Grubb.

$$f_{out}(v) = v^{\alpha+\beta} \tag{5.13}$$

This result shows that the Grubb relation is only valid in the steady state. During dynamic changes in flow Grubb's constant changes to reflect the current state of the compliance of the venous balloon. Therefore typical functional experiments cannot be accurately modelled and a dynamic model is required.

Buxton *et al.*

In Buxton *et al.* [47] it was noted that whilst the Grubb relation does predict the steady state relationship between flow and total blood volume, it fails to adequately model transitions between states. As a solution to this problem they proposed modelling f_{out} as the sum of a linear component and a power law [130].

$$f_{out}(v) = v^{1/\alpha} + \tau_{\pm}\frac{dv}{dt} \tag{5.14}$$

Viscoelastic effects in the venous balloon were modelled by making $f_{out}(v)$ a function of the rate of volume change. At the onset of activation the balloon will resist a change in volume, but eventually a new steady state will be realised. For non-zero values of $\tau_{\pm}$ the flow-volume curve of the balloon will experience hysteresis. As a further generalisation of the model the value of

$\tau_{\pm}$ was allowed to vary on inflation (+) and deflation (−), allowing greater fine tuning when fitting this model to data.

Kong *et al.*

The modified windkessel model with compliance was described by Kong *et al.* [131]. It is an enhancement of the earlier windkessel model produced by Mandeville *et al.* [68].

$$f_{out}(v,t) = \frac{v^{\alpha+\beta}}{A(t)} \tag{5.15}$$

The function $A(t)$ is exponential and is adjusted when fitting to experimental data in order to control the vascular compliance. Kong *et al.* sought to generalise equation 5.15 by introducing an additional state variable, the normalised delayed compliance, $c(t)$.

$$\frac{dc(t)}{dt} = \frac{1}{\tau_c}\big(v^{\beta} - c(t)\big) \tag{5.16}$$

By substituting $c(t)$ for $A(t)$ in equation 5.15 they derived a new form for f_{out}.

$$f_{out}(v,t) = \frac{v(t)^{\alpha+\beta}}{c(t)} \tag{5.17}$$

During changes in blood volume $c \to 1$ and $f_{out} \to v^{\alpha+\beta}$ whereas at steady state $c = e^{\beta}$ and $f_{out} = v^{\alpha}$. Therefore at steady state equation 5.17 reduces to Grubb's relation.

5.2.3 Oxygen Extraction Models

An integral part of a Balloon model simulation is the determination of the oxygenation of the venous blood. The majority of the BOLD signal is derived from the change in oxygenation of venous blood. The BOLD signal model [106] discussed later in this section estimates that the ratio of signal derived from oxygenation change versus volume change is 3.4 : 1 at 1.5 T.

Three models of oxygen extraction from the blood were investigated. The first model [130] was empirical in nature and assumed that blood flow and

oxygen metabolism can be linearly related. The second model [57] described the vasculature by a two-compartment model and provides a greater understanding of the underlying mechanism. This model, known as the oxygen limitation model, explains the large increase in blood flow which accompanies small changes in oxidative metabolism. This explanation is both intuitive and maintains linearity between blood flow and oxidative metabolism. The third model [132] compensates for deficiencies in the oxygen limitation model such as its invalidity during dynamic changes in flow and metabolism. All three models are described in greater detail in the following sections.

Empirical Model

Despite the simplicity of this model it was the most recently proposed of the three models in this section. Buxton *et al.* [130] state that this model was based on the experimental observation that during modest increases in activity, CBF increases linearly with $CMRO_2$ [133]. At steady state $CMRO_2$ is related to CBF ($F_{in}(t)$) by equation 5.3. In this work these variables were normalised to their resting values, giving equation 5.18. In this expression m is the normalised $CMRO_2$ and the arterial oxygenation fraction, C_a, is assumed to be unity.

$$m = \frac{E}{E_0} f_{in} \tag{5.18}$$

Given the linearity assumption above, the empirical model described the relationship between changes in CBF and $CMRO_2$ by a constant n. Equation 5.20 is quoted in normalised units.

$$n = \frac{\Delta CBF / CBF_0}{\Delta CMRO_2 / CMRO_{20}} \tag{5.19}$$

$$n = \frac{f_{in} - 1}{m - 1} \tag{5.20}$$

Buxton *et al.* referenced experimental studies [133–137] that suggested that $n = 2 - 3$. They note that the fact that $n > 1$ suggests that the oxygen extraction fraction decreases with increasing flow. This is a central principle of the oxygen limitation model described below.

Oxygen Limitation Model

The oxygen limitation model was motivated by the observation [55] that during neuronal activation blood flow and the metabolic rate of glucose consumption rose by 30-50 %, whereas oxygen consumption only rose by 5 %. This seemed to suggest that blood flow and oxygen metabolism were decoupled, at least during dynamic changes in activity. This goes against conventional philosophy that these quantities are tightly coupled. Buxton and Frank sought to prove that the observations could still be explained by tight coupling of flow and oxygen metabolism. Their argument is based on four assumptions;

1. At rest all capillaries are perfused. There is no capillary recruitment.
2. Oxygen metabolism is efficient. All oxygen entering tissue is metabolised.
3. Exchange of O_2 between plasma and erythrocytes is very rapid.
4. Each O_2 molecule in the capillary has a probability per unit time of being extracted.

The transport of oxygen to the tissue was described as an oxygen concentration gradient between the capillary and tissue mitochondria. During activity the mitochondrial oxygen demand increases and in order to supply this demand the concentration gradient must also increase. They state that this can be achieved in one of two ways; capillary recruitment or increased blood velocity. They describe capillary recruitment as the ability of the vasculature to open up previously non-perfused capillaries. By recruiting capillaries the oxygen source can be brought closer to the mitochondria and hence the gradient can be increased. However they argue that this mechanism does not exist, and the only way to increase the concentration gradient is by increasing capillary oxygenation. The only other way to increase capillary oxygen concentration is by increasing blood flow. As the change in capillary volume on activation is assumed to be negligible this is manifested as an increase

in blood velocity. Therefore the transit time of an oxygen molecule through the capillary will be reduced and so by assumption 4 the probability of it being extracted will also be reduced. This led to the observation that in order to satisfy a small increase in oxygen metabolism a large increase in flow was required. Buxton and Frank formalised these arguments to produce a mathematical model of oxygen transport under the oxygen limitation model.

An element of blood with oxygen concentration, C_B, moving along the capillary loses oxygen as a function of the plasma oxygen concentration, C_p, and the probability of extraction, k.

$$\frac{dC_B(t)}{dt} = -kC_p(t) \tag{5.21}$$

Equation 5.21 follows assumption 2 and therefore tissue oxygen concentration was assumed to be zero.

The oxygen extraction at time t was described as the change in the capillary blood oxygen concentration relative to time $t = 0$. Time $t = 0$ represents the point at which arterial blood flows into the capillary and time t the time at which blood leaves the capillary to pass into the veins.

$$E(t) = \frac{C_B(0) - C_B(t)}{C_B(0)} \tag{5.22}$$

The oxygen extraction fraction was dependent on the average transit time of an oxygen molecule through the capillary. Assuming that the ratio, $r = C_p/C_B$, was constant and that all capillaries had the same mean transit time, $\tau_{MTT} = V/F$ (from the central volume principle).

$$E = 1 - e^{-k\,r\,\tau_{MTT}} \tag{5.23}$$

Equation 5.23 was then solved for the active and rest conditions of oxygen extraction and flow i.e. at rest $E = E_0$ and $F = F_0$. The variables k, r, and V remained the same during both conditions leading to the oxygen extraction fraction being a function of blood flow, f_{in}.

$$E = 1 - (1 - E_0)^{1/f_{in}} \tag{5.24}$$

Oxygen Transport to Tissue

The Oxygen Transport to Tissue (OTT) model of Zheng *et al.* [132] sought to improve upon the work of Buxton and Frank [57] in several important areas. These areas included the incorporation of a tissue oxygen buffer, implementation of a dynamic model of oxygen extraction and the establishment of a link between tissue oxygenation and metabolic demand. The results of their work are discussed below, without mathematical proof.

The introduction of a tissue oxygen buffer removed assumption 2 of the oxygen limitation model. This was achieved by adding a second compartment to equation 5.21 and allowing exchange between these compartments,

$$\frac{dC_B(x,t)}{dt} = -k(C_p(x,t) - C_t(t)) \tag{5.25}$$

where C_t represents the tissue oxygen concentration. The solution of this equation allowed the blood oxygen concentration, at any point along the capillary, to be derived,

$$C_B = \left(C_B^a - \frac{C_t}{r}\right) e^{Akrx/F_{in}} + \frac{C_t}{r} \tag{5.26}$$

where C_B^a represents the arterial blood oxygen concentration, A the capillary cross-sectional area, and x the distance along the capillary, where $x = 0$ is the beginning of the capillary bed. In turn this equation can be used to calculate the oxygen extraction fraction for a system in a steady state.

$$E = 1 - \frac{C_B^v}{C_B^a} = (1-g)\left[1 - \left(1 - \frac{E_0}{1-g_0}\right)^{1/f_{in}}\right] \tag{5.27}$$

The variable g was introduced to represent the tissue oxygen buffer and was defined as the ratio of the arterial plasma and tissue oxygen concentrations.

$$g = \frac{C_t}{C_p^a} \qquad 0 < g < 1 - E \tag{5.28}$$

However this relation does not hold during dynamic changes in blood flow. Changes in flow cause the spatial profile of the blood oxygen concentration

to vary with time. If the capillary transit time was zero then changes in oxygenation would be instantaneous, but unrealistic. Therefore Zheng *et al.* attempted to describe the temporal change in blood oxygen concentration, at a given location along the capillary, by a first order differential equation. This equation was based on the steady state relation and an additional dynamic component controlled by a time constant, τ. As τ was related to the capillary transit time it was redefined as a function of blood flow, to account for a reduced transit time at increased blood flow levels,

$$\tau = \frac{\varphi}{f_{in}} \tag{5.29}$$

where φ is a characteristic time constant of the system. For non-zero tissue oxygenation the blood oxygen concentration at a point L is given as,

$$\frac{\varphi}{f_{in}}\frac{\partial C_B}{\partial t} + C_B = C_B^a(1-g)\left(1 - \frac{E_0}{1-g_0}\right)^{x/f_{in}L} + C_B^a g \tag{5.30}$$

and in turn the oxygen extraction fraction is given by,

$$\frac{\varphi}{f_{in}}\frac{\partial E}{\partial t} + E = (1-g)\left(1 - \left(1 - \frac{E_0}{1-g_0}\right)^{1/f_{in}}\right) \tag{5.31}$$

Finally in order to solve for g, Zheng *et al.* produced a model to link tissue oxygen concentration to metabolic demand. They defined the rate at which oxygen accumulates in the tissue to be a mismatch between the rate at which oxygen leaves the capillary ($CMRO_2$) and the rate at which it is metabolised (M).

$$V_{tis}\frac{dC_t}{dt} = CMRO_2 - M \tag{5.32}$$

The variable V_{tis} represents the volume of blood in the tissue. Models of $CMRO_2$ and M were substituted into equation 5.32 to produce,

$$J\frac{V_{tis}rT}{V_{cap}E_0}\frac{dg}{dt} = \left(\frac{\bar{C}_B - gC_B^a}{\bar{C}_{B0} - g_0C_B^a} - 1\right) - Ku \tag{5.33}$$

where J and K represent scaling constants, V_{cap} the capillary blood volume and $\bar{C}_B$ the mean blood oxygen concentration, defined by equation 5.34.

$$\frac{\phi}{f_{in}}\frac{d\bar{C}_B}{dt} + \bar{C}_B = -\frac{C_B^a E}{ln\left(1 - \frac{E}{1-g}\right)} + C_B^a g \tag{5.34}$$

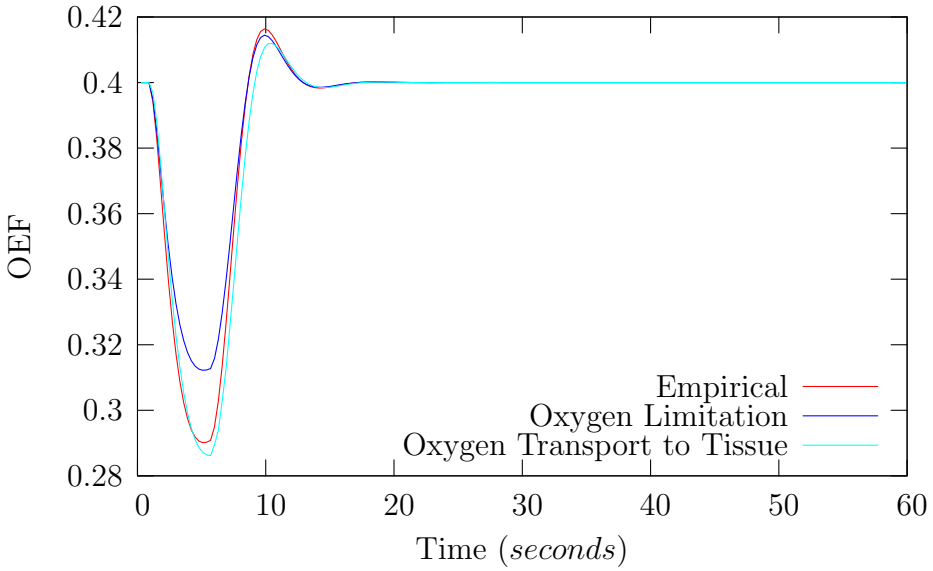

Figure 5.5: Comparison of models of oxygen extraction.

Equations 5.31, 5.33 and 5.34 form the basic equations of the OTT model. They are integrated into the Balloon model, along with the flow model of Friston *et al.* in the implementation of Zheng *et al.*.

Whilst this model is very complex it does not produce dramatically different results to the previous models, see figure 5.5. However it does have several advantages. Firstly it makes it possible to model experiments where hypercapnia is induced in subjects [133]. The metabolic load can be retained at a consistent level, whilst the effect of increased blood flow on oxygen extraction can be simulated. Secondly the OTT model makes it possible to investigate metabolic loads that are de-coupled from neural activity. This would allow the possibility of post-stimulus metabolic activity to be simulated within the framework of an integrated model such as this.

5.2.4 BOLD signal model

The solution of the Balloon model equations 5.4 and 5.5 produces timecourses of deoxyhaemoglobin content, q, and volume, v. In order to relate these

quantities to an approximation of the measured BOLD signal a model of the MR signal is required. A simple and flexible model was proposed by Buxton *et al.* [47] whereby changes in signal brought about by changes in q and v can be calculated. This model was revised and updated by Obata *et al.* [106] and is presented below.

In the work of Obata *et al.* the signal at rest, S_0, resulting from an imaging voxel was assumed to be a volume weighted sum of the intravascular, S_I, and extravascular, S_E, signal. The intravascular signal was assumed to represent a venous volume fraction V_0, for which blood vessels were assumed to be randomly and isotropically distributed. The intravascular contribution due to arterial blood was assumed to be negligible, and the capillary component was merged into the venous compartment. The signal components were modelled as a monoexponential decay dependent on R_2^*, where ϵ_s represents the intrinsic ratio of blood to tissue signal.

$$S_0 = (1 - V_0)S_E + V_0 S_I \tag{5.35}$$

$$S_E = S_{E0} e^{-TER_{2E}^*} \tag{5.36}$$

$$S_I = S_{I0} e^{-TER_{2I}^*} \tag{5.37}$$

$$\epsilon_s = \frac{S_I}{S_E} \tag{5.38}$$

During neural activity the R_2^* of both signal components was increased by an amount ΔR_2^* due to the change in oxygenation, and the venous volume fraction changed from V_0 to V. On activation the signal was given by,

$$S = (1 - V)S_E e^{-TE\Delta R_{2E}^*} + V S_I e^{-TE\Delta R_{2I}^*} \tag{5.39}$$

The fractional signal change was then found from equations 5.35, 5.38 and 5.39,

$$\frac{\Delta S}{S_0} = \frac{1}{1 - V_0 + \epsilon_s V_0}\Big[(1 - V)e^{-TE\Delta R_{2E}^*} + \epsilon_s V e^{-TE\Delta R_{2I}^*} - (1 - V_0) - \epsilon_s V_0\Big] \tag{5.40}$$

This expression was then simplified further. Assuming that signal changes were small the exponent can be expanded as a first order linear approximation. Furthermore, by assuming a small fractional blood volume it was

also possible to equate the multiplicative factor to 1, yielding the following simplified expression.

$$\frac{\Delta S}{S_0} \approx -TE\Delta R^*_{2E} - \epsilon_s VTE\Delta R^*_{2I} + (V_0 - V)(1 - \epsilon_s) \tag{5.41}$$

Models of ΔR^*_{2E} and ΔR^*_{2I} were then described as follows.

Extravascular Signal Change

Obata *et al.* based their model of ΔR^*_{2E} on the numerical simulations of Ogawa *et al.* [84].

$$R^*_2 = 4.3\nu V \tag{5.42}$$

The frequency offset at the outer surface of the magnetised vessel was described as $\nu = \nu_0(1 - Y)$, where ν_0 represents the frequency offset for fully deoxygenated blood and Y the fractional oxygen saturation of the blood. Therefore the transverse relaxation of the extravascular space was described as,

$$R^*_2 = 4.3\nu_0 V(1 - Y) \tag{5.43}$$

and relative to the resting state (subscript 0) it was found that,

$$\Delta R^*_{2E} = 4.3\nu_0[V(1 - Y) - V_0(1 - Y_0)] \tag{5.44}$$

With the knowledge that the total deoxyhaemoglobin content was described by $Q = V(1-Y)[Hb]$, Obata *et al.* derived the normalised deoxyhaemoglobin content, q.

$$q = \frac{Q}{Q_0} = \frac{V(1 - Y)}{V_0(1 - Y_0)} \tag{5.45}$$

By combining equations 5.44 and 5.45, along with the resting oxygen extraction fraction $E_0 = 1 - Y_0$, ΔR^*_{2E} became a function of q.

$$\Delta R^*_{2E} = 4.3\nu_0 V_0 E_0(q - 1) \tag{5.46}$$

Intravascular Signal Change

The intravascular signal change was modelled with reference to the experiments of Li *et al.* [86]. This work involved the *in vivo* measurement of the relationship between R_2^* and blood oxygen saturation. As expected this relationship was best approximated by a second-order curve fit. However it was suggested that for the normal physiological range of oxygenation a linear fit was adequate,

$$R_2^* = r_d(1 - Y) \tag{5.47}$$

where r_d represents the relaxivity of deoxyhaemoglobin and Y the fractional oxygen saturation. This was confirmed by the experiments of chapter 3, as shown in figure 3.5. At 3.0 T r_d was measured to be $16.9 \pm 2.2 \times 10^{-2}$ ms^{-1}. Consequently the change in R_2^* was,

$$\Delta R_{2I}^* = r_d\big[(1 - Y) - (1 - Y_0)\big] \tag{5.48}$$

This was rearranged in terms of the normalised deoxyhaemoglobin content and volume.

$$\frac{q}{v} = \frac{Q}{Q_0}\frac{V_0}{V} = \frac{1 - Y}{1 - Y_0} \tag{5.49}$$

To give the expression,

$$\Delta R_{2I}^* = r_d E_0\Big(\frac{q}{v} - 1\Big) \tag{5.50}$$

Fractional Signal Change

Equations 5.46 and 5.50 were combined with equation 5.41.

$$\begin{aligned}
\frac{\Delta S}{S_0} &= -4.3\nu_0 V_0 E_0 TE(q - 1) - \epsilon_s V r_d E_0 TE\Big(\frac{q}{v} - 1\Big) + (1 - \epsilon_s)(V_0 - V) \\
&= V_0\Big[k_1(1 - q) - k_2 v\Big(\frac{q}{v} - 1\Big) - k_3(1 - v)\Big] \\
&= V_0\Big[(k_1 + k_2)(1 - q) - (k_2 + k_3)(1 - v)\Big]
\end{aligned} \tag{5.51}$$

The constants k_1 to k_3 were defined as,

$$k_1 = 4.3\nu_0 E_0 TE \quad (5.52)$$

$$k_2 = \epsilon_s r_d E_0 TE \quad (5.53)$$

$$k_3 = \epsilon_s - 1 \quad (5.54)$$

5.3 Method

Two BOLD models were formed from the theory components discussed in section 5.2. Each model was described by a different number of parameters, allowing a comparison to be made between empirical (low number of parameters) and more sophisticated model elements. The composition of each model is described in section 5.3.1. Each model was fitted using a simulated annealing algorithm (section 5.3.4) to the experimental data of chapter 4 and the fitting process is described in section 5.3.2. In order to calculate the signal changes due to contrast agent in arterial vessels (typically neglected in conventional models) a multi-component signal model was derived (section 5.3.3) by generalising the equations of Obata *et al.* [106].

5.3.1 Models Studied

Two combinations of model components were chosen to reflect an empirical approach and a more sophisticated mechanistic approach. These approaches are most noticeable in the modelling of the flow input (section 5.2.1) to the system, f_{in}. The Miller model is dependent only on the duration of the stimulus as it was determined by fitting to experimental data. However, the Behzadi model is dependent on four parameters; neuronal efficacy (ϵ), signal decay (k_s), feedback gain, (g_f), and arteriolar radius (r_{max}). These extra parameters are required to describe the mechanism behind changes in CBF.

In choosing a model of flow output, f_{out}, the conventional hypothesis was adopted (section 5.2.2). This states that the post-stimulus undershoot can be described by a lag between flow into the system and the return to baseline of

Model No.	Flow Model	Volume Model	Oxygen Extraction	No. Parameters
1	Miller *et al.*	Buxton *et al.*	Empirical	3
2	Behzadi *et al.*	Buxton *et al.*	Empirical	7

Table 5.2: Components of models 1 and 2. For a detailed description of these components see section 5.2.

CBV. It was clear that a dynamic model of venous outflow was required. For simplicity the model of Buxton *et al.* was chosen. This model is dependent on two time constants describing the inflation (τ_+) and deflation (τ_-) of the venous balloon. However it can be shown that this model and the model of Kong *et al.* can simulate equivalent venous outflow curves, and are as such interchangeable for the purposes of this simulation. The model of Kong *et al.* does offer the possibility of a greater understanding of venous outflow, but was not investigated.

The selection of an oxygen extraction model (section 5.2.3) followed the hypothesis described above. As it is assumed that volume change alone can describe the post-stimulus undershoot, the simplest model of oxygen extraction was used. This Empirical model of oxygen extraction produces comparable results to the Oxygen Limitation and Oxygen Transport to Tissue models.

In summary, both models shared the same basic dynamic volume model of Buxton *et al.*, describing venous volume change, and the empirical oxygen extraction model, to describe changes in oxygenation. However differences between the models were achieved by using different forms for the arterial input function. In the case of model 1 this element was supplied by the empirical Miller *et al.* model. For model 2 the Arteriolar Compliance model described by Behzadi *et al.* was used. One final parameter was added to model the time delay (t_d) between the onset of stimulus and the haemodynamic response. Overall model 1 was described by 3 parameters and model 2 by 7 parameters.

5.3.2 Model Parameter Estimation

Each BOLD model combination was fitted to experimental data from chapter 4. This data consisted of a total CBV timecourse (figure 4.9) and a BOLD signal timecourse (figure 4.6a). A least squares fit was performed for each model to each data set to estimate the model parameters in each case. Parameters were constrained to the ranges described by Behzadi *et al.* [126] and are listed in table 5.3. In order to fit each model to the total CBV data a simulated timecourse was required. This was created by performing a volume weighted sum of the arterial and venous volume change. These variables are produced when the Balloon model equations are numerically solved. The weighting was based on an arterial:venous vessel volume ratio of 1:3 [111].

Simulation of the BOLD signal timecourse required a multi-component BOLD signal model to be developed, see section 5.3.3. In a conventional BOLD signal model changes in blood signal are assumed to occur in venous and capillary vessels due to changes in blood oxygenation, whilst arterial blood is fully oxygenated. The addition of contrast agent to the blood causes the blood signal to decrease and will affect all vessels, both arterial and venous. By adopting a multi-component model the arterial blood signal contribution can be determined in the absence of changes in oxygenation.

The BOLD signal data consisted of 20 cycles of a visual stimulus. The final 16 cycles were acquired during a 16 minute infusion of contrast agent. Preliminary fitting to this data caused the fitting algorithm to ignore the features of the BOLD haemodynamic response and concentrate on fitting the much larger baseline drift due to the infusion of the contrast agent. Therefore in the final fits the baseline drift was removed by linearly interpolating between the first and last data points of each cycle. In addition the results of fitting to the total CBV data revealed an overestimation in the simulated BOLD signal. In this case a vascular volume fraction of 4 % was used. However the vascular volume fraction, V_0, in equation 5.68 effectively represents the fraction of vessels involved in the haemodynamic response. All other vessels, remaining in the steady state, will not contribute to BOLD signal

change but will contribute to baseline drift due to the contrast agent. The BOLD signal data were acquired from a large region of interest encompassing a volume of $\sim$0.8 cm^3. Evidently there will be dilution of the BOLD signal due to the partial volume effect. Therefore an additional fitting parameter was added to vary the activated vessel volume fraction, giving a total parameter count of 4 and 8 for models 1 and 2, respectively.

Due to the large number of fitting parameters, and the generous constraints, it was possible that local minima could exist in the fitting space. This problem was exacerbated by the noise present in the data. In order to investigate this effect, models 1 and 2 were fitted to the total CBV timecourse. A non-optimised simulated annealing (SA) algorithm was used, allowing the final solution to be independent of initial starting position. Assuming that local minima were present in the data, the solutions produced by a descent based algorithm would be highly dependent on starting position. Multiple random starting positions could have been selected, but many low significance local minima would have been found. The SA technique bypasses these minima and only selects minima of high significance. An optimised SA algorithm will theoretically find a single global minimum. By *de-tuning* the algorithm it was possible to discover multiple local minima. Whilst these minima were spread over a range of sum of square residual values, this range was narrow. This allowed the distribution of these minima to be investigated and the possibility of a single global minima assessed. De-tuning the SA algorithm was achieved by choosing a sub-optimal cooling schedule, see section 5.3.4 for further details. A total of 100 least squared SA fits were performed for each model.

Figure 5.6 plots τ_+ versus τ_- for each of 100 parameter estimations. For model 1 (figure 5.6a) it is clear that a single minima is possible as the values of τ_+ and τ_- are very tightly clustered. However for model 2 (figure 5.6b) the values show a great deal of scatter and suggest that there may well be multiple local minima. Figure 5.7 shows the value of τ_+ against the sum of the squared residuals generated for that estimation. Again in model 1

Parameter	Variable	Constraint
Inflation Time Constant	τ_+	$0 - 30$
Deflation Time Constant	τ_-	$0 - 30$
Neuronal Efficacy	ϵ	$0 - 1$
Signal Decay Constant	k_s	$0 - 2$
Flow Feedback Gain	g_f	$0 - 2$
Max. Normalised Radius	r_{max}	$1.2 - 1.3$
Time Delay	t_d	$0 - 5$

Table 5.3: Parameter constraints used in least squares fit to data [126].

(figure 5.7a) this result suggests that the data can be described by a single global minima within certain error bounds determined by the noise in the data. For model 2 (figure 5.7b), however, there appear to be many local minima which could describe the data. Determining which minima is the global minima is complicated by the noise incorporated in the data.

The theoretical minimum sum of squared residuals value can be calculated using a Monte Carlo technique. A model curve solution was randomly chosen and subtracted from the experimental data to assess the level of noise. The noise was assumed to be Gaussian in nature and its mean and standard deviation was calculated. It was then assumed that the original model curve described the data perfectly. Random Gaussian noise, with the same distribution as that calculated from the data, was then added to the model curve. The sum of square residuals was calculated and this process repeated 100 times. This allowed a mean and standard deviation of 0.35 and 0.04, respectively, to be calculated. There are many distinct solutions to model 2 which surpass this threshold. Determining which solution is the global minimum is extremely difficult. It is not even meaningful to quote the mean and standard error of the parameter estimates as this average is unlikely to fall within a minima itself. It is still possible, however, to assess the form and variation of the curve solutions. In figure 5.8 the variation in the solutions is visualised by plotting all 100 solutions.

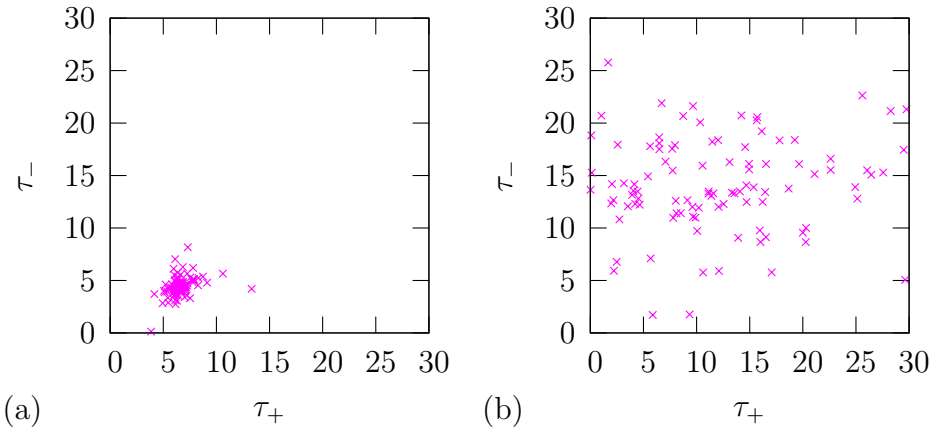

Figure 5.6: Model parameter solution: τ_+ versus τ_- for (a) model 1 and (b) model 2.

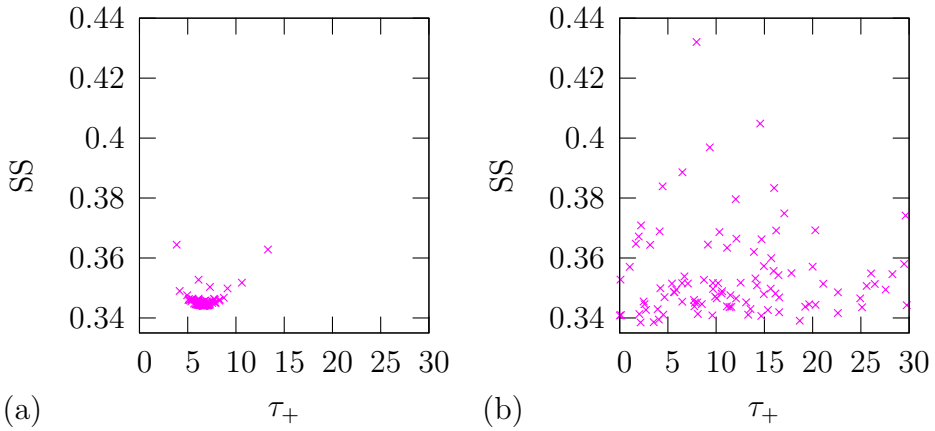

Figure 5.7: Model parameter solution: τ_+ versus the sum of the squared residuals for (a) model 1 and (b) model 2.

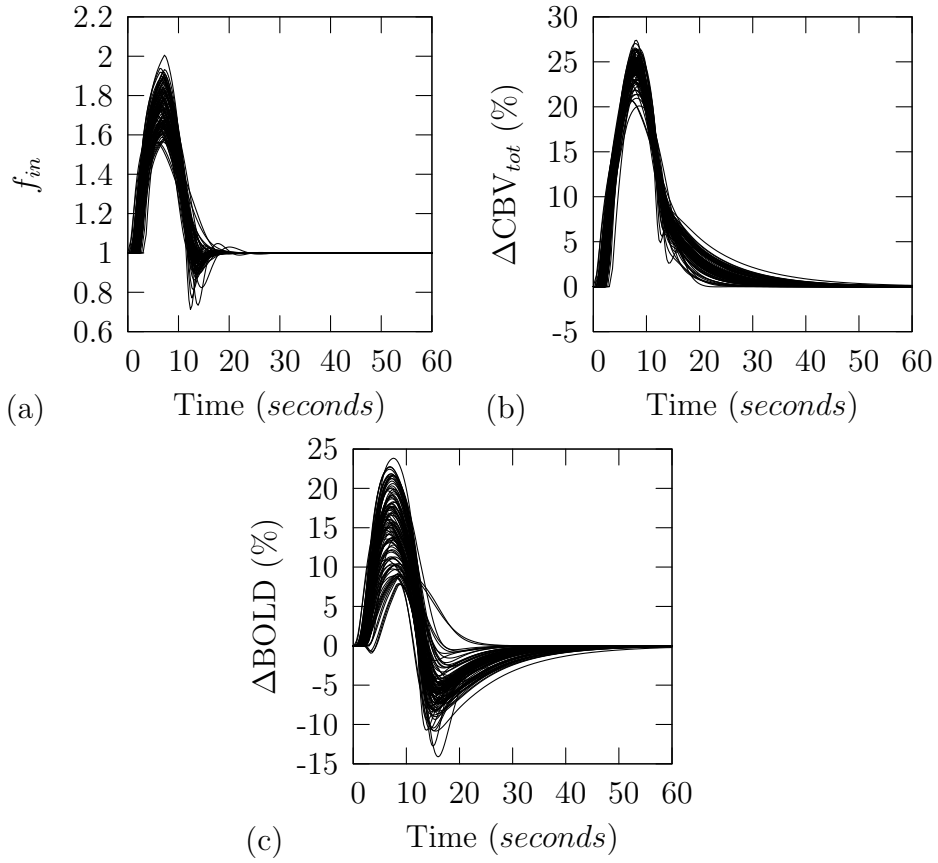

Figure 5.8: Model parameter solutions: 100 solutions of model 2 for variables f_{in}, v_{tot} and simulated BOLD signal change. BOLD signal change calculated using the multi-component signal model.

As a final check of the independence of the minima determined in figure 5.6 a Monte Carlo error estimation technique was used to calculate the error in the parameter estimation of 5 randomly selected solutions, with mean sum of squares 0.35 and standard deviation 0.01. Initially each of the solutions were subjected to a constrained descent based minimisation algorithm in order to find the absolute minimum for each solution. It was assumed that each model curve described the data perfectly and that the residuals represent additive Gaussian noise. The mean and standard deviation of this noise was calculated. Gaussian noise with the same characteristics was added

to the model curve and a constrained least squares optimisation performed. This process was repeated 100 times to sample the range of possible solutions given the noise in the data. The parameter estimates generated were used to calculate mean values along with an error estimate and are summarised in table 5.4. It is clear from these results that each of the solutions show very little overlap, and as such represent distinct local minima.

	1	2	3	4	5
τ_+	21.13 ± 0.02	8.48 ± 0.13	13.11 ± 0.04	14.09 ± 0.04	5.82 ± 0.11
τ_-	15.19 ± 0.02	11.57 ± 0.12	16.27 ± 0.04	14.75 ± 0.04	12.81 ± 0.10
ϵ	0.49 ± 0.01	0.77 ± 0.01	0.43 ± 0.01	0.36 ± 0.01	0.74 ± 0.01
k_s	1.00 ± 0.01	1.61 ± 0.01	0.99 ± 0.01	0.80 ± 0.01	1.61 ± 0.02
g_f	0.43 ± 0.01	0.82 ± 0.01	0.42 ± 0.01	0.38 ± 0.01	0.83 ± 0.01
r_{max}	1.247 ± 0.001	1.229 ± 0.001	1.253 ± 0.001	1.242 ± 0.001	1.218 ± 0.001
t_d	1.77 ± 0.02	2.39 ± 0.03	1.93 ± 0.02	1.80 ± 0.02	1.94 ± 0.03

Table 5.4: Calculated error in parameter estimations of model 2 using the bootstrap technique. Five solutions chosen randomly from total of 100 solutions.

5.3.3 Multi-Component Signal Model

It was noted in section 5.2 that the Balloon model effectively assumes all changes in volume and susceptibility occur in venous vessels. However when modelling an infusion of contrast agent, as performed in chapter 4, the arterial susceptibility resulting from the infusion must also be considered. Therefore a multi-component signal model based on the methodology of Obata *et al.* [106] was developed. In this model it is assumed that the cerebral vasculature can be partitioned into two components: arterial and venous. The capillary blood volume is shared between these compartments as it is assumed to have mixed oxygenation levels and constant volume. The intravascular signal components of each compartment are modelled as separate monoexponential decays. However the extravascular signal is summed over the effect of both compartments, as they both effect the same tissue volume. In this model the reference signal, S_0, is redefined as the signal at time $t = 0$, to reflect the condition that the system is at rest and the contrast agent concentration is zero. Equations 5.35 and 5.39 can be rewritten to reflect these assumptions and modifications,

$$S_0 = (1 - V_{a0} - V_{v0})S_E + V_{a0}S_{Ia} + V_{v0}S_{Iv} \tag{5.55}$$

$$S = (1 - V_a - V_v)S_E e^{-TE\Delta R^*_{2E}} + V_a S_{Ia} e^{-TE\Delta R^*_{2Ia}} + V_v S_{Iv} e^{-TE\Delta R^*_{2Iv}} \tag{5.56}$$

where subscripts a and v represent the arterial and venous compartments, respectively, and subscript 0 defines the value of a variable at time $t = 0$. In order to derive the fractional signal change the ratio of venous signal to arterial signal, β_s, at time $t = 0$ is introduced.

$$\epsilon_s = \frac{S_{Iv}}{S_E} \rightarrow S_{Iv} = \epsilon_s S_E \tag{5.57}$$

$$\beta_s = \frac{S_{Iv}}{S_{Ia}} \rightarrow S_{Ia} = \frac{S_{Iv}}{\beta_s} = \frac{\epsilon_s S_E}{\beta_s} \tag{5.58}$$

Using the same simplifying assumptions as described in section 5.2.4 produces the following expression.

$$\begin{aligned}\frac{\Delta S}{S_0} \approx & -TE\Delta R^*_{2E} - V_a\frac{\epsilon_s}{\beta_s}TE\Delta R^*_{2Ia} - V_v\epsilon_s TE\Delta R^*_{2Iv} \\ & +(V_{a0}-V_a)\Big(1-\frac{\epsilon_s}{\beta_s}\Big) + (V_{v0}-V_v)(1-\epsilon_s) \quad (5.59)\end{aligned}$$

This now leaves models of ΔR^*_{2E}, ΔR^*_{2Ia} and ΔR^*_{2Iv} to be defined in the presence of a contrast agent. In the context of this derivation, ΔR^*_2 represents a change in R^*_2 which is due to changes in contrast agent concentration and/or blood oxygenation.

Extravascular Signal Change

In this work the analytical solutions of Yablonskiy and Haacke [85] were used in the definition of ΔR^*_{2E},

$$R^*_2 = \frac{4\pi}{3}V\omega_0\chi \quad (5.60)$$

where R^*_2 is a function of the volume fraction, V, the Larmor frequency, ω_0, and the susceptibility relative to the surrounding medium, χ. It is possible to compare this expression with equation 5.42 used by Ogawa *et al.* [84]. The susceptibility of venous blood can be modelled [95] as $\chi_v = \chi_d(1-Y)$ and similarly from Ogawa *et al.* $\nu_v = \chi_d(1-Y)\omega_0$, where χ_d is the susceptibility of fully deoxygenated blood relative to tissue. Hence the only difference between the expressions is the multiplicative factor, which at $4\pi/3$ is within the errors of the numerical result calculated by Ogawa *et al.* of 4.3 ± 0.3.

In order to model the signal change the susceptibility at time t is considered with reference to the susceptibility at time $t = 0$. It is assumed that the susceptibility due to the contrast agent increases linearly with concentration, $[Gd]$, where χ_g is the molar susceptibility of the contrast agent.

$$\begin{aligned}\chi_0 &= (1-Y_0)\chi_d + [Gd]\chi_g \qquad \text{but at } t=0, [Gd]=0 \\ &= (1-Y_0)\chi_d \quad (5.61) \\ \chi &= (1-Y)\chi_d + [Gd]\chi_g \quad (5.62)\end{aligned}$$

By substituting equations 5.61 and 5.62 into equation 5.60, along with equation 5.45, the change in the extravascular R_2^* due to venous blood, with increasing contrast agent concentration, can be estimated.

$$\begin{aligned}\Delta R^*_{2Ev} &= \frac{4\pi}{3}\omega_0\Big[V_v(1-Y)\chi_d + V_v[Gd]\chi_g - V_{v0}(1-Y_0)\chi_d\Big] \\ &= \frac{4\pi}{3}\omega_0\Big[V_{v0}E_0(q-1)\chi_d + V_v[Gd]\chi_g\Big] \end{aligned} \tag{5.63}$$

Similarly the change in extravascular R_2^* due to arterial blood can be derived.

$$\Delta R^*_{2Ea} = \frac{4\pi}{3}\omega_0 V_v[Gd]\chi_g \tag{5.64}$$

A unified extravascular ΔR_2^* can then be realised by performing a volume weighted sum of equations 5.63 and 5.64.

$$\Delta R^*_{2E} = \frac{V_a}{V_a+V_v}\Delta R^*_{2Ea} + \frac{V_v}{V_a+V_v}\Delta R^*_{2Ev} \tag{5.65}$$

Intravascular Signal Change

For the purposes of this simulation it is assumed that the intravascular signal change due to the presence of a contrast agent increases R_2^* linearly with increasing concentration. By definition the concentration of contrast agent is zero at time $t = 0$ therefore,

$$\Delta R^*_{2Ia} = r_g[Gd] \tag{5.66}$$

where r_g is the relaxivity of contrast agent in blood. At 3.0 T r_g was measured, in chapter 3, to be $3.7 \pm 0.5 \times 10^{-2}$ $\mathrm{ms^{-1}mM^{-1}}$. Similarly the change in venous R_2^* can be modelled with reference to the derivation of equation 5.50,

$$\Delta R^*_{2Iv} = r_d E_0\Big(\frac{q}{v} - 1\Big) + r_g[Gd] \tag{5.67}$$

In fact a linear relationship may not always hold true, and an explanation of why this is the case can be found in chapter 3.

Fractional Signal Change

Equations 5.65, 5.66 and 5.67 can now be substituted into equation 5.59 to give,

$$\begin{aligned}
\frac{\Delta S}{S_0} &= -\frac{4\pi}{3}\omega_0 TE\frac{V_v}{V_a+V_v}V_{v0}E_0(q_v-1)\chi_d - \frac{4\pi}{3}\omega_0 TE\frac{V_v}{V_a+V_v}V_v[Gd]\chi_g \\
&\quad -\frac{4\pi}{3}\omega_0 TE\frac{V_a}{V_a+V_v}V_a[Gd]\chi_g - V_a\frac{\epsilon_s}{\beta_s}TEr_g[Gd] \\
&\quad -V_v\epsilon_s TEr_d E_0\Big(\frac{q}{v}-1\Big) - V_v\epsilon_s TEr_g[Gd] \\
&\quad +(V_{a0}-V_a)\Big(1-\frac{\epsilon_s}{\beta_s}\Big) + (V_{v0}-V_v)(1-\epsilon_s) \\
&= V_{v0}\Bigg[k_1\frac{V_v}{V_a+V_v}(1-q_v) - k_2 v_v\Big(\frac{q_v}{v_v}-1\Big) - k_3(1-v_v) \\
&\quad -k_4\frac{V_v}{V_a+V_v}v_v[Gd] - k_5 V_{v0}V_v[Gd]\Bigg] \\
&\quad +V_{a0}\Bigg[-k_4\frac{V_a}{V_a+V_v}v_a[Gd] - k_6 v_a[Gd] - k_7(1-v_a)\Bigg] \qquad (5.68)
\end{aligned}$$

Constants k_1 to k_5 are defined as,

$$\begin{aligned}
k_1 &= \frac{4\pi}{3}\omega_0 TEE_0\chi_d && (5.69)\\
k_2 &= \epsilon_s TEE_0 r_d && (5.70)\\
k_3 &= \epsilon_s - 1 && (5.71)\\
k_4 &= \frac{4\pi}{3}\omega_0 TE\chi_g && (5.72)\\
k_5 &= \epsilon_s TEr_g && (5.73)\\
k_6 &= \frac{\epsilon_s}{\beta_s}TEr_g && (5.74)\\
k_7 &= \frac{\epsilon_s}{\beta_s} - 1 && (5.75)
\end{aligned}$$

By assuming a singular vascular compartment, and that the concentration of contrast agent is zero, equation 5.68 reduces to equation 5.51. Therefore this model is a generalisation of the previously described model [106].

5.3.4 Simulated Annealing

The SA optimisation algorithm is analogous to the cooling of solids forming crystalline structures. Annealing is the process whereby a solid is first heated to a high temperature, below its melting point, and is then cooled slowly. At high temperatures the atoms within the solid are highly mobile, and hence can change their positions within the lattice structure. If the solid is cooled sufficiently slowly all of the atoms will find positions within the lattice structure with minimum energy. Alternatively if a solid is cooled rapidly mobility is quickly reduced and atoms will be trapped in positions that have energies greater than the minimum value. Hence conventional descent based algorithms are analogous to quench cooling a solid. By following a downward trend in the cost function these algorithms will find the nearest local minima, and are therefore dependent on starting conditions. However the SA technique is an approximation algorithm. It aims to find a good approximation to the global optima when a *brute force* approach is impractical or where it is likely that local minima may exist. Therefore a trade-off must be made between speed and accuracy.

In this section the SA algorithm will be described through a simple example. The Travelling Salesman Problem (TSP) is a computationally difficult question. The problem is stated as; given a number of cities, n, and the distance travelled between these cities, what is the most efficient route? When n is small this problem can be solved using the brute force method of calculating the total distance incurred by every permutation of city visits, $n!$. However as n increases the total number of permutations increases rapidly and solving the problem in this way becomes impractical. The SA technique proves to be particularly adept at solving this problem. Figure 5.9 schematically represents the SA algorithm. Initially n random city co-ordinates are generated and a cost function evaluated. In this case the cost function is the total journey length for the current order of visits, or state, s. The result of this cost function is commonly known as the current energy. The system is then perturbed in a random way to form state s'. For the TSP

this may occur by choosing two cities randomly and swapping their positions in the journey order. The cost function is then re-evaluated and acceptance testing of this new energy state performed. Acceptance testing consists of the following two step process. If the difference in energy, ΔE, between state s and state s' is less than zero, then the current state s is replaced by s'. However if ΔE is greater than zero, then the *Metropolis criteria* is applied. This probabilistic criteria allows the algorithm to escape local minima by permitting *up hill* steps in the cost function. Therefore states with positive ΔE are accepted using equation 5.76, where r is a random number between 0 and 1, k_B is Boltzmann's constant and T is the current temperature.

$$P = \begin{cases} 1 & \text{if } e^{-\Delta E/k_B T} > r \\ 0 & \text{otherwise} \end{cases} \tag{5.76}$$

This sequence is repeated many times for the current temperature in analogy to the thermal motion of atoms in a solid. In order for the parameter space to be adequately sampled at this temperature, a system for deciding when *thermal equilibrium* is achieved is required. For this simple case this was empirically determined to be a number of iterations. However there are more sophisticated alternatives.

At thermal equilibrium the temperature is decremented subject to a *cooling schedule*. Again this can be achieved in many ways, but the simplest is to multiply the current temperature by a cooling factor, α.

$$T_{new} = \alpha T_{current} \tag{5.77}$$

Finally a *freezing point* must be determined. Due to the exponential nature of the cooling schedule $T = 0$ will take an infinitely long time to achieve. Therefore the algorithm must be terminated after a certain number of iterations or when a temperature threshold is passed. The former method is used in this simple example.

In order to compare simulated annealing versus the brute force technique a TSP validation experiment was performed. Twenty co-ordinates in the $x - y$ plane were uniformly distributed along the circumference of a circle.

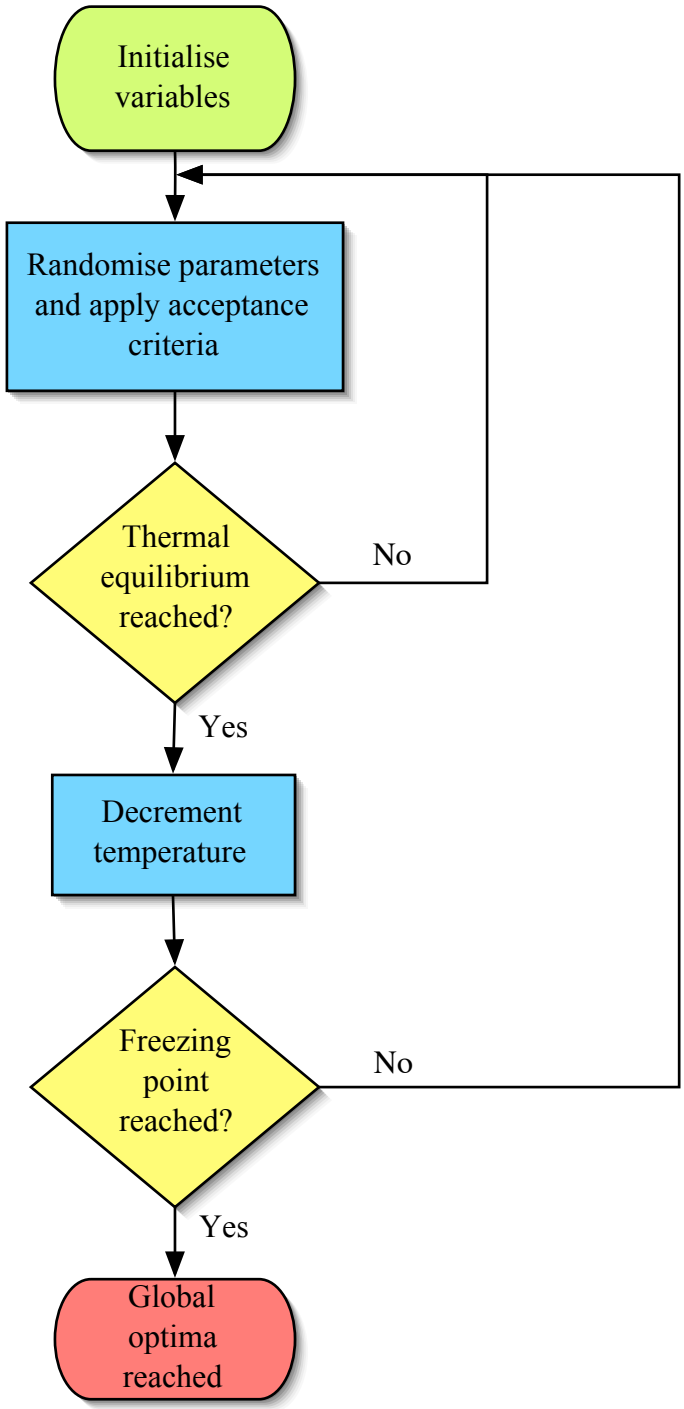

Figure 5.9: A schematic representation of the SA algorithm.

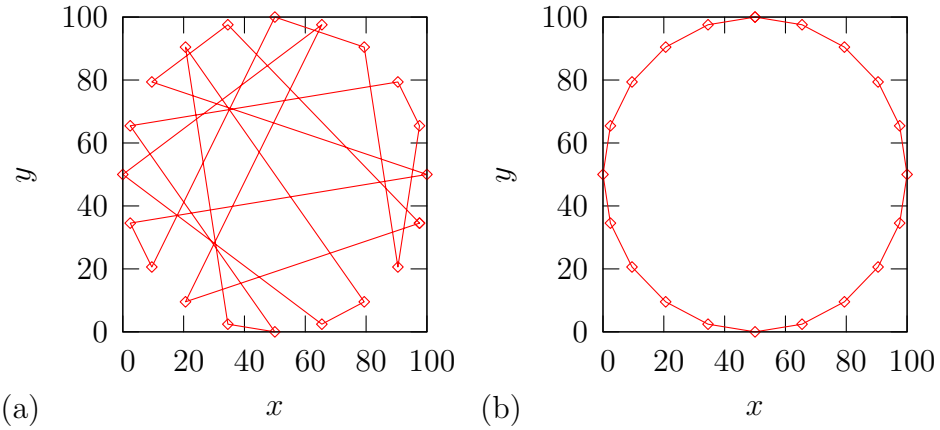

Figure 5.10: Validation of the SA algorithm for a simple example. Twenty co-ordinates are randomly distributed on the circumference of a circle (a) and subjected to an SA optimisation (b) to find the shortest route between all the points.

The resultant co-ordinates were placed in a random order and subjected to an SA optimisation. Optimisation was performed on an Apple PowerBook with a 1 Ghz PowerPC G4 processor and 512 Mb of RAM using MATLAB. The SA optimisation took approximately 5 minutes to reach the expected minima, see figure 5.10. The brute force technique could not be simulated, so an estimated processing time was calculated. A co-ordinate count of 20 requires over 2.4×10^{18} evaluations of the cost function. By running the cost function 100,000 times it was found that on average each evaluation takes 111.5 μs, giving a total run time of 8.6×10^6 years. This figure does not include the time to calculate all of the order permutations, which would add considerably to the total. It is obvious that despite the relatively crude algorithm described above, the SA technique is significantly faster than the brute force technique. This technique is also less susceptible to problems with multiple local minima.

In order to optimise models 1 and 2, described in section 5.3.1, a similarly crude implementation of the algorithm was used. Initially each model para-

meter was set to lie at the centre of the constraint range, see table 5.3. The model was then solved for the current state, and a cost function evaluated. The cost function, in this case, was the sum of squared residuals between the experimental and simulated curves. Perturbation of the solution was achieved by selecting one parameter and adding a random number. The random number was scaled to the full range of the constraint, was proportional to temperature and was uniformly distributed. This new parameter value was then tested for compliance with the constraint. If the new value was rejected then an alternative value was generated. The acceptance criteria used in the TSP example are then applied. The initial temperature was chosen as 2000, thermal equilibrium was determined to have occurred following 100 randomisation iterations and the freezing point was selected to be 5. These values were selected with the aim of trading-off speed and accuracy, as the aim of this investigation was not to find the absolute global minima, but to assess the likelihood of their presence.

5.4 Results

As was noted in section 5.3.2, mutiple minima are present in higher dimensional fits to the total CBV data from chapter 4. A similar pattern was found whilst fitting the signal data. Therefore all time course data in this section have been plotted in a similar manner to figure 5.8. As noted the mean values of the estimated parameters cannot be quoted, as simulations based upon these values are unlikely to fit the experimental data.

The following sections describe the results of fitting to both the total CBV and BOLD signal data gathered in chapter 4.

5.4.1 Volume Fitting Results

Figure 5.11 shows the results of fitting models 1 and 2 to the total CBV data from chapter 4. Both models show good correlation with the data and have mean sum of squared residuals of 0.346 and 0.354, for models 1 and 2 respect-

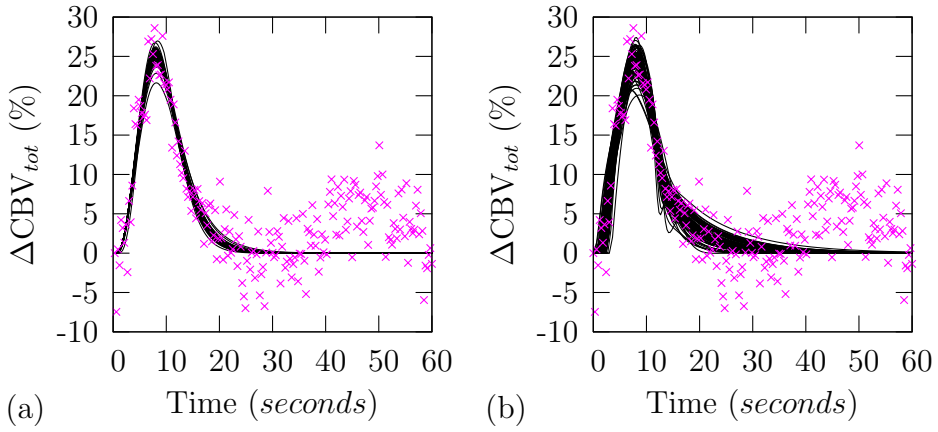

Figure 5.11: Model total CBV (ΔCBV_{tot}) curves from fit to experimental CBV data for (a) model 1 and (b) model 2. Experimental data points are plotted as crosses along with all 100 curve solutions.

ively. The standard deviation of the respective sum of squared residuals was 0.003 and 0.015, respectively. Due to the higher number of dimensions used in the fitting of model 2, there are a greater range of solutions. However during the period between 15 and 25 s model 2 appears to provide a solution giving a better fit to the change of slope, evident in the experimental data. This feature may be created in the summation of arterial and venous volume change, which creates the total CBV change. Arterial volume change is closely linked to changes in CBF. In turn venous volume change is dependent on CBF (f_{in}), but with a longer timescale due to smoothing introduced by viscoelastic effects in the venous balloon. By allowing more flexibility in the form of f_{in}, model 2 is capable of describing temporal dynamics of total CBV change that the rigid flow model of model 1 cannot. The feature present in the data beyond 35 s cannot be simulated by either model. This feature is an artefact of the button-press paradigm used to retain the attention of the subject and as such is not accounted for in either model.

Figure 5.12 plots the model variables simulated using models 1 and 2 for the model fits to the experimental CBV data. The variability across curve

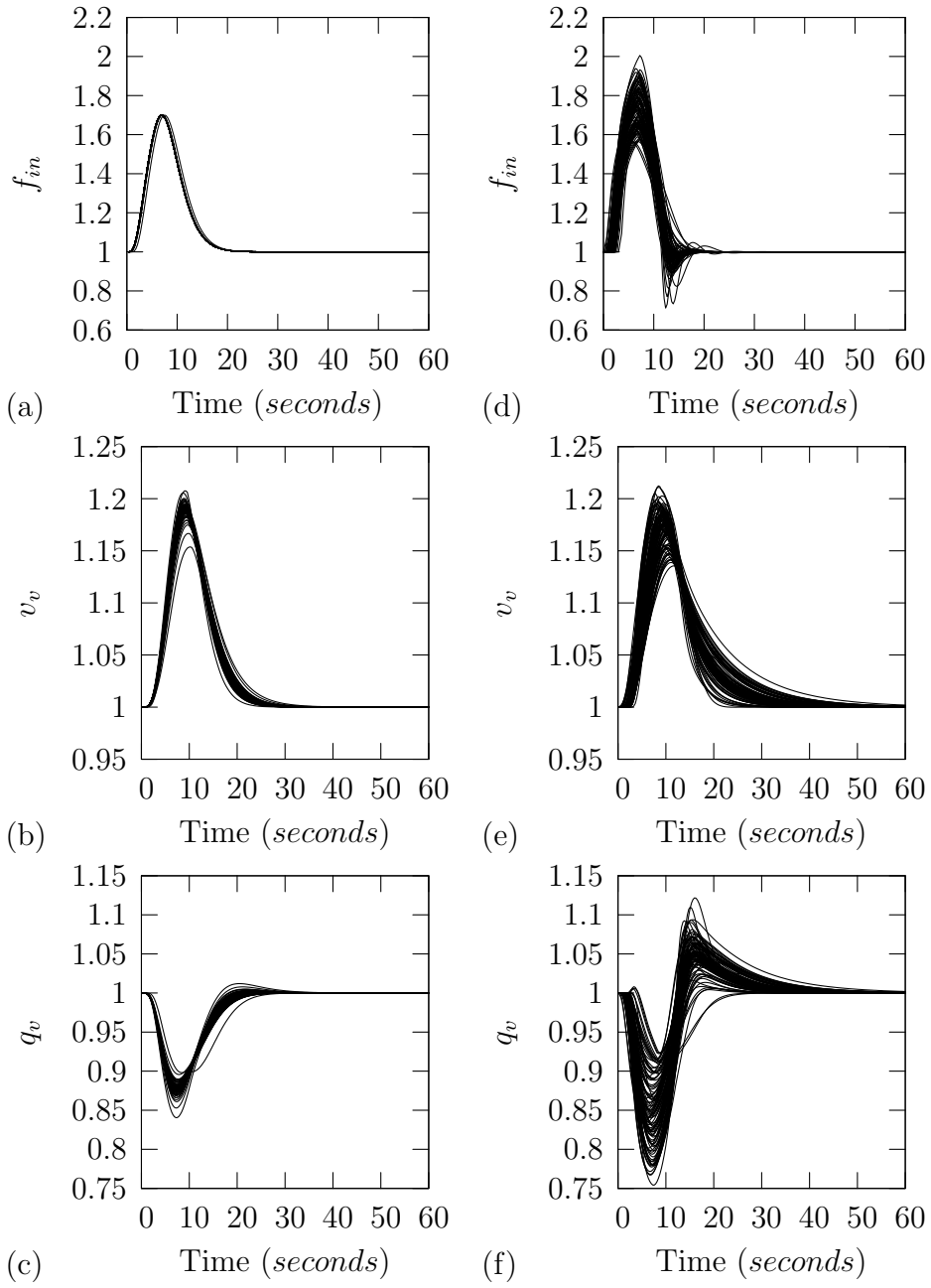

Figure 5.12: Model variable curves from fit to experimental CBV data for (a-c) model 1 and (d-f) model 2. Simulated variables include arterial flow input to the system, f_{in}, venous outflow, v_v, and venous deoxyhaemoglobin content, q_v. Data consists of 100 curve solutions to ΔCBV data.

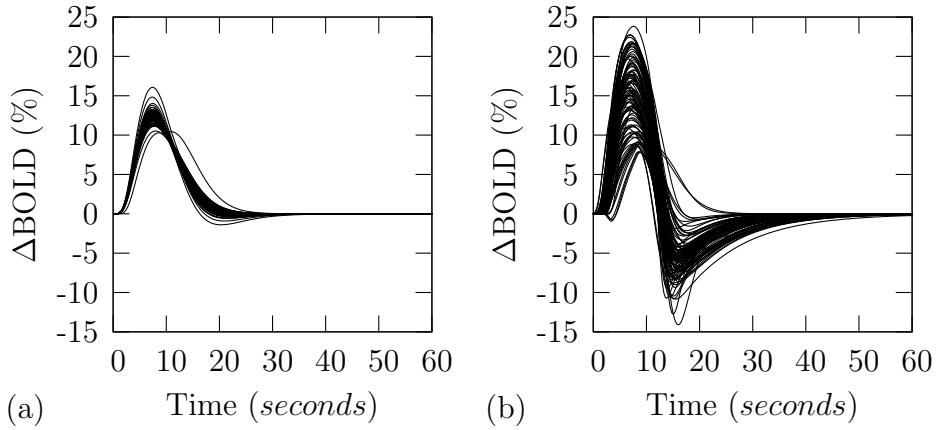

Figure 5.13: Simulated BOLD response using model variables and the multi-component signal model ($[Gd] = 0$). All 100 curve solutions plotted.

solutions for the model 2 variables is much greater than that present in the model 1 variables. As can be seen in figure 5.13, variation in the underlying model variables causes increased variability in the BOLD signal calculation.

The simulation predictions for an infusion of contrast agent could now be compared using the following method.

1. Remove baseline drift due to the contrast agent infusion.
2. Group the 20 cycles into 5 blocks of 4 continuous stimulus cycles, with mean $[Gd] = 0$, 0.11, 0.35, 0.53 and 0.70 mM.
3. Average across the stimulus cycles in each block
4. Overlay each of the 5 averaged blocks

In order to improve the visualisation of this figure all 100 curve solutions were averaged to produce a representative solution. In both cases the amplitude of the predictions was larger than seen experimentally. This is most likely due to unknowns such as the vascular volume fraction and the partial volume effect.

Both models display a reduction in signal at the peak of the BOLD response with increasing contrast agent that is relatively consistent with the experimental data. Experimental data shows a uniform decrease in amplitude of the response with little change in the trailing edge, whereas the models show greater attenuation of the trailing edge. The reasons for this are unclear, but it may be due to the form of the flow model used in each case. Further experimental measurement of CBF are required to attempt to disentangle the total CBV measurements. The post-stimulus undershoot is also poorly modelled. At baseline, model 1 does not exhibit a post-stimulus undershoot. With increasing contrast agent concentration an undershoot appears, but earlier in the response than expected. This undershoot is due to the mismatch between the arterial and venous volume curves. Therefore it is likely that the form of the flow model curve is inconsistent with the experimental data. Model 2 exhibits an undershoot at baseline and with increasing contrast agent concentration. It occurs only slightly earlier than expected in the experimental data. The modelling of arterial flow would benefit from experimental measurements of the changes in CBF and arterial CBV in order to fine tune the form of the response.

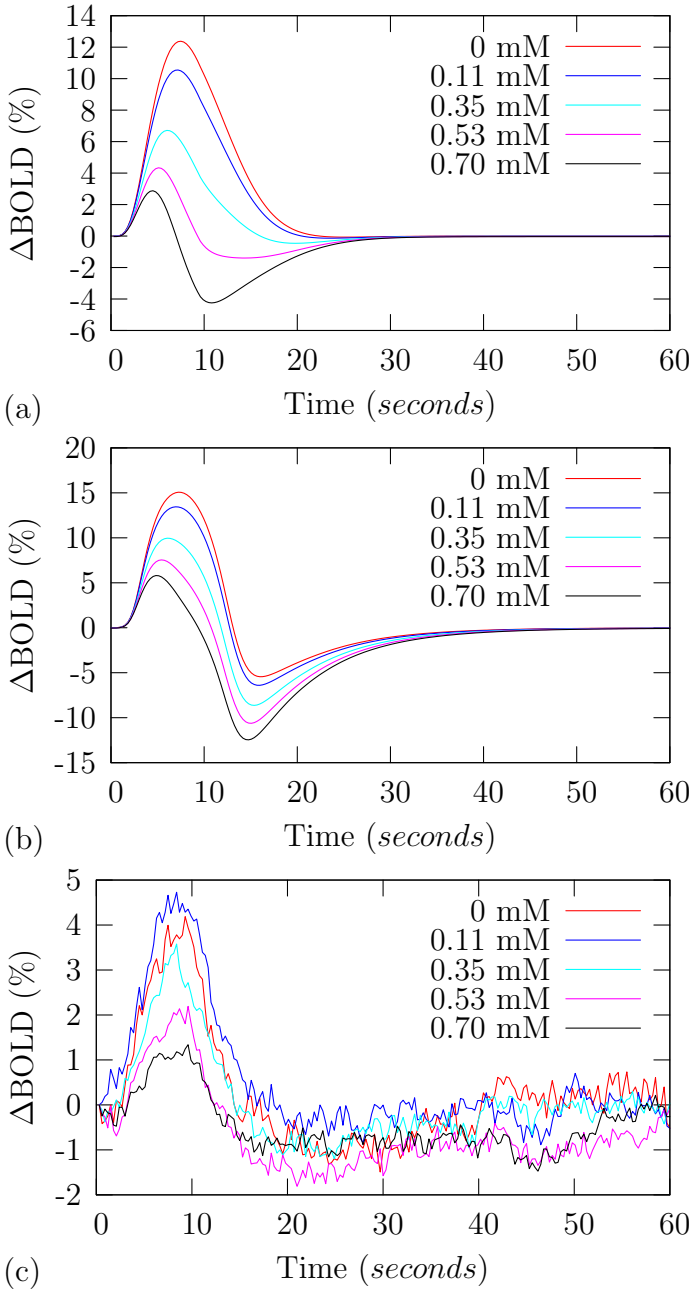

Figure 5.14: Baseline normalised data averaged in blocks of four stimulus cycles for model fits to (a) model 1, (b) model 2 and for (c) experimental data.

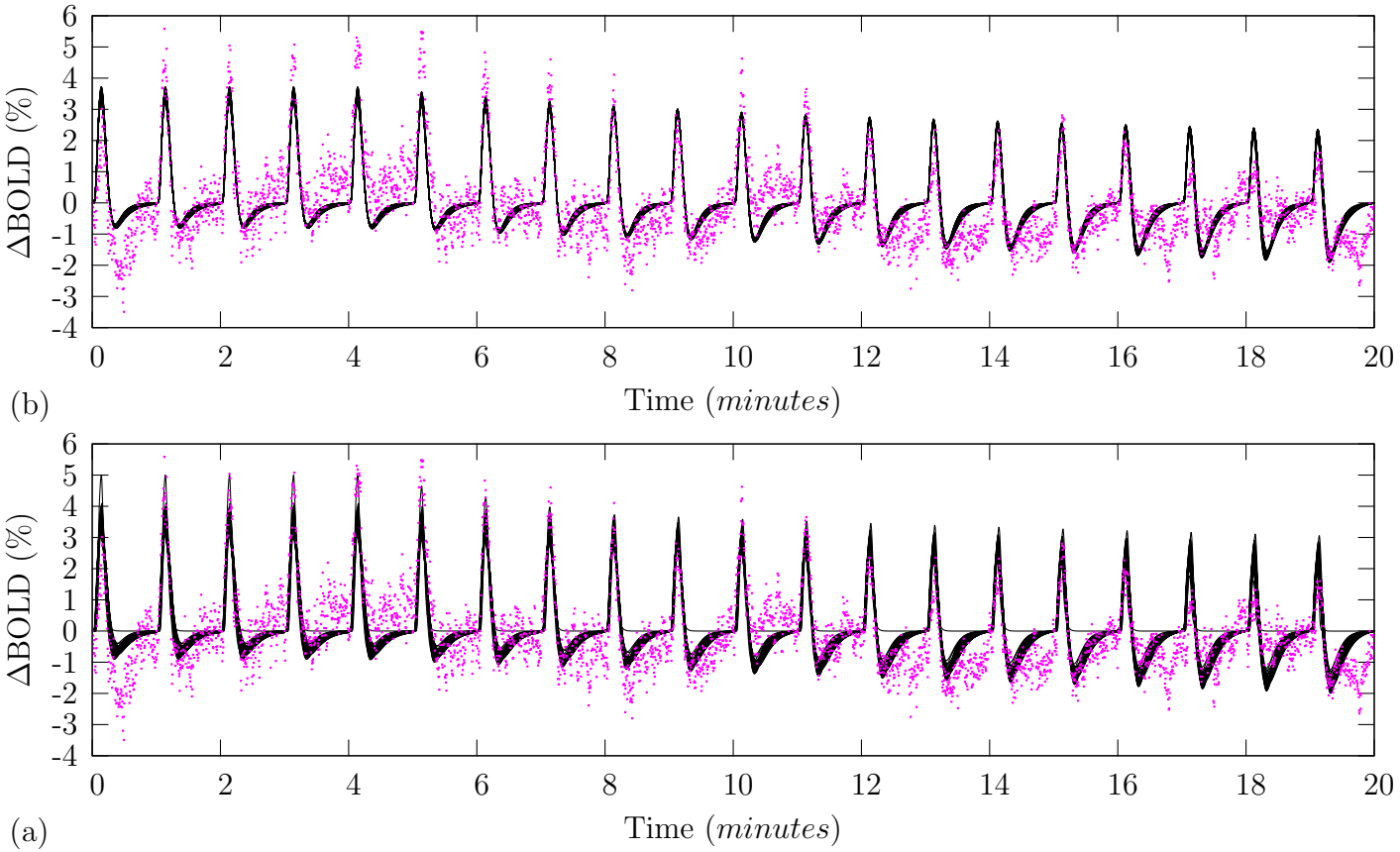

Figure 5.15: Model BOLD signal curves from fit to experimental signal data for (a) model 1 and (b) model 2. Experimental data points are plotted as dots.

5.4.2 Signal Fitting Results

Figure 5.15 shows the result of fitting models 1 and 2 to the experimental BOLD signal data of chapter 4. Mean sum of squared residuals for these fits to models 1 and 2 were 0.256 and 0.257, respectively. The standard deviation of the respective sum of squared residuals was 0.001 and 0.011. Both models follow the trend of a reduction in peak BOLD response with increasing contrast agent concentration. This is despite the confounding effects of inter-stimulus variability in the BOLD response and any instability in the MR signal. Model 2 shows particularly good correlation of the positive overshoot throughout. Each model displays a post-stimulus undershoot, which becomes more negative with increasing contrast agent concentration.

Figure 5.16 plots the model variables simulated using models 1 and 2 for the model fits to the experimental signal data. A slightly larger variability in curve solutions for model 1 can be seen when compared to the total CBV fitting. However the variability in model 2 is far greater than before. This is due to the highly unconstrained nature of the model. A large parameter space has to be defined, as it is difficult, or impossible, to measure suitable ranges for the parameters that describe the model. This allows the fitting algorithm to try many combinations of the variables f_{in}, v_v and q_v to achieve the same total BOLD signal. Fitting would benefit from experimental measures of these variables in order to reduce the number of plausible solutions.

Using the same technique as figure 5.14, the effect of an infusion of contrast agent can be compared. The form of both models differs markedly from their corresponding fits to the volume data. However contrary to the volume data both fits to the signal data are very similar in form. The timing of the initial edge of the post-stimulus undershoot described by both models shows good correlation with the data. The correlation of the form of the response is more difficult to discern, due to noise in the experimental data. Similarly the increasingly negative signal of the undershoot with increasing contrast agent concentration is difficult to compare with the data. This is due to errors in the baseline correction and the small magnitude of the effect.

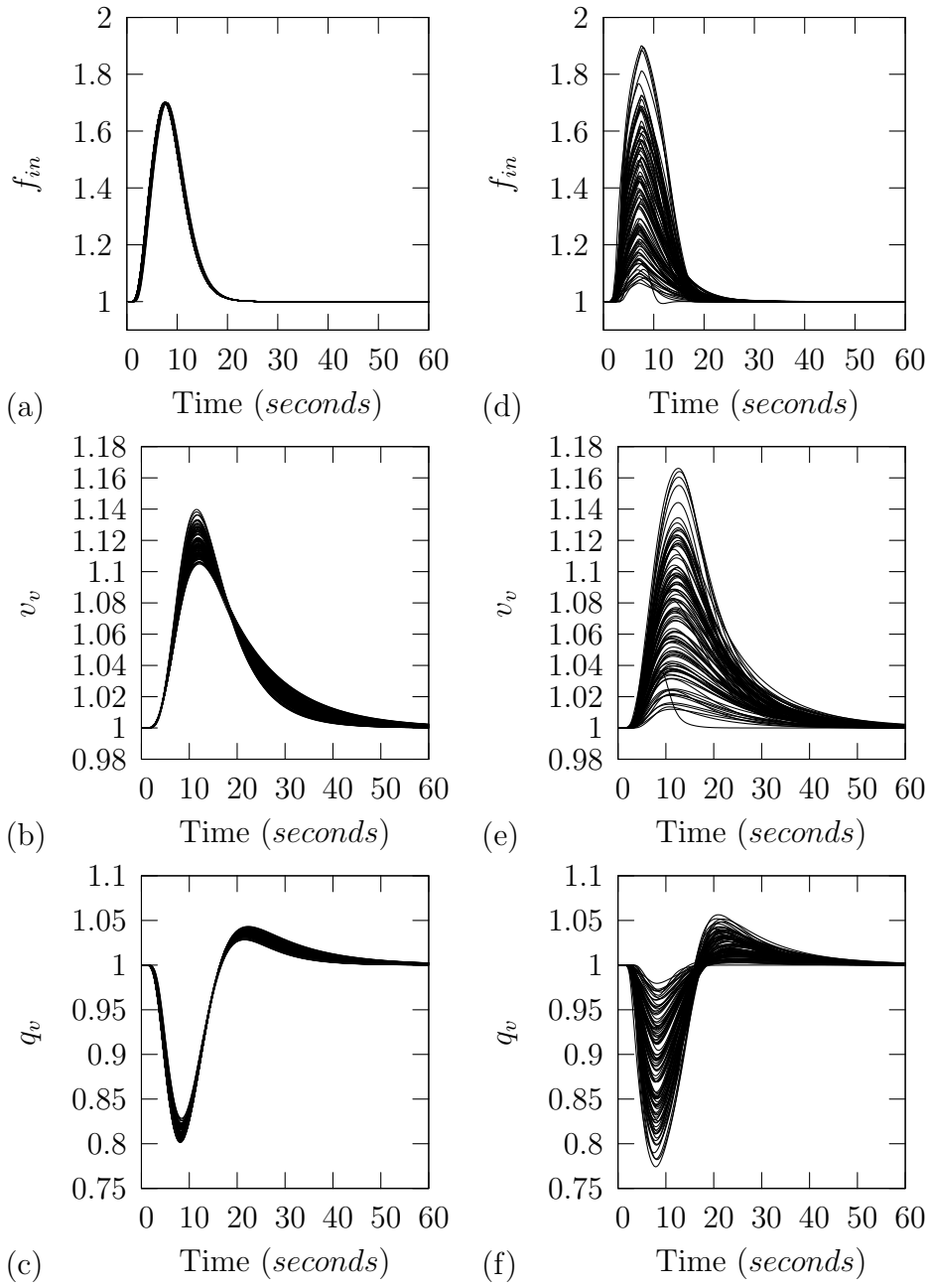

Figure 5.16: Model variables curves from fit to experimental signal data for (a-c) model 1 and (d-f) model 2. Simulated variables include arterial flow input to the system, f_{in}, venous outflow, v_v, and venous deoxyhaemoglobin content, q_v. Data consists of 100 curve solutions to the BOLD signal data.

In both model fits, the reduction of the positive overshoot with increasing contrast agent concentration does not correlate well with the experimental result. This is most likely due to an underestimation of CBV during this feature. One other interesting feature of the experimental data, compared with the simulations, is the increase in BOLD signal for the average of stimulus cycles 5-8. Magnetic field gradients within the blood, which surround paramagnetic red blood cells, are reduced in magnitude at low concentrations of contrast agent. As the contrast agent is also paramagnetic and is only present in the plasma, the susceptibility difference between red blood cells and plasma is reduced and the MR signal is increased. A more detailed description of the effect can be found in chapter 3.

As a final comparison the simulated total volume curves are plotted in figure 5.18, along with the measured data. The curve predicted by model 1 underestimates total CBV during the positive overshoot and overestimates it during the post-stimulus undershoot. This underestimated overshoot value helps to explain why this feature doesn't decrease rapidly enough with increasing contrast agent. However the overestimation of undershoot CBV suggests that the negative BOLD signal is similarly overestimated. Without this overestimation it is unlikely that a post-stimulus undershoot would be observed. Due to the large variation of solutions provided by model 2 there are several which would match the measured CBV data. It is likely that model 2 would suffer the same problems as model 1, by displaying an overestimation of post-stimulus blood volume. In order to fit model 2 accurately a measurement of CBF ($f_{in}(t)$) is needed. This could be simultaneously fitted alongside the signal data, thereby reducing the number of possible solutions.

5.5 Discussion

In this study an enhanced Balloon model has been applied to describe the experimental paradigm of chapter 4. This involved implementing all of the models described in section 5.2 in order to evaluate their suitability for this

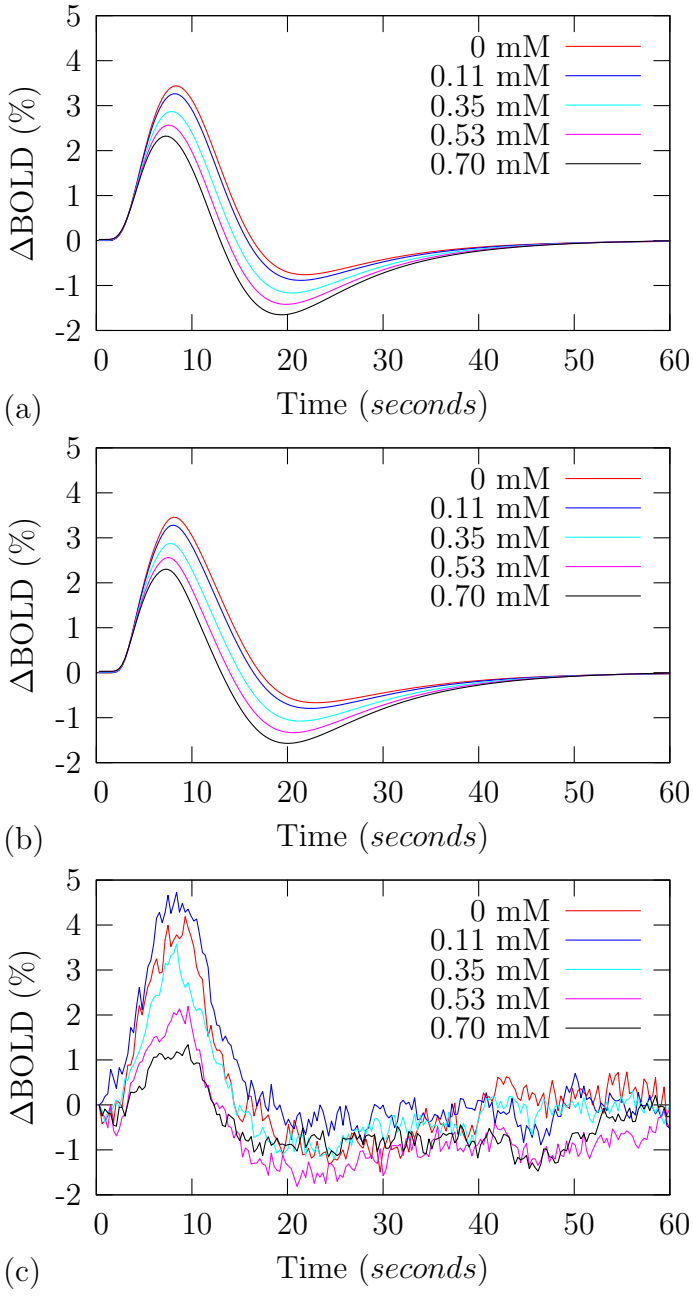

Figure 5.17: Baseline normalised data averaged in blocks of four stimulus cycles for model fits to (a) model 1, (b) model 2 and for (c) experimental data.

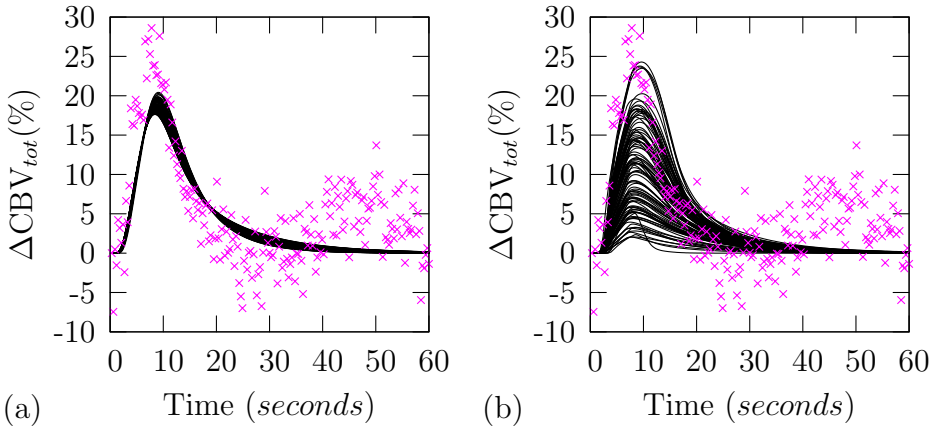

Figure 5.18: Model total CBV (ΔCBV_{tot}) curves from fit to experimental signal data for (a) model 1 and (b) model 2. Experimental data points are plotted as crosses along with all 100 curve solutions.

modelling effort. A multi-component BOLD signal model was analytically derived, based on the work of Obata *et al.* [106]. This was necessary since the infusion of contrast agent meant that the blood susceptibility was varied in both arterial and venous compartments. This situation was made more complex by the stimulus induced variations in susceptibility brought about by changing oxygenation states in the venous vasculature. Due to the high dimensional nature of the model fitting, it was a concern that multiple local minima may exist, particularly for model 2. Therefore the implementation of the simulated annealing fitting algorithm, and the subsequent discovery of local minima, was also important. This technique was also applied whilst fitting the models to both total CBV data and BOLD signal data.

The vascular model used in this work was originally described by Buxton *et al.* [47]. The Balloon model was chosen for its simplicity and versatility. The changing vascular state is modelled as the flow of an incompressible fluid through a network of tubes. An alternative model such as the one proposed by Mandeville *et al.* [68] follows a more abstract approach and describes this state in terms of an electrical circuit. Whilst this approach produces the

same result it can be less intuitive.

The versatility of the Balloon model is evident in its modular construction. The model is dependent on three main effects; arterial flow input, venous volume change and capillary oxygen extraction. Ancillary models of these quantities can be substituted into the Balloon model to produce a detailed description of the haemodynamic response. Section 5.2 details a selection of these Balloon model elements.

From the investigations in this chapter it is clear that flow input into the system is important in determining the form of the BOLD signal. Indeed the multi-component model described in section 5.3.3 suggests that arterial volume change contributes to BOLD signal even in the absence of susceptibility change. The form of the flow input also determines the venous volume change as the venous vasculature is assumed to be an essentially passive structure. Therefore venous volume change is determined by the elastic properties of the vessel walls.

The three models of flow described in section 5.2.1 represent an evolution in the modelling of this quantity. The Miller model determines the arterial input function empirically using an arterial spin labelling technique. This proved to be a very accurate method, but does not improve understanding of the underlying mechanism. In contrast the Friston model aimed to improve understanding by postulating a feed-forward mechanism relating neural activity to increases in flow. Whilst this benefits understanding, a greater number of parameters are required to describe this model. These hidden parameters are unmeasurable and so the range of valid values is unclear. Determining these ranges would require measurement of neural activity and flow across a range of stimuli.

Similarly the model of Behzadi extends the Friston model by modelling the coupling of neural activity to changes in arteriole radius, rather than flow. The model includes a realistic biomechanical model of arteriolar resistance describing the balance between passive and active components of the vessel wall. As a consequence an additional descriptive parameter is added. By

inclusion of a model of arteriole resistance, flow changes become increasingly smoothed. It has yet to be proven that this added level of complexity is required or realistic.

The volume models described in section 5.2.2 all have a common modelling ancestor. This model is conventionally known as Grubb's model. He noted that the relationship between CBF and CBV can be modelled by a power law. The major caveat of this work is that the measurements were carried out at steady state. Hence the other two models in this section attempt to describe this relationship when CBF is dynamically changing from one steady state to another. The dynamic volume model represents this as a transient lag of volume change and is controlled by a time constant. This time constant is allowed to take different values during inflation and deflation of the venous balloon. This allows the mechanical properties of the vessel walls to display viscoelastic effects. The modified windkessel model with compliance is also applicable during dynamics changes in blood volume. This model is an extension of the work of Grubb *et al.* [129] and Mandeville *et al.* [68]. As such the parameters required for its solution are more physiologically plausible and hence more easily measurable.

The models of oxygen extraction described in section 5.2.3 form the basis of the oxygenation level dependent effect. The oxygen limitation model [57] proposed that tight coupling between oxidative metabolism and blood flow could exist despite the evidence of Fox and Raichle [55] to the contrary. Whilst technically this model is only valid in the steady state it does describe oxygen extraction very well. However the assumption that all oxygen leaving the capillary is metabolised means that oxygen extraction and oxidative metabolism cannot be independently investigated. The OTT model solves both of these problems by extending the oxygen limitation model to the dynamic case and allowing a reservoir of oxygen in the tissue space. These changes allow future investigation into the the transient de-coupling of blood flow and metabolism, as an alternative explanation of the post-stimulus undershoot.

However, it appears that improvements in the theoretical understanding of the underlying effect come with a cost attached. This cost is in the precision of the solution. As was shown in section 5.3.2, given noisy experimental data and high numbers of parameters to estimate, the likelihood of an exact solution may diminish. A similar effect seems to have been observed in the work of Behzadi *et al.* [126]. In this work fitting was performed as a two step process. The first step consisted of a coarse grid covering the whole parameter space. The parameters which minimised the sum of squares cost function were then subjected to a constrained descent based algorithm. This method allows a reasonable fit to be achieved, which would be difficult if arbitrary initial estimates had been chosen. The added benefit of a simulated annealing technique is that the initial estimates are unimportant. No matter where the algorithm starts it will still try to sample the entire parameter space, bypassing local minima. However the cost of this method is compute time. Whilst much quicker than the brute force technique this algorithm is compute intensive. This problem is compounded by the need for repeat applications of the algorithm in order to sample the range of solutions.

As noted above it was necessary to derive a multi-component BOLD signal model due to changing susceptibility in both the arterial and venous vasculature. The model is a generalisation of the model of Obata *et al.* [106] and collapses back to their relation under their assumptions. This enables the arterial and venous volume changes, along with the venous oxygenation, calculated by the extended Balloon model to be incorporated into the simulated BOLD signal. Under zero contrast agent conditions the arterial component of the signal model produces a small correction due to the changing volume of the compartment. However when contrast agent concentration is non-zero this component acts to considerably reduce the BOLD signal and is weighted by changes in volume. The same effect is introduced into the venous signal using similar relations.

Using the multi-component model it was possible to fit the data from chapter 4. This model was fitted to either calculated total CBV data or

measured BOLD signal data. With respect to the total CBV data, models 1 and 2 provided a reasonable description of the total CBV curve. Model 2 was better at describing more subtle features, such as the change of slope between 15 s and 25 s. These parameter estimations were used to produce simulated BOLD signal timecourses. The correlation between the temporal dynamics of the major features of the response was good, despite the fit being performed on a single component of the BOLD signal model. Results suggest that the positive overshoot is well described by the model. However the post-stimulus period is less well described. The temporal dynamics of the post-stimulus undershoot produced by model 1 are particularly poor. This is not unexpected as the input to the model is purely empirical, and hence is extrapolated from other data [125]. The post-stimulus undershoot produced by model 2 correlates more closely with the experimental data. However the duration of this modelled response is shorter than seen experimentally. This is a consequence of the hypothesis for the origin of the post-stimulus undershoot. This theory suggests that the undershoot is due to the mismatch between CBF and CBV [69]. However this work was performed on α-chloralose anaesthetised rats and it has recently been shown [138] that this anaesthetic prolongs CBV dynamics. Therefore the experimental measure of total CBV, performed in chapter 4, does not support the hypothesis that the post-stimulus undershoot is due to a mismatch between CBF and CBV.

Both models showed good correlation when fitted to experimental BOLD signal data from the same experiment. The temporal characteristics of the post-stimulus undershoot compare well with the experimental data. However this effect is achieved by overestimating blood volume changes during this time period. Therefore the role of blood volume changes on the form of the post-stimulus undershoot is inconclusive, given these results. Volume change during the positive overshoot is underestimated leading to reduced signal loss as contrast agent concentration increases.

The results of this chapter suggest that a greater understanding of cerebral haemodynamics and metabolism are required to improve models of the

BOLD response. In addition greater emphasis needs to be place on testing new models using suitably designed experiments. In particular perturbations of the BOLD signal through introduction of contrast agents or physiological challenges can help to elucidate the underlying mechanisms. The Balloon model provides a good description of the positive overshoot, but improvements to the description of other features are required. It has been shown that fitting models with a high number of parameters leads to multiple independent minima. Evidently experiments with higher SNR would help to reduce this effect. It has been shown that these minima can be discovered by using a simulated annealing fitting algorithm. Fitting data using an empirical model (model 1) provides reasonably accurate results. However, despite the problems associated with fitting a high number of parameters, theoretical models (model 2) of the BOLD response are still preferable. These models push forward understanding of the technique that will help to discover the limits associated with BOLD fMRI. Ultimately experimental measurements of other model variables are required to reduce the number of valid solutions, such as CBF ($f_{in}(t)$), arterial CBV (v_a) and neuronal firing rates ($u(t)$). Future work should concentrate on this multi-mode approach.

Chapter 6

Conclusions

6.1 Summary

In this thesis, work was performed with the aim of elucidating the underlying mechanisms of the BOLD response. Investigations were centred around existing models of the BOLD response, in particular the Balloon model and its variants. A selection of model components were selected from the literature and tested against experimental data.

Total CBV changes were measured by an infusion of a paramagnetic contrast agent. The technique described in chapter 4 enabled fractional changes in blood volume to be measured with high temporal resolution (300 ms). This allowed the dynamics of blood volume change to be measured in response to a 4.8 s visual stimulus with high fidelity. Aside from the blood volume measurement, this experiment also provided an interesting way to probe the dynamics of the BOLD response. The introduction of contrast agent into the blood reduces MR signal. The signal reduction associated with temporal characteristics of the BOLD response were differentially affected by the contrast agent. Aspects of the response that were strongly dependent on volume change saw a greater reduction in signal intensity, relative to the resting state. This allowed a qualitative understanding of the volume contribution to each of these characteristics to be gathered.

Previously the dynamics of venous CBV change were thought [69] to be delayed with respect to CBF. In this work experiments were performed on α-chloralose anaesthetised rats. It has since been shown [138] that this anaesthetic prolongs CBV dynamics. The experiments of chapter 4 show that CBV does not exhibit a pronounced lag with respect to CBF. This would mean that the post-stimulus undershoot could not be due to a mismatch between CBF and venous CBV. An alternative explanation [70] for this characteristic is that metabolism could remain elevated beyond the cessation of the stimulus. The exact origin of this prolonged metabolic activity has yet to be determined.

An enhanced Balloon model was applied to describe this experiment using components derived from the literature. In order to describe the BOLD signal accurately, under the conditions of an infusion of contrast agent, a multi-component BOLD signal model was required. This requirement was caused by changing susceptibility in the arterial blood, as well as the venous blood, due to the contrast agent. A model was derived based on the work of Obata *et al.* and shown to be equivalent to this model under their assumptions. Intravascular blood signal was assumed to be dependent on the relaxivity of the blood and measurements were performed in chapter 3 to measure this.

Two models of the BOLD response were fitted to the experimental data of chapter 4. An investigation was performed to see whether a more sophisticated mechanistic model of the BOLD response would perform better than an empirical model. The differences between these two models was largely based on a differing number of descriptive parameters. Although evidently the more sophisticated model provided a much more detailed description of the underlying mechanism of the BOLD response. Due to the high number of fitting parameters involved there was a concern that multiple local minima would be present in the parameter space. This was shown to be the case for the sophisticated model, but not for the empirical model. A simulated annealing algorithm was employed for this work as the results it produced were

independent of the starting conditions. This method also had the advantage of only finding fits with high correlation to the data, which would have been harder to find using a descent based algorithm. This work shows that whilst more sophisticated models provide a better description of the mechanisms they are very difficult to fit accurately. Without experimental measurements of other quantities associated with BOLD signal, such as CBF, arterial CBV, and neural firing rates, it is not possible to narrow the range of solutions to those that are plausible.

In chapter 3 the relaxivity of whole blood as a function of oxygenation and contrast agent concentration was measured in order to model intravascular blood signal. The R_1 and R_2^* of whole blood were measured at 1.5 T, 3.0 T and 7.0 T. These measurements used high resolution imaging techniques and small samples of human blood. It was found that R_1 was dependent on oxygenation at field strengths above 1.5 T. The transverse relaxation rate R_2^* was shown to be linear over the physiological range of oxygenation values used and the R_2^* relaxivity increased with field strength. The R_1 dependence of contrast agent in blood was independent of field strength giving almost identical relaxivity values. This was as predicted by NMRD experiments [89, 94]. An interesting result was found when the R_2^* dependence of contrast agent in blood was measured. A non-linear relationship between R_2^* and contrast agent was encountered. Monte Carlo simulations showed that this relationship was quadratic in nature and highly sensitive to blood oxygenation. This result also provided an explanation for the anomalous increase in BOLD signal observed during the total CBV measurements in chapter 4. Stimulus cycles 5-8, which were measured in the presence of a low concentration of contrast agent in the blood, showed a higher BOLD signal than cycles 1-4, where contrast agent was not present.

6.2 Conclusions

The work presented in this thesis suggests that there is still much work to be performed before a full description of the BOLD response can be produced. Section 5.2 shows that there have been many good attempts at modelling the underlying causes of the response. However relatively little work has been performed on validating this work experimentally. Part of this problem lies in the design of suitable experiments to test models under a variety of physiological conditions. In this regard the experiment performed in chapter 4 provided a good way to perturb the MR signal and to see how BOLD models could cope with this disturbance. A secondary problem is the measurement of physiological parameters which directly, or indirectly, influence the BOLD response. Parameters such as CBF and arterial CBV can be measured directly using MRI techniques and would greatly aid the validation of flow models. Similarly neurovascular coupling could be investigated through the use of MEG. However many sophisticated models introduce many variables that are immeasurable in reality. For instance it is not possible to test the model of arteriolar compliance developed by Behzadi *et al.* [126] as it is impossible to measure the circumferential stresses hypothesised by the theory.

The results presented by chapters 4 and 5 contribute to the idea that the post-stimulus cannot be adequately modelled by a temporal lag between CBF and total CBV. The experiments show that the post-stimulus period is not very dependent on volume change. Similarly current BOLD models cannot adequately predict the post-stimulus undershoot, given that in reality the lag between CBF and CBV is so small. In order to advance understanding of the post-stimulus undershoot a model to describe post-stimulus metabolic activity is required. Such a model would require a working hypothesis of the origin of this metabolic activity, which at present has not been determined.

In conclusion, the fact that the positive BOLD response is used to infer changes in neural activity means that modelling the BOLD response is an important endeavour. The basic mechanism behind the positive overshoot is

well understood and forms a framework from which a more accurate model can be built. Other transient features, such as the post-stimulus undershoot, are less well modelled and require further research. A greater understanding of the BOLD response will give researchers greater confidence in this fMRI technique and possibly deliver better spatial specificity.

References

[1] C Boesch. Nobel prizes for nuclear magnetic resonance: 2003 and historical perspectives. *Journal of Magnetic Resonance Imaging*, 19:517–519, 2004.

[2] R R Ernst. Nuclear magnetic resonance fourier transform spectroscopy. *Nobel Lecture*, December 1992.

[3] P C Lauterbur. Image formation by induced local interactions: examples employing nuclear magnetic resonance. *Nature*, 242:190–191, 1973.

[4] P Mansfield and P K Grannel. NMR diffraction in solids? *Journal of Physics C: Solid State Physics*, 6:L422–466, 1973.

[5] D A Christie and E M Tansey, editors. *Making the human body transparent: the impact of nuclear magnetic resonance and magnetic resonance imaging*, volume 2, pages 1–74. The Welcome Trust, London, UK, 1998.

[6] P Mansfield. Snap-shot MRI. *Nobel Lecture*, December 2003.

[7] P A Bottomley, P Mansfield, and P S Allen. E. Raymond Andrew. June 27, 1921 – May 27, 2001. *Magnetic Resonance in Medicine*, 46(3):417–418, 2001.

[8] W Hinshaw. Spin mapping: the application of moving gradients to NMR. *Physics Letters*, 48A:87, 1974.

[9] J Hennig. The historical documentation of scientific developments: scientists should participate. *Journal of Magnetic Resonance Imaging*, 19:521–522, 2004.

[10] A N Garroway, P K Grannell, and P Mansfield. Image formation in NMR by a selective irradiative process. *Journal of Physics C: Solid State Physics*, 7(24):L457–L462, 1974.

[11] P Mansfield and A A Maudsley. Line scan proton spin imaging in biological structures by NMR. *Physics in Medicine and Biology*, 21(5):847–852, 1976.

[12] P Mansfield. Multi-planar image formation using NMR spin echoes. *Journal of Physics C: Solid State Physics*, 10:L55–L58, 1977.

[13] A Kumar, D Welti, and R R Ernst. NMR Fourier zeugmatography. *Journal of Magnetic Resonance*, 18:69–83, 1975.

[14] W A Edelstein, J M S Hutchinson, G Johnson, and T Redpath. Spin warp NMR imaging and applications to human whole-body imaging. *Physics in Medicine and Biology*, 25(4):751–756, 1980.

[15] P Mansfield and B Chapman. Active magnetic screening of gradient coils in NMR imaging. *Journal of Magnetic Resonance*, 66:573–576, 1986.

[16] P Mansfield and B Chapman. Active magnetic screening of coils for static and time-dependent magnetic field generation in NMR imaging. *Journal of Physics E: Scientific Instruments*, 19(7):540–545, 1986.

[17] R J Ordidge, R Coxon, A Howseman, B Chapman, R Turner, M Stehling, and P Mansfield. Snapshot head imaging at 0.5 T using the echo planar technique. *Magnetic Resonance in Medicine*, 8(1):110–115, 1988.

[18] P Mansfield, A M Howseman, and R J Ordidge. Volumar imaging using NMR spin echoes - echo volumar imaging (EVI) at 0.1 T. *Journal of Physics E: Scientific Instruments*, 22(5):324–330, 1989.

[19] S Goudsmit and G E Uhlenbeck. Spinning electrons and the structure of spectra. *Nature*, 117:264–265, 1926.

[20] P A M Dirac. The quantum theory of the electron. *Proceedings of the Royal Society of London. Series A*, 117:610–624, 1928.

[21] M Levitt. *Spin Dynamics: Basics of Nuclear Magnetic Resonance*. John Wiley & Sons Ltd., Chichester, UK, 2001.

[22] P Zeeman. The effect of magnetisation on the nature of light emitted by a substance. *Nature*, 55:347, 1897.

[23] H-U Kauczor, R Surkau, and T Roberts. MRI using hyperpolarized noble gases. *European Radiology*, 8:820–827, 1998.

[24] G Planinsic, D Grucker, and J Stepisnik. New method for contrast manipulation in DNP-enhanced MRI. *Magnetic Resonance in Medicine*, 35(3):379–383, 1996.

[25] F Bloch, W W Hansen, and M Packard. Nuclear induction. *Physical Review*, 69:127, 1946.

[26] E M Purcell, H C Torrey, and R V Pound. Resonance absorption by nuclear magnetic moments in a solid. *Physical Review*, 69:37–38, 1946.

[27] F Bloch. Nuclear induction. *Physical Review*, 70(7):460–474, 1946.

[28] H Y Carr and E M Purcell. Effects of diffusion on free precession in nuclear magnetic resonance. *Physical Review*, 94(3):630–638, 1954.

[29] E L Hahn. Spin echoes. *Physical Review*, 80(4):580–594, 1950.

[30] S Meiboom and D Gill. Modified spin-echo method for measuring nuclear relaxation times. *Review of Scientific Instruments*, 29(8):668–691, 1958.

[31] M A Bernstein, K F King, and X J Zhou. *Handbook of MRI pulse sequences*. Elsevier Academic Press, Burlington, MA, USA, 2004.

[32] F J Blatt. *Modern Physics*. McGraw Hill, New York, NY, USA, 1992.

[33] J V M McGinley, V C Srivastava, and G D DeMeester. Passive shimming technique for MRI magnets. *Magnetic Resonance Imaging*, 15(3):XIX, 1997.

[34] F Schmitt, M K Stehling, and R Turner. *Echo Planar Imaging*. Springer-Verlag, Wien, AT, 1998.

[35] R T Turner. Gradient coil design: a review of methods. *Magnetic Resonance Imaging*, 11:903–920, 1993.

[36] B Chapman and P Mansfield. Double active magnetic screening of coils in NMR. *Journal of Physics D: Applied Physics*, 19(7):L129–L131, 1986.

[37] K P Pruessmann, M Weiger, M B Scheidegger, and P Boesiger. SENSE: sensitivity encoding for fast MRI. *Magnetic Resonance in Medicine*, 42:952–962, 1999.

[38] S Ogawa, D W Tank, R Menon, J M Ellerman, S-G Kim, H Merkle, and K Ugurbil. Intrinsic signal changes accompanying sensory stimulation: Functional brain mapping with magnetic resonance imaging. *Proceedings of the National Academy of Sciences of the United States of America*, 89:5951–5955, July 1992.

[39] K K Kwong, J W Belliveau, D A Chesler, I E Goldberg, R M Weisskoff, B P Poncelet, D N Kennedy, B E Hoppel, M S Cohen, R Turner, H-M Cheng, T J Brady, and B R Rosen. Dynamic magnetic resonance

imaging of human brain activity during primary sensory stimulation. *Proceedings of the National Academy of Sciences of the United States of America*, 89:5675–5679, June 1992.

[40] D S Williams, J A Detre, J S Leigh, and A P Koretsky. Magnetic-resonance-imaging of perfusion using spin inversion of arterial water. *Proceedings of the National Academy of Sciences of the United States of America*, 89(1):212–216, 1992.

[41] B R Rosen, J W Belliveau, B R Buchbinder, R C McKinstry, L M Porkka, D N Kennedy, M S Neuder, C R Fisel, H J Aronen, and K K Kwong. Contrast agents and cerebral hemodynamics. *Magnetic Resonance in Medicine*, 19(2):285–292, 1991.

[42] H Lu, X Golay, J J Pekar, and P C M van Zijl. Functional magnetic resonance imaging based on changes in vascular space occupancy. *Magnetic Resonance in Medicine*, 50:263–274, 2003.

[43] S K Piechnik and P Jezzard. Sensitivity of the vascular space occupancy (VASO) method estimated using a multicompartmental blood-tissue model. In *Proceedings ISMRM 14th Meeting*, page 103, 2006.

[44] H Gray. *Anatomy of the human body.* Lea & Febiger, Philadelphia, PA, USA, 1918.

[45] H M Duvernoy. *The human brain: surface, three-dimensional sectional anatomy with MRI, and blood supply.* Springer-Verlag, Wien, AT, 2nd edition, 1999.

[46] G J Tortora and S R Grabowski. *Principles of anatomy and physiology.* John Wiley & Sons Ltd., New York, NY, USA, 9th edition, 2000.

[47] R B Buxton, E C Wong, and L R Frank. Dynamics of blood flow and oxygenation changes during brain activation : the balloon model. *Magnetic Resonance in Medicine*, 39:855–864, 1998.

[48] R M Weisskoff and S Kiihne. MRI susceptometry: image-based measurement of absolute susceptibility of MR contrast agents and human blood. *Magnetic Resonance in Medicine*, 24(2):375–383, 1992.

[49] S Ogawa and T M Lee. Magnetic resonance imaging of blood vessels at high fields: *in vivo* and *in vitro* measurements and image simulation. *Magnetic Resonance in Medicine*, 16(1):9–18, 1990.

[50] T Q Duong, E Yacoub, G Adriany, X Hu, and Uĝurbil. Microvascular BOLD contribution at 4 and 7 T in the human brain: gradient-echo and spin-echo fMRI with suppression of blood effects. *Magnetic Resonance in Medicine*, 49(6):1019–1027, 2003.

[51] P W Stroman, V Krause, U N Frankenstein, K L Malisza, and B Tomanek. Spin-echo versus gradient echo fMRI with short echo times. *Magnetic Resonance Imaging*, 19(6):827–831, 2001.

[52] L M Parkes, J V Schwarzbach, A A Bouts, R R Deckers, P Pullens, C M Kerskens, and D G Norris. Quantifying the spatial resolution of the gradient echo and spin echo BOLD response at 3 tesla. *Magnetic Resonance in Medicine*, 54(6):1465–1472, 2005.

[53] J Hulvershorn, L Bloy, E E Gualtieri, J S Leigh, and M A Elliott. Spatial sensitivity and temporal response of spin echo and gradient echo bold contrast at 3 T using peak hemodynamic activation time. *NeuroImage*, 24(1):216–223, 2005.

[54] S Ogawa, T M Lee, A S Nayak, and P Glynn. Oxygenation-sensitive contrast in magnetic resonance image of rodent brain at high magnetic field. *Magnetic Resonance in Medicine*, 14:68–78, 1990.

[55] P T Fox and M E Raichle. Focal physiological uncoupling of cerebral blood-flow and oxidative metabolism during somatosensory stimulation in human-subjects. *Proceedings of the National Academy of Sciences of the United States of America*, 83(4):1140–1144, February 1986.

[56] R B Buxton. The elusive initial dip. *NeuroImage*, 13:953–958, 2001.

[57] R B Buxton and L R Frank. A model for the coupling between cerebral blood flow and oxygen metabolism during neural stimulation. *Journal of Cerebral Blood Flow and Metabolism*, 17(1):64–72, 1997.

[58] N K Logothetis, J Pauls, M Augath, T Trinath, and A Oeltermann. Neurophysiological investigation of the basis of the fMRI signal. *Nature*, 412:150–157, 2001.

[59] R L Buckner, P A Bandettini, K M O'Craven, R L Savoy, S E Peterson, M E Raichle, and B R Rosen. Detection of cortical activation during averaged single trials of a cognitive task using functional magnetic resonance imaging. *Proceedings of the National Academy of Sciences of the United States of America*, 93:14878–14883, 1996.

[60] E Yacoub, A Shmuel, J Pfeuffer, P Van De Moortele, G Adriany, K Ugurbil, and Xiaoping Hu. Investigation of the initial dip in fMRI at 7 tesla. *NMR in Biomedicine*, 14:408–412, 2001.

[61] E Yacoub, T Huu Le, K Ugurbil, and X Hu. Further evaluation of the initial negative response in functional magnetic resonance imaging. *Magnetic Resonance in Medicine*, 41:436–441, 1999.

[62] J Röther, R Knab, F Hamzei, J Fiehler, J R Reichenbach, C Büchel, and C Weiller. Negative dip in BOLD fMRI is caused by blood flow - oxygen consumption uncoupling in humans. *NeuroImage*, 15:98–102, 2002.

[63] M Fukuda, P Wang, C-H Moon, M Tanifuji, and S-G Kim. Spatial specificity of the enhanced dip inherently induced by prolonged oxygen consumption in cat visual cortex: implication for columnar resolution functional MRI. *NeuroImage*, 30:70–87, 2006.

[64] Y Behzadi and T T Liu. Caffeine reduces the intial dip in the visual BOLD response at 3T. *NeuroImage*, 32:9–15, 2006.

[65] G H Glover, T-Q Li, and D Ress. Image-based method for retrospective correction of physiological motion effects in fMRI: RETROICOR. *Magnetic Resonance in Medicine*, 44:162–167, 2000.

[66] C M Peppiatt, C Howarth, P Mobbs, and D Attwell. Bidirectional control of CNS capillary diameter by pericytes. *Nature*, 443:700–704, 2006.

[67] R Turner. How much cortex can a vein drain? Downstream dilution of activation-related cerebral blood oxygenation changes. *NeuroImage*, 16:1062–1067, 2002.

[68] J B Mandeville, J J Marota, C Ayata, G Zaharchuk, M A Moskowitz, B R Rosen, and R M Weisskoff. Evidence of a cerebrovascular postarteriole windkessel with delayed compliance. *Journal of Cerebral Blood Flow and Metabolism*, 19:679–689, 1999.

[69] J B Mandeville, J J Marota, B E Kosofsky, J R Keltner, R Weissleder, B R Rosen, and R M Weisskoff. Dynamic functional imaging of relative cerebral blood volume during rat forepaw stimulation. *Magnetic Resonance in Medicine*, 39(4):615–624, 1998.

[70] H Lu, X Golay, J J Pekar, and P C M van Zijl. Sustained poststimulus elevation in cerebral oxygen utilization after vascular recovery. *Journal of Cerebral Blood Flow and Metabolism*, 24:764–770, 2004.

[71] M L Schroeter, T Kupka, T Mildner, K Uludağ, and D Y von Cramon. Investigating the post-stimulus undershoot of the BOLD signal – a simultaneous fMRI and fNIRS study. *NeuroImage*, 30:349–358, 2006.

[72] K J Friston, A Mechelli, R Turner, and C J Price. Nonlinear responses in fMRI: The balloon model, volterra kernels, and other hemodynamics. *NeuroImage*, 12:466–477, 2000.

[73] S Clare. *Functional magnetic resonance imaging: method and applications*. PhD thesis, University of Nottingham, 1997.

[74] Analyze. Mayo Clinic, Rochester, MN, USA.

[75] SPM2. Wellcome Department of Cognitive Neurology, London, UK.

[76] K J Friston, C D Frith, R J Dolan, J C Mazziotta, and R S J Frackowiak. *Human Brain Function*. Academic Press Ltd., London, UK, 1st edition, 1997.

[77] MATLAB. The Mathworks Inc., Nattick, MA, USA.

[78] P Jezzard, P M Matthews, and S M Smith. *Functional MRI: an introduction to methods*. Oxford University Press, Oxford, UK, 2001.

[79] R Freeman. *Spin choreography: basic steps in high resolution NMR*. Spektrum Academic Publishers, Oxford, UK, 1996.

[80] A Abragam. *Principles of Nuclear Magnetism*. Oxford University Press, Oxford, UK, 1961.

[81] S T Francis. *Magnetic resonance imaging of perfusion: techniques and applications*. PhD thesis, University of Nottingham, 1998.

[82] P T Callaghan. *Principles of nuclear magnetic resonance microscopy*. Oxford University Press, Oxford, UK, 1995.

[83] S Ogawa, T M Lee, A R Kay, and Tank D W. Brain magnetic resonance imaging with contrast dependent on blood oxygenation. *Proceedings of the National Academy of Sciences of the United States of America*, 87:9868–9872, December 1990.

[84] S Ogawa, R S Menon, D W Tank, S-G Kim, H Merkle, J M Ellerman, and K Ugurbil. Functional brain mapping by blood oxygenation level-dependent contrast magnetic resonance imaging: a comparison of signal characteristics with a biophysical model. *Biophysical Journal*, 64:803–812, 1993.

[85] D A Yablonskiy and E M Haacke. Theory of NMR signal behaviour in magnetically inhomogenous tissues: The static dephasing regime. *Magnetic Resonance in Medicine*, 32:749–763, 1994.

[86] D Li and D J Waight. In vivo correlation between blood T_2^* and oxygen saturation. *Journal of Magnetic Resonance Imaging*, 87:1236–1239, 1998.

[87] R B Lauffer. Paramagnetic metal complexes as water proton relaxation agents for NMR imaging: theory and design. *Chemical Reviews*, 87:901–927, 1987.

[88] P Caravan, J J Ellison, T J McMurry, and R B Lauffer. Gadolinium(III) chelates as MRI contrast agents: structure, dynamics, and applications. *Chemical Reviews*, 99:2293–2352, 1999.

[89] E Tóth, L Helm, and A E Merbach. Relaxivity of MRI contrast agents. *Topic in Current Chemistry*, 221:61–101, 2002.

[90] Z Luz and S Meiboom. Proton relaxation in dilute solutions of cobalt(II) and nickel(II) ions on methanol and the rate of methanol exchange of the solvation sphere. *The Journal of Chemical Physics*, 40(9):2686–2692, 1964.

[91] T J Swift and R E Connick. NMR-relaxation mechanisms of O^{17} in aqueous solutions of paramagnetic cations and the lifetime of water molecules in the first coordination sphere. *The Journal of Chemical Physics*, 37(2):307–320, 1962.

[92] H Pfeifer. Der translationsanteil der protonenrelaxation in wässrigen lösungen paramagnetischer ionen. *Annalen der Physik*, 463(1–2):1–8, 1961.

[93] J H Freed. Dynamic effects of pair correlation-functions on spin relaxation by translational diffusion in liquids. II. Finite jumps and inde-

pendent t_1 processes. *Journal of Chemical Physics*, 68(9):4034–4037, 1978.

[94] S H Koenig and R D Brown. Field-cycling relaxometry of protein solutions and tissue: Implications for MRI. *Progress in NMR Spectroscopy*, 22:487–567, 1990.

[95] J A Pears, S T Francis, S E Butterworth, R W Bowtell, and P A Gowland. Investigating the BOLD effect during infusion of Gd-DTPA using rapid T_2^* mapping. *Magnetic Resonance in Medicine*, 49:61–70, 2003.

[96] K R Thulborn, J C Waterton, P M Matthews, and G K Radda. Oxygenation dependence of the transverse relaxation time of water protons in whole blood at high field. *Biochimica et Biophysica Acta*, 714(2):265–270, 1982.

[97] R A Brooks, A Brunetti, J R Alger, and G Di Chiro. On the origin of paramagnetic inhomogeneity effects in blood. *Magnetic Resonance in Medicine*, 12(2):241–248, 1989.

[98] N A Matwiyoff, C Gasparovic, R Mazurchuk, and G Matwiyoff. On the origin of paramagnetic inhomogeneity effects in whole blood. *Magnetic Resonance in Medicine*, 20(1):144–150, 1991.

[99] A G Gardener. *In-vivo measurement of blood oxygenation using MR.* PhD thesis, University of Nottingham, 2005.

[100] ProHance. Bracco Diagnostics Inc., Princeton, NJ.

[101] ABL710 Blood Gas Analyser. Radiometer Medical ApS, Brønshøj, Denmark.

[102] H Dahnke and T Schaeffter. Limits of detection of SPIO at 3.0 T using T_2^* relaxometry. *Magnetic Resonance in Medicine*, 53:1202–1206, 2005.

[103] W M Spees, D A Yablonskiy, M C Oswood, and J J H Ackerman. Water proton MR properties of human blood at 1.5 tesla: magnetic susceptibility, t_1, t_2, t_2^*, and non-lorentzian signal behaviour. *Magnetic Resonance in Medicine*, 45:533–542, 2001.

[104] R M Weisskoff, S Z Chun, J L Boxerman, and B R Rosen. Microscopic susceptibility variation and transverse relaxation: Theory and experiment. *Magnetic Resonance in Medicine*, 31(6):601–610, 1994.

[105] P Gillis, S Petö, F Moiny, J Mispelter, and C-A Cuenod. Proton transverse nuclear magnetic relaxation in oxidised blood: a numerical approach. *Magnetic Resonance in Medicine*, 33:93–100, 1995.

[106] T Obata, T T Liu, K L Miller, L Wen-Ming, E C Wong, L R Frank, and R B Buxton. Discrepancies between BOLD and flow dynamics in primary and supplementary motor areas: application of the balloon model to the interpretation of BOLD transients. *NeuroImage*, 21:144–153, 2004.

[107] B Shuter, S C Wang, J Roche, G Briggs, and J M Pope. Relaxivity of Gd-EOB-DTPA in the normal and biliary obstructed guinea pig. *Journal of Magnetic Resonance Imaging*, 8(4):853–861, 1998.

[108] R V Mulkern, Y P Hung, Z Ababneh, S E Maier, A B Packard, M C Uluer, D F Kacher, G Gambarota, and S Voss. On the strong field dependence and nonlinear response to gadolinium contrast agent of proton transverse relaxation rates in dairy cream. *Magnetic Resonance Imaging*, 23:757–764, 2005.

[109] R P Kennan, B E Scanley, and J C Gore. Physiologic basis for BOLD MR signal changes due to hypoxia/hyperoxia: Separation of blood volume and magnetic susceptibility effects. *Magnetic Resonance in Medicine*, 37:953–956, 1997.

[110] K Scheffler, E Seitfritz, R Haselhorst, and D Bilecen. Titration of the BOLD Effect: Separation and quantitation of blood volume and oxygenation change in the human cerebral cortex during neuronal activation and ferumoxide infusion. *Magnetic Resonance in Medicine*, 42:829–836, 1999.

[111] S-P Lee, T Q Duong, G Yang, C Iadecola, and S-G Kim. Relative changes of cerebral arterial and venous blood volumes during increased cerebral blood flow: Implications for BOLD fMRI. *Magnetic Resonance in Medicine*, 45:791–800, 2001.

[112] V L Runge, K M Dickey, N M Williams, and X Peng. Local tissue toxicity in response to extravascular extravasation of magnetic resonance contrast media. *Investigative Radiology*, 37(7):393–398, 2002.

[113] F G Shellock and E Kanal. Safety of magnetic resonance imaging contrast agents. *Journal of Magnetic Resonance Imaging*, 10:477–484, 1999.

[114] S J McLachlan, S Eaton, and D N De Simone. Pharmacokinetic behaviour of gadoteridol. *Investigative Radiology*, 27:S12–S15, 1992.

[115] P G Welling. *Pharmacokinetics: processes, mathematics, and applications*. American Chemical Society, Washington, DC, USA, 2nd edition, 1997.

[116] J G Wagner. *Fundamentals of Clinical Pharmacokinetics*. Drug Intelligence Publications Inc., Hamilton, IL, USA, 1st edition, 1975.

[117] TEM and Occipital Coils. Nova Medical, Wilmington, MA.

[118] R B Buxton. Plumbing, energy or something else: What are we looking at with BOLD? In *Proceedings ISMRM 13th Meeting*, page 122, 2005.

[119] A Devor, A K Dunn, M L Andermann, I Ulbert, D A Boas, and A M Dale. Coupling of total hemoglobin concentration, oxygenation, and neural activity in rat somatosensory cortex. *Neuron*, 39:353–359, 2003.

[120] A Devor, I Ulbert, A K Dunn, S N Narayanan, S R Jones, M L Andermann, D A Boas, and A M Dale. Coupling of the cortical hemodynamic response to cortical and thalamic neuronal activity. *Proceedings of the National Academy of Sciences of the United States of America*, 102:3822–3827, 2005.

[121] J K Thompson, M R Peterson, and R D Freeman. Single-neuron activity and tissue oxygenation in the cerebral cortex. *Science*, 299:1070–1072, 2003.

[122] B M Ances, D G Buerk, J H Greenberg, and J A Detre. Temporal dynamics of the partial pressure of brain tissue oxygen during functional forepaw stimulation in rats. *Neuroscience Letters*, 306:106–110, 2001.

[123] V Toronov, S Walker, R Gupta, J H Choi, E Gratton, D Hueber, and A Webb. The role of changes in deoxyhemoglobin concentration and regional cerebral blood volume in the fMRI BOLD signal. *NeuroImage*, 19:1521–1531, 2003.

[124] M J Brookes, P G Morris, P A Gowland, and S T Francis. The non-invasive measurement of arterial cerebral blood volume using look-locher EPI and arterial spin labeling. *Magnetic Resonance in Medicine*, In Press, 2007.

[125] K L Miller, W-M Luh, T T Liu, A Martinez, T Obata, E C Wong, L R Frank, and R B Buxton. Nonlinear temporal dynamics of the cerebral blood flow response. *Human Brain Mapping*, 13:1–12, 2001.

[126] Y Behzadi and T T Liu. An arteriolar compliance model of the cerebral blood flow response to neural stimulus. *NeuroImage*, 25:1100–1111, 2005.

[127] C Lammertmann and B Lütkenhöner. Near-DC magnetic fields following a periodic presentation of long-duration tonebursts. *Clinical Neurophysiology*, 112:499–513, 2001.

[128] A Martinex-Hernandez, K P Bell, and Norenberg M D. Glutamine synthetase: glial localisation in brain. *Science*, 195:1356–1358, 1977.

[129] RL Grubb, ME Raichle, JO Eichling, and MM Terpogos. Effect of changes in Pa_{CO_2} on cerebral blood volume, blood flow, and vascular mean transit time. *Stroke*, 5(5):630–639, 1974.

[130] R B Buxton, K Uludağ, D J Dubowitz, and T T Liu. Modelling the hemodynamic response to brain activation. *NeuroImage*, 23:S220–S233, 2004.

[131] Y Kong, Y Zheng, D Johnston, J Martindale, M Jones, S Billings, and J Mayhew. A model of the dynamic relationship between blood flow and volume changes during brain activation. *Journal of Cerebral Blood Flow and Metabolism*, 24:1382–1392, 2004.

[132] Y Zheng, J Martindale, D Johnston, M Jones, J Berwick, and J Mayhew. A model of the hemodynamic response and oxygen delivery to the brain. *NeuroImage*, 16:617–637, 2002.

[133] R D Hoge, J Atkinson, B Gill, G R Crelier, S Marrett, and G B Pike. Linear coupling between cerebral blood flow and oxygen consumption in activated human cortex. *Proceedings of the National Academy of Sciences of the United States of America*, 96:9403–9408, 1999.

[134] R J Seitz and P E Roland. Vibratory stimulation increases and decreases the regional cerebral blood flow and oxidative metabolism: a positron emission tomography (PET) study. *Acta Neurologica Scandinavica*, 86:60–67, 1992.

[135] S Marret and A Gjedde. Changes of blood flow and oxygen consumption in visual cortex of living humans. *Advances in experimental medicine and biology*, 413:205–208, 1997.

[136] T L Davis, K K Kwong, R M Weisskoff, and B R Rosen. Calibrated functional MRI: mapping the dynamics of oxidative metabolism. *Proceedings of the National Academy of Sciences of the United States of America*, 95:1834–1839, 1998.

[137] A Kastrup, G Kruger, T Neumann-Haefelin, G H Glover, and M E Moseley. Changes of cerebral blood flow, oxygenation, and oxidative metabolism during graded motor activation. *NeuroImage*, 15:74–82, 2002.

[138] C Martin, M Jones, J Martindale, and J Mayhew. Haemodynamic and neural responses to hypercapnia in the awake rat. *European Journal of Neuroscience*, 24:2601–2610, 2006.